2014

# Impact of Tropical Cyclones on Ocean Heat Content and Transport

Michael R. Bueti
*University of Rhode Island*, mbueti@gmail.com

# IMPACT OF TROPICAL CYCLONES ON OCEAN HEAT CONTENT AND TRANSPORT

BY

MICHAEL R. BUETI

A DISSERTATION SUBMITTED IN PARTIAL FULFILLMENT OF THE REQUIREMENTS FOR THE DEGREE OF

DOCTOR OF PHILOSOPHY

IN

OCEANOGRAPHY

UNIVERSITY OF RHODE ISLAND

2014

DOCTOR OF PHILOSOPHY DISSERTATION

OF

MICHAEL R. BUETI

APPROVED:

Dissertation Committee:

Major Professor Isaac Ginis

Major Professor Lewis M. Rothstein

Stephen M. Griffies

Kathleen Donohue

Jason Dahl

Nasser H. Zawia

DEAN OF THE GRADUATE SCHOOL

UNIVERSITY OF RHODE ISLAND

2014

## ABSTRACT

Strong surface winds of a hurricane locally cool the surface and warm the subsurface waters via turbulent mixing processes. While the surface cool anomalies generally decay in roughly a month, the warm subsurface anomalies can persist over a seasonal cycle. We examine questions related to the magnitude and cumulative footprint of subsurface warm anomalies forced by tropical cyclones during the combined global tropical cyclone seasons, making use of a global ocean model forced by tropical cyclones.

Simulations of the 2004-2005 tropical cyclone season are conducted with and without tropical cyclone wind forcing, blended with the daily Coordinated Ocean-ice Reference Experiments (COREs) atmospheric state. Physical characteristics of cyclone-forced surface and subsurface anomalies are elucidated. In particular, we examine the spatial extent and magnitude of tropical cyclone forced subsurface warm anomalies over the course of an entire season. This analysis allows us to estimate the contribution of cyclone-induced anomalies to the ocean heat content and sea surface temperature, and to understand anomalous meridional heat transport.

Globally, there is a maximum accumulated heat uptake $4.1{\cdot}10^{21}J$, with the greatest regional contributions in the North Atlantic ($1.7{\cdot}10^{21}J$), West Pacific ($1.5{\cdot}10^{21}J$), and East Pacific ($1.7{\cdot}10^{21}J$). We find an export of heat from the subtropics to the tropics via rapid advective pathways, most notably in the West Pacific. These warm anomalies tend to remain in the equatorial band, with potential implications for the tropical climate system.

Analysis of a 20-year simulation using a semi-idealized tropical cyclone distribution reveals much of how the ocean adjusts to tropical cyclone induced warming on interannual timescales. The apparent quasi-equilibrium that the global ocean reaches over the first several years masks a great deal of regional variability. The redistribution of heat by intense cyclone winds results in semi-permanent warming of the

upper-thermocline in some regions by as much as $1/4°C$.

While there is a minimal impact on the upper ocean meridional heat transport, regional variability in anomalous heat content reaches a significant percentage of warming attributed to climate change. Lateral transport of warm anomalies plays a key role in maintaining the ocean heat balance, with those remaining in the mid-latitudes being released to the atmosphere during the local winter, and those exported poleward by upwelling in the tropics.

Crucially, transport pathways and ventilation mechanisms are regulated by the large-scale intraseasonal and interannual climate variability, specifically the North Atlantic Oscillation, Asian monsoon, and El Niño Southern Oscillation. These internal climate modes modulate the accumulation, release, and redistribution of tropical cyclone induced heating in a manner not addressed in globally focused analysis.

## ACKNOWLEDGMENTS

I would like to thank my major professors, Isaac Ginis and Lew Rothstein, for giving me the opportunity to study such an interesting and important problem at the Graduate School of Oceanography, and for providing the guidance and support needed to see the project through to completion. Thank you to Kathnleen Donohue and Jason Dahl for serving on my core committee. A special thank you goes to Stephen Griffies of NOAA's Geophysical Fluid Dynamics Laboratory, who took a keen interest in my research, and volunteered his much appreciated time and expertise.

I am grateful to GFDL and Oak Ridge National Laboratory for providing us with the needed computational resources and technical assistance. I would like to thank Whit Anderson and Zhi Liang at GFDL for their help throughout this project with the simulations and to Mike Winton for his support. I also thank Jae-Hun Park for helpful discussion, and Richard Yablonsky and Biju Thomas for development support.

I would like to thank WeatherPredict Consulting Inc. for providing financial support throughout my doctoral studies.

# DEDICATION

I would like to dedicate this dissertation to the friends and family who have supported and guided me throughout my education.

To my parents, Michael and Anne Bueti, who have always given me the support and opportunity to pursue my dreams and ambitions, even if it wasn't always clear just what I was going on about. I wouldn't be here without you.

To Nina, who's had to listen to more talk of hurricanes and heat transport than she even could have imagined, and kept me sane through deadlines, writer's block, and hard drive crashes. You've helped me feel at home while everything around me was changing.

To Caity and Jules, who never let my head get too big.

To the memory of Rocco and Maria Bueti, who always believed in me and who I hope would be proud of what I've accomplished.

To Leigh Ann Jervis DeLyser, who continued to teach and mentor me long after I left her classroom, and gave me tools I will be using for the rest of my career.

To all of my friends, loved ones, and colleagues from home and school. From New York, Pittsburgh, Narragansett, and Chicago. From Fox Lane, Carnegie Mellon, GFDL, and GSO. Thank you for helping me find what I love to do, and then making sure I didn't get too lost in it. For guiding me even when you didn't realize you were. For helping me have fun, even when I couldn't see past the next due date. For helping me get where I am without letting me forget who I am. Thank you, I love you all more than you know.

## PREFACE

This dissertation is written in manuscript format and consists of two scientific journal articles. The first chapter was published in the Journal of Climate Volume 27, Issue 18, in September of 2014. The second chapter is in preparation and will be submitted for publication in the near future.

## TABLE OF CONTENTS

Page

## LIST OF TABLES

## LIST OF FIGURES

# MANUSCRIPT 1

# Tropical Cyclone-Induced Thermocline Warming and its Regional and Global Impacts

Michael R. Bueti*, Isaac Ginis, Lewis M. Rothstein

*Graduate School of Oceanography, The University of Rhode Island, Narragansett, Rhode Island*

Stephen M. Griffies

*National Oceanographic and Atmospheric Administration/Geophysical Fluid Dynamics Laboratory, Princeton, New Jersey*

**Published in Journal of Climate, September 2014**

---

* *Corresponding author address:*

Michael R. Bueti,

Graduate School of Oceanography

The University of Rhode Island,

215 South Ferry Road,

Narragansett, RI 02882

Email: mbueti@my.uri.edu

## 1.1 Introduction

Tropical cyclones (TCs) are highly coherent, intermittent, and intense wind and precipitation events, notable for their ability to induce strong vertical oceanic mixing over the course of their lifetime. TCs are defined by their cyclonic winds, which increase from nearly zero to magnitudes exceeding 70 $m\ s^{-1}$ at a radius of maximum wind on the order of 50 km before decreasing over several hundred kilometers. Strong sea surface temperature (SST) cooling associated with TC passage over the ocean produces a well-understood cold wake due to vertical mixing of mixed layer and upper thermocline waters (Price, 1981), and anomalous surface buoyancy fluxes and upwelling induced by the strong wind stress curl.

SST returns to its climatological value within 30-40 days regardless of storm intensity (Dare and McBride, 2011), with local restoration due to anomalous heat flux associated with SST cooling (Price et al., 2008). Furthermore, restoration of the shallow cooling takes place over similar timescales, although full climatological mixed layer (CML) restoration takes several months (Park et al., 2011; Price et al., 2008). However, the subsurface warm anomalies decay over much longer timescales (Pasquero and Emanuel, 2008) since they are not subject to the same restoration processes as the mixed layer cold anomaly. Emanuel (2001) estimated that the restoration of an idealized cold wake could result in the introduction of up to $5{\cdot}10^{21}\ J$ of anomalous ocean heat uptake (OHU). Extending this analysis to an idealized modeling study he hypothesized that a full year of TC activity could produce an annual mean OHU rate of $1.4 \pm 0.7\ PW$.

Studies since Emanuel (2001) have attempted to refine the magnitude of TC induced ocean heating based on global observations from remote sensing instruments. Sriver and Huber (2007) used satellite SST and model reanalysis of ocean data to derive a mean annual TC induced OHU rate of 0.26 $PW$, later revised to a peak value

of 0.6 $PW$ and accompanying 60% increase in ocean heat transport (OHT) based on refined estimates of mixed layer (ML) deepening (Sriver et al., 2008). Jansen et al. (2010) utilized SST and SSH satellite observations, and ML depth and stratification from ocean reanalysis to estimate a mean annual seasonal thermocline heat deposition rate of 0.58 $PW$, which may produce a comparable OHU.

Jansen et al. (2010) hypothesized that the magnitude of persistent TC heat pumping in previous studies is systematically overestimated on interannual timescales, with upper-thermocline warm anomalies entrained into the winter ML and reventilated to the atmosphere. Accounting for this heat release results in a mean annual OHU rate of 0.15 $PW$, a 75% reduction of their previous estimate. Shoaling of upper thermocline warm anomalies by baroclinic ML instabilities enhances this reventilation, a process unaccounted for in most observational estimates (Jansen et al., 2010; Boccaletti et al., 2007). Pasquero and Emanuel (2008) found that equatorial upwelling also releases TC OHU to the atmosphere. Using gridded SSH measured from satellite, Mei et al. (2013) derived a global annual OHU of $1.01 \pm 0.46 \cdot 10^{22} J$ and mean annual rate of $0.32 \pm 0.15$ $PW$ from the thermal expansion needed to account for TC induced SSH anomalies.

Argo float data has recently been used to directly quantify TC OHU. Park et al. (2011) used pre- and post-storm float pairs to estimate TC induced OHU, finding that storms of Category 3 or less ($\sim$85% of annual TCs) produce no detectable subsurface warming, with the remaining storms producing an OHU rate $\sim 0.19 \pm 0.03$ $PW$. The spatial and temporal sparseness of in situ observations in relation to storm tracks, effects of Ekman pumping, inertial gravity waves, and other background variability make the accurate quantification of TC-induced OHU from these observations quite difficult.

Numerical modeling studies with varying levels of dynamical and thermodynam-

ical idealization have also been used to study the magnitude and mechanisms of TC OHU. Pasquero and Emanuel (2008) used a 4° horizontal resolution ocean general circulation model (OGCM) with specified mixing to 75 $m$, equivalent to a 25 $m$ deepening of the ML, resulting in $1.1{\cdot}10^{22}$ $J$ of OHU over 12 months of model integration, from which we estimate a mean annual rate of 0.35 $PW$. Approximately 50% of this heating persisted through the winter, while anomalies from mixing down to 155 $m$ had ∼80% retention. Sriver and Huber (2010) specified realistic TC wind forcing derived from QuikScat data in a 3.6° zonal by 1.5° meridional resolution OGCM. By doubling and tripling the TC winds, mean OHU rates varied from 0.1 $PW$ to 0.3 and 0.8 $PW$ respectively, during 500 years of model integration. Anomalous heat transport was predominantly into the tropics, warming the upper 300 $m$ of the tropical Pacific, with much of the heat deposited in the Equatorial Undercurrent (EUC).

Enhanced diffusivity of $\kappa{\sim}1$ $cm^2$ $s^{-1}$ has been used as a proxy for TC wind forcing. Manucharyan et al. (2011) used this method in the upper 200 $m$ of the ocean between 8° and 40° latitude in a 1.25° zonal and 0.25°−1° meridional resolution OGCM. Enhanced mixing was applied uniformly in time, seasonally, and as discrete multi-day events repeated over 200 years of model integration, with the resulting OHU producing an average ∼0.2 $PW$ of poleward and equatorward OHT over the last 25 years of simulation. Forcing was found to be most effective when applied during the local summer, demonstrating sensitivity to temporal variability in TC activity. Jansen and Ferrari (2009) demonstrated a sensitivity to the meridional distribution of TC forcing in a 2.8° resolution OGCM by introducing an enhanced diffusivity uniformly between 31°$N/S$, with gaps imposed between 11.2°$N/S$ and 5.6°$N/S$. Increases in poleward OHT reached values of 0.24 $PW$ with no equatorial gap, which decreased to ∼0.175 and ∼0.15 $PW$ with increasing gap size during their 100 year analysis timeframe. These gaps also allow for enhanced OHT into the tropics of ∼0.15 and

$\sim$0.25 $PW$, respectively.

Scoccimarro et al. (2011) used a coupled ocean-atmosphere general circulation model with a 2° resolution ocean, finding a 35% increase in equatorward OHT between 0° and 18°$N$ ($\sim$0.5 $PW$), a 5% increase in poleward OHT between 18°$N$ and 40°$N$ ($\sim$0.1 $PW$) attributed to the presence of TCs during their 120 year experiment. While their 3/4° resolution atmosphere reproduced the climatology of TC distribution and movement, it underestimated the annual frequency by $\sim$15%, with a bias towards weaker storms. Jullien et al. (2012) conducted finer (1/3°) resolution regional study in the South Pacific, with surface forcing from global Weather Research and Forecasting (WRF) model output with and without TCs. They derived a regional OHU rate of $\sim$0.015 $PW$ during the southern TC season, with an attenuation of $\sim$0.009 $PW$ over the winter. This region is subject to 10$-$15% of global TC activity, and of those the WRF forcing contains fewer major TCs than observed.

Recently, Vincent et al. (2013) used a 1/2° OGCM initialized from World Ocean Atlas climatology and forced with winds from version 2.0 of the Coordinated Ocean-Ice Reference Experiments (CORE-II) and synthetic vortices based on the IBTrACS record and Willoughby et al. (2006) wind profile formulation to explore the impact of TCs on the mean ocean state. They found broad cooling in the mixed layer, with underlying warming and cooling in the upper thermocline due to mixing and upwelling/downwelling, and offsetting warming and cooling deeper in the water column due only to upwelling/downwelling. They attempted to account for cooling from enhanced fluxes during TC passage offsetting the impact of mixing induced OHU, as well as fall/winter release of heat anomalies to the atmosphere via surface heat fluxes. They quantified the average 3D response in various regions, finding subsurface warming in the subtropical North West Pacific down to nearly 200 $m$ underlying cooling to $\sim$40 $m$. They found that $\sim$1/4 of TC heating is transported out of its

region of generation, with ∼40% released locally during winter ML deepening and ∼1/3 compensated by loss of heat to the atmosphere during TC passage. Meridional OHT was derived from a surface flux based overturning, with all anomalous heat moving on average from latitudes of net input to those of heat release, displaying a transport from the subtropics poleward to the mid-latitudes, and equatorward to the deep tropics. This assumed a quasi-steady state response interannually, and stressed the importance of dynamical effects such as Ekman pumping and nonlinear wave propagation over mixing in many cases for heat transport.

We expand on previous studies of this topic using a global ocean-ice general circulation model of finer resolution than those used in previous studies, with realistic TC surface boundary conditions. In this way, we hope to better understand the rate and magnitude of TC induced OHU over intraseasonal and interseasonal timescales, both globally and in the individual ocean basins. Specifically, we will enumerate and contextualize this heat uptake for a single year, explore its regional climate significance, and detail likely pathways and timescales that dictate the export of heat from the dominant TC forcing regions.

## 1.2 Methods

### 1.2.1 The ocean model

We use GFDL's Modular Ocean Model (MOM), version 4 (Griffies, 2009). MOM is a hydrostatic primitive equation ocean model configured using a Boussinesq approximation with a free surface algorithm and coupled to the SIS (Sea Ice Simulator) ice model to handle processes in the high latitudes. We utilize an ocean-ice configuration with its resolution taken from the CM2.5 coupled climate model documented in Delworth et al. (2012). The horizontal resolution varies from 28 $km$ at the equator to $8-11$ $km$ at high latitudes. The model has 50 vertical levels, 23 of which are in the upper 500 $m$ of the ocean.

The upper ocean mixing and restratification is of particular importance in evaluating the ocean's response to TCs. Vertical mixing of tracers and momentum is handled by the KPP boundary layer scheme (Large et al., 1994), which computes enhanced mixing within a boundary layer depth determined according to a bulk Richardson number. Mixing of tracers also arises in regions of negative surface buoyancy fluxes from a non-local transport term proportional to surface boundary heat and salt fluxes. Beneath the boundary layer, tracer mixing arises due to parameterized shear instability, tide-induced mixing, double diffusion, and convection due to gravitational instabilities. The parameterized mixing is thus highly variable in both space and time, producing mixing that is strongly dependent on the applied surface forcing. MOM parameterizes the effect of sub-mesoscale mixed layer eddies according to Fox-Kemper et al. (2011), with these eddies enhancing the ventilation of TC warm anomalies (Jansen et al., 2010).

### 1.2.2 Air-sea fluxes and TC forcing

The ocean model is forced with air-sea boundary conditions as in the CORE-II experiments described by Griffies et al. (2009). The prescribed atmospheric state is from the Corrected Inter-Annual Forcing product (Large and Yeager, 2009) with a 1.9° resolution, providing sea level pressure, air temperature, specific humidity, zonal and meridional winds at 10 $m$, every six hours; daily average values for incoming shortwave and longwave radiation; and monthly averages of liquid and frozen precipitation rates. The CORE-II winds are relatively coarse, so that TC winds are poorly resolved, if present at all. As an example, the strong winds in the compact TC eye-wall region of Category 4 Hurricane Frances (here on 1 September 2004 north of Hispaniola), critical for producing ocean mixing, are entirely absent (Fig. 1.1a).

In this study we introduce two changes to the CORE-II boundary conditions. First, the parameterization of the drag coefficient, $C_D$, is modified for strong winds.

The linear relationship between wind speed and $C_D$ (Large and Yeager, 2004) and used in CORE-II greatly overestimates the wind stress for high wind speeds, particularly those present in tropical cyclones (Powell et al., 2003); Moon et al. (2007). The high $C_D$ values result in unrealistically intense vertical mixing (Sanford et al., 2007). For wind speeds greater than 12.5 $m\ s^{-1}$, we replace the Large and Yeager (2004) parameterization with the formulation of Moon et al. (2007), empirically derived from coupled wave-wind model simulations in hurricanes. The hybrid drag coefficient increases more slowly than in Large and Yeager (2004) and levels off for wind speeds greater than 40 $m\ s^{-1}$.

Second, we modify the CORE-II winds by introducing synthetic TCs based on the National Hurricane Center (NHC) and Joint Typhoon Warning Center (JTWC) Tropical Cyclone Vitals Database (TCVitals). This database contains cyclone location, intensity, and structure information, generated in real time by forecasters (Table 1.1,1.2). TCVitals are used to initialize cyclones in operational forecasting models. We use TCVitals because they contain parameters such as radius of maximum wind, radius of last closed isobar, and the radii at which winds reach values of 18 $m\ s^{-1}$ and 26 $m\ s^{-1}$ in the northeast, southeast, southwest, and northwest quadrants of the storm (extended structure data), which are not consistently available for all basins from IBTrACS (International Best Track Archive for Climate Stewardship) or NHC's North Atlantic hurricane database (HURDAT2). While there are statistical biases in storm intensity ($\sim$0.25$-$1 $m\ s^{-1}$) and location (0$-$5 $km$) compared to the best track database (Trahan and Sparling, 2012), these errors should have negligible impact on the results of this study.

Air-sea heat fluxes are calculated from bulk formulae as described in Griffies et al. (2009). No explicit SST restoration is applied. Surface heat fluxes are allowed to freely evolve under the specified atmospheric state and respond to both the enhanced TC

winds and cooled SSTs in the storm cold wakes. The air temperature and humidity are unperturbed from their CORE-II values and do not respond to the ocean state, with implications for the character of these fluxes. Specifically, the elevation of latent and sensible heat fluxes out of the ocean in response to high TC wind speeds is underestimated in our simulations. Likewise, suppression of the latent heat flux out of the ocean and rate of the resulting upper ocean warming in the TCs cold wake may be somewhat overestimated.

Synthetic TC wind speeds are generated for each storm in the TCVitals as is done for operational hurricane forecasting (Bender et al., 2007). The cyclone wind field is projected onto the ocean model grid, and at any location where the CORE-II wind speed is lower than the TC wind speed it is replaced by the latter (Fig 1.1b). For cases when the extended structure data is unavailable, the axisymmetric wind profile of Holland (1980) is used. The Holland (1980) axisymmetric profile comprises only $\sim$20% of storm hours, typically during cyclogenesis and storm dissipation. Further details of the wind formulation and the blending method are described in the Appendix.

The 2004-2005 global TC season is simulated from the start of the North Atlantic hurricane season (1 June) and integrated for one full calendar year. There were 92 TC events during these 12 months (Fig.1.2), with the greatest number in the West Pacific (WestPac) (30), a significant number in the North Atlantic (16), East Pacific (EastPac) (17), and Southern Hemisphere (18), and a few in the North Indian Ocean (3). The boundaries and oceanic surface areas of these basins are defined in Table 1.3.

### 1.2.3 Experimental procedure

The model is run from 1 June 2004 through 31 May 2005 in two forcing configurations. The first has surface forcing based on the CORE-II atmospheric state, and

we will refer to this experiment as the "control experiment" (Fig. 1.1a). The other configuration has the CORE-II surface wind augmented by embedding the synthetic TCs, and will be referred to as the "TC experiment" (Fig. 1.1b). An "anomaly" is defined as the difference between the oceans in the TC and control experiments, thus yielding the net thermal and dynamical effect of TC activity.

Ocean initial conditions are derived from GFDL's Ocean Data Assimilation Experiment (ODAE) product, described by Zhang et al. (2007). This product provides the average monthly temperature and salinity fields at 1° grid spacing. MOM is started on December 1, 2003 from the ODAE December 2003 field interpolated onto the ocean model grid, with air-sea fluxes computed based on the CORE-II atmospheric state. The model is run for six months. At this point, the ocean has reached a mechanical quasi-steady state with the ocean's globally integrated total kinetic energy being $\sim$3500 $PJ$.

### 1.2.4 Seasonal behavior

To evaluate the seasonal behavior of the ocean model and set a baseline against which to compare TC heating values, the seasonal component of the upper Ocean Heat Content (OHC) is calculated. OHC is defined as

$$OHC\,(t) = c_p \rho_o \int_{-729\ m}^{0m} dz \int_{x_w}^{x_e} dx \int_{y_s}^{y_n} dy \Delta T_{729m} \tag{1.1a}$$

$$\Delta T_{729m} = T\,(x, y, z, t) - T\,(x, y, z = -729\ m, t) \tag{1.1b}$$

where $[x_w, x_e; y_s, y_n]$ are the [zonal; meridional] domain boundaries. The 729 $m$ depth level is selected as it is the closest model level to the 700 $m$ depth used by in situ analyses, such as Levitus et al. (2012b).The seasonal OHC variability is defined as

$$\Delta OHC_{season}(t) = OHC(t) - \overline{OHC(t)} \tag{1.2}$$

where the overbar denotes time averaging from 1 June-31 May. A 30-day low pass filter is applied in order to isolate the seasonal behavior from higher frequency vari-

ability.

The seasonal OHC amplitude in MOM is compared to that found by applying Eq. 1.2 to an independent data source, the Navy Coupled Ocean Data Assimilation (NCODA) product (Cummings, 2005). As NCODA data at a consistent horizontal resolution is not available until the 2007 calendar year, $\Delta OHC_{season}$ in MOM is calculated from both 1 June 2004-31 May 2005 and 1 June 2007-31 May 2008, presented in Fig. 1.3. $\Delta OHC_{season}$ is consistent between model run years, with little difference in phase and amplitude. The seasonal OHC in MOM is on average $\sim$8% smaller than in NCODA (though at times this discrepancy is closer to $\sim$18%), but otherwise in good agreement. This comparison gives confidence that MOM is capturing the seasonal behavior of OHC reasonably well. The maximum global excursion of $\Delta OHC_{season}$ (calculated as the sum of the Northern and Southern hemisphere extrema), as well as those for the individual ocean basins, is presented in Table 1.4. A cross-comparison of ML depths between MOM and NCODA was conducted as well. While not shown, the temporal and spatial structure of the modeled ML were generally consistent with those derived from NCODA data.

## 1.3 Results

### 1.3.1 Test cases

Two TC cases are considered to test the model response and explore the physical processes involved in simulating the ocean response to TC passage. In this way the suitability of our analysis is established. We select 2004's Hurricane Frances (Table 1.1), a category 4 hurricane that took place from 25 August-7 September 2004 in the North Atlantic, and Typhoon Songda (Table 2), a category 4 typhoon that took place from 27 August-7 September 2004 in the West Pacific. The Hurricane Frances case is selected due to the availability of observational data from the Coupled Boundary Layers and Air-Sea Transfer (CBLAST) field experiment (Black et al., 2007), D'Asaro

et al. (2007). Typhoon Songda is selected for comparison of the ocean response to a TC with similar intensity, duration, and track length in the West Pacific.

To investigate the restoration timescale of TC induced anomalies, model integration is carried out through 31 December 2004 ($\sim$2 weeks of storm passage and just over 4 months of ocean recovery). SST and $\Delta SST$ following passage of Hurricane Frances and Typhoon Songda are shown in Fig. 1.4, with both TCs producing strong cold wakes by 5 September. Fig. 1.5 focuses on the cold wake of Hurricane Frances on 1 September, with domain boundaries selected to approximate those in Fig. 1 from D'Asaro et al. (2007). Note that on 1 September the modeled background SST, and thus the cold wake SST, displays a $\sim 0.5^{\circ}C$ low bias in this region as compared to the observations, and so a corresponding shift has been made in the color range of Fig. 1.5 relative to Fig. 1 in D'Asaro et al. (2007). The model exhibits a cooling of $2.5^{\circ}C$ (Fig. 1.5b) comparable to the $2.2^{\circ}C$ maximum SST anomaly found in the same region by D'Asaro et al. (2007). Hurricane heat content integrated to the $26^{\circ}C$ isotherm, defined in D'Asaro et al. (2007), is reduced by $\sim 100\ m^{\circ}C$ (Fig. 1.5d), comparable to the $\sim 125\ m^{\circ}C$ from D'Asaro et al. (2007). The cold wake of Frances is consistent in spatial structure with CBLAST observations.

Typhoon Songda produces a stronger simulated cold wake (Fig. 1.4 c,d) with maximum cooling $\sim 5.5^{\circ}C$. Songda passes over a more strongly stratified ocean (Fig. 1.9b), allowing for a more intense modeled cold wake (Vincent et al., 2012b), with its slower translation speed during the period of maximum cooling ($\sim 5\ m\ s^{-1}$) compared to that of Frances ($\sim 6\ m\ s^{-1}$) reinforcing the effect (Yablonsky and Ginis, 2009; Mei and Pasquero, 2013). The modeled cold wake of Songda is consistent with remote sensing observations taken from AMSR-E swath data (Fig. 1.6), with similar spatial structure and SSTs in the core of the wake as low as $22^{\circ}C$ in both cases.

In Fig. 1.7, the recovery e-folding time ($\tau$) of the sea surface temperature

anomaly ($\Delta SST$) is presented, with means and standard deviations of those times calculated within the shown $\Delta SST$ bins. Dare and McBride (2011) calculated the SST recovery time for cold wakes found in the daily, 1/4° resolution Reynolds et al. (2007) SST analysis product. The position and time of cold wakes was determined for each storm in the IBTrACS during the 1981-2008 period, finding that surface cold anomalies were restored with an e-folding time ∼8.5 days. From the daily MOM output a local recovery e-folding time is calculated for every model grid point determined to be within the cold wake of either Hurricane Frances or Typhoon Songda. This recovery time is based on an exponential decay model $\Delta SST = \Delta SST_o \cdot e^{-(t-t_o)/\tau}$, where $\Delta SST_o$ is the initial SST cooling and $t_o$ is the time of storm passage for that location. Fig. 1.7 is produced from the results of this fit, with an average e-folding time ∼8.75 days, in good agreement with the findings of Dare and McBride (2011), and somewhat faster than the ∼11 day e-folding time derived by Mei and Pasquero (2013). As in the results of Dare and McBride (2011), recovery time shows no statistically significant dependence on the strength of initial cooling.

TC induced subsurface anomalies are addressed next. Fig. 1.8 illustrates the cross track structure of the cold wake behind Typhoon Songda, with the cold anomaly in the upper 50 $m$ centered ∼25 $km$ to the right of the storm track, corresponding to upward mixing and upwelling of thermocline waters into the mixed layer. Cooling directly below the track exceeds 750 $m$ depth, consistent with Ekman pumping induced by the strong TC wind stress curl, and is offset by downwelling centered around 500 $m$ depth and ∼150 $km$ from the storm track. Warming due to downward mixing of ML waters into the thermocline is present between 50 $m$ and 100 $m$ depth to the right and left of the storm track. Warming of ∼2.5°$C$ extends to nearly 200 $m$, at depths that have been attributed to non-linearities in the superposition of mixing-induced warming and downwelling (Vincent et al., 2013).

Mean temperature anomalies are calculated in the regions shown in Fig. 1.4, isolating the respective mixing effects of Frances and Songda while averaging out upwelling and downwelling effects. Immediately after storm passage there is surface cooling and subsurface warming (Fig. 1.9b). The depth and strength of mixing in the two storms is comparable, with Songda producing slightly more warming at depth, consistent with the stronger cold wake.

Ocean heat content anomaly ($\Delta OHC$), ocean heat loss (OHL), and ocean heat uptake (OHU) are used to quantify the bulk impact of TC heating and cooling. The OHC anomaly is defined as

$$\Delta OHC\,(t) = OHC_{TC}\,(t) - OHC_{con}\,(t) \tag{1.3}$$

where $OHC_{TC}$ and $OHC_{con}$ are the respective heat contents of the TC and control experiments calculated from Eq. 1.1a.

OHL and OHU decompose the heat content anomaly into shallow cooling and deep warming constituents

$$OHL\,(t) = c_p\rho_o \int_{z_1}^{0} dz \int_{x_w}^{x_e} dx \int_{y_s}^{y_n} dy \Delta T\,(x,y,z,t) \tag{1.4a}$$

$$OHU\,(t) = c_p\rho_o \int_{z_2}^{z_1} dz \int_{x_w}^{x_e} dx \int_{y_s}^{y_n} dy \Delta T\,(x,y,z,t) \tag{1.4b}$$

where $\Delta T = T_{TC} - T_{con}$. These integrals are first carried out horizontally, to obtain a heat anomaly profile with clear zeros crossings (Fig. 1.9b). OHL is integrated from the surface through the cold anomaly to the first zero crossing ($z_1$) and OHU from the first zero crossing until either the second zero crossing or, if one is not present, the warm anomaly has attenuated to 1% of its peak value ($z_2$).

Time series of OHL and OHU are calculated through 31 December as OHL is attenuated to zero by mid to late December for both Frances and Songda. For Frances, OHL reaches a maximum value of $2.6{\cdot}10^{20}J$ with an accompanying OHU of $2.9{\cdot}10^{20}J$, while Songda produces both OHL and OHU of $3.7{\cdot}10^{20}J$. OHU and OHL

approximately balance in both cases, indicating that prior to restoration heat has been well conserved over the integration depth. TC wind enhanced heat fluxes under the storm cool the ocean during TC passage, an effect that is underestimated in the uncoupled model as previously discussed. Direct extraction of heat by TC winds is relatively small but non-negligible contributor to TC induced cooling when compared to vertical mixing, contributing less than $10-15\%$ to the cooling (Price, 1981; Ginis, 2002). While this lower heat extraction provides for warmer surface waters available for mixing by the TC and thus may elevate OHU values (Vincent et al., 2012a), its contribution to the anomalous heating is expected to be small. The maximum OHU and OHL for Frances are reached on 7 September, two weeks after Frances formed. Maximum OHU is $\sim$10% higher than OHL, indicating that restoration of upper ocean cooling has begun even as the TC continues to mix the ocean elsewhere. This is consistent with the SST restoration timescale previously discussed. $\Delta OHC$ was $\sim$75% of the maximum OHU for Frances, an artifact of the chosen averaging domain capturing cooling due to uncompensated deep upwelling.

OHL decays with an e-folding time of $39 \pm 2$ days for Frances and $44 \pm 2$ days for Songda. This recovery time is significantly longer than that of the SST, consistent with the additional time needed for solar insolation and mixing to restore temperatures in the ML. Reduction of SSTs in the cold wake result in a dampening of the outgoing latent, sensible, and longwave heat fluxes in Songda's wake (Fig. 1.11). This reduction creates an imbalance between outgoing heat fluxes and the unperturbed incoming shortwave radiation at the ocean surface, resulting in an accumulation of $3.5 \cdot 10^{20} J$ of anomalous heat input by the time the CML is restored. This positive anomalous surface heat flux nearly balances the $3.6 \cdot 10^{20} J$ of upper thermocline OHU, closing the heat budget in the mixed layer.

The impact of individual storms is compared to the values from Emanuel (2001).

He found OHU from a single storm of $\sim 5 \cdot 10^{20} J$, given a wake of uniform width ($400km$), length ($2000km$), depth ($50\ m$) and cooling ($3°C$). The wakes of Frances and Songda have lengths $\sim$2000 $km$, widths $\sim$400 $km$, cooling to $\sim$50 $m$, and average $SST$ cooling of $3.25°C$ and $3.5°C$ respectively. While the wake characteristics are very similar, the OHU of Frances is $\sim$57% and Songda's $\sim$74% of Emanuel's estimates.

The discrepancy is due to the spatial variability of the modeled cooling. The SST anomaly quickly falls off with distance from the core of the cold wake, cooling at depth quickly approaches zero past a depth of $\sim$30 $m$, and the greatest cooling takes place only along the portion of the storm track where storm intensity and stratification are favorable. In light of this discrepancy, the idealized single storm estimate is considered an upper bound on storm impact.

### 1.3.2 Global and basin ocean temperature response

Shown in Fig. 1.12 are the SST and $\Delta SST$ fields on 1 October 2004 near the peak of northern TC activity. Strong cold wakes of recent TCs are present in the West Pacific (Typhoon Meari), East Pacific (Hurricane Javier), and North Atlantic (Hurricanes Jeanne, Karl, and Lisa). Weaker cooling is present where cold wakes have been partially restored in the weeks after storm passage (West Pacific Typhoons Songda and Aerie; East Pacific Hurricanes Howard and Isis; North Atlantic Hurricanes Frances and Ivan). Fig. 1.13 presents the accompanying subsurface temperature and temperature anomaly fields near 100 $m$. Warming from mixing and downwelling is present throughout the TC forcing regions, persisting long after the surface cooling has been restored. Cooling due to Ekman pumping (upwelling) accompanies many of these warm anomalies, but the anomaly field at depth is dominated by warming.

Fig. 1.14 shows TC induced temperature anomalies averaged laterally across the basins described in Table 1.3, on 1 October 2004 and 31 May 2005. The different averaging areas are reflected in the differing $\Delta T$ axes between the global and hemi-

sphere means (Fig. 1.14a,f) and basin means (Fig. 1.14b,c,d,e). The global anomaly (Fig. 1.14a) displays cooling to $\sim$40 $m$ on 1 October with maximum warming at $\sim$60 $m$ and extending deeper than 300 $m$. By 31 May 2005, only the deep, persistent warming remains, with a maximum at $\sim$90 $m$ and magnitude comparable to that in October.

The West Pacific, East Pacific, and North Atlantic have cooling on 1 October down to $\sim$50 $m$, 30 $m$, and 40 $m$ respectively (Fig. 1.14b,c,d). West Pacific warming has a deeper and broader peak than either the North Atlantic or East Pacific, while the East Pacific warming is both the shallowest and weakest. This inter-basin variability is due to differences in TC forcing and local stratification, with those regions with the greatest forcing (West Pacific and North Atlantic) and with deeper mixed layers (West Pacific) having stronger and deeper warming.

Cooling in the North Atlantic has vanished by 31 May, with a weaker and deeper warm anomaly centered around 100 $m$. The East Pacific warm anomaly on 31 May is nearly as strong as that on 1 October and has deepened by $\sim$60 $m$. The West Pacific has two peaks of weaker persistent warming, one shallower ($\sim$50 $m$) and the other deeper ($\sim$160 $m$) than on 1 October. The reasons for these differences, especially the strong, deep 31 May warming in the East Pacific and weakened, bifurcated warming in the West Pacific will be discussed in Section 3e.

The North Indian Ocean, consistent with its weakened and offset TC season has nearly zero subsurface accumulation on 1 October (Fig. 1.14e). By 31 May there is strong warming centered on 110 $m$. In the Southern Hemisphere (Fig. 1.14f) there is a weak warming at depth on 1 October, centered on 150 $m$. 1 October is before the start of austral TC activity, and so is not attributed to direct storm forcing. By 31 May, there is a sharp warming centered on 95 $m$. The origin of this deep anomalous heating at times and locations removed from TC induced mixing will be explored in

Section 3e.

### 1.3.3 Ocean heat uptake

Fig. 1.15 illustrates the OHL (Eq. 1.4a), OHU (Eq. 1.4b), and $\Delta OHC$ (Eq. 1.3) calculated from the global temperature anomaly profile (Fig. 1.14a). A 15-day low pass filter is applied to the resulting time series, in order to emphasize seasonal to interseasonal trends. OHL increases slowly before accelerating with increased storm activity in August, reaching a peak of $1.7 \cdot 10^{21} J$ at the beginning of October. Global OHL subsequently decays until there is none remaining by February, indicating that on average the CML has been restored.

OHU temporal structure mirrors that of OHL through October, with anomalous heating increasing slowly through August, and then accelerating before leveling off at $\sim 4.1 \cdot 10^{21} J$, which is approximately 3% of the maximum amplitude of global seasonal OHC (Table 1.4), and somewhat lower than the heat uptake derived from SSH anomalies by Mei et al. (2013) ($1.01 \pm 0.46 \cdot 10^{22} J$). OHU continues to increase slowly through January, before decreasing slightly to $3.9 \cdot 10^{21} J$. Increasing $\Delta OHC$ lags OHU as in the Frances and Songda cases, with the difference between the two equivalent to the OHL. February $\Delta OHC$ values are comparable to OHU, by which time mean restoration of the global CML has occurred, giving confidence that OHU is capturing the warming anomaly in a globally averaged sense.

A globally averaged OHU rate can be derived from a linear fit to the OHU time series in Fig. 1.15. An annual OHU rate of $0.13 \pm 0.09$ $PW$ is found for 1 June 2004-31 May 2005, with $R^2 = 0.69$. A seasonal rate of $0.47 \pm 0.02$ $PW$ with $R^2 = 0.98$ is found by constraining the fit to the period of peak OHU (20 July-28 October 2004). This difference in uptake rate and $R^2$ supports the hypothesis that the effect of TC induced heating on the ocean is poorly represented by a bulk annual heating rate.

As in past studies, we find the mean annual OHU rate to be a useful method of

comparison, despite its acknowledged shortcomings in capturing the full spatial and temporal variability of TC thermocline heating. The annual OHU rate is consistent with the Argo float estimates of Park et al. (2011) ($0.19 \pm 0.03\ PW$) and the $0.15\ PW$ rate of Jansen et al. (2010), which accounts for the effect of reventilation of thermocline thermal anomalies via the so-called "Stommel demon" associated with seasonal advection of subsurface heat anomalies around the subtropical gyre (Stommel, 1979). The annual rate is lower than the findings of Sriver and Huber (2007) ($0.26\ PW$) and the "doubled wind" experiment of Sriver and Huber (2010) ($0.3\ PW$), which they considered to be the most physically representative. Both rates are significantly lower than the estimates of Emanuel (2001) ($1.4 \pm 0.7\ PW$), the peak values of Sriver et al. (2008) ($0.6\ PW$), and the unventilated values of Jansen et al. (2010), again suggesting that a realistic representation of oceanic processes is critical in capturing TC induced heating. Both the annual and seasonal rates are consistent with the recent estimates of Mei et al. (2013) ($0.32 \pm 0.15\ PW$).

Fig. 1.16 shows the ocean basin cooling response to TC forcing, where OHL has been integrated across those basins defined in Table 1.3. The strongest OHL is seen in the North Atlantic (peaking at $8 \cdot 10^{20} J$ on 5 October) and the West Pacific (peaking at $7 \cdot 10^{20} J$ on 1 September). While its peak is lower, the West Pacific OHL is broader, consistent with the longer West Pacific TC season. The East Pacific and Southern Hemisphere have weaker OHL, peaking in late September and mid-April respectively, again consistent with the timing and duration of direct TC forcing in those regions.

Basin integrated OHU is shown in Fig. 1.16b, with maxima shown in Table 1.4. Similar to the Frances, Songda, and Global OHU calculations, the initial heat uptake follows the structure of the accompanying OHL. North Atlantic OHU peaks in early October before gradually falling by 50% by 31 May 2005. West Pacific OHU peaks

in early November, at a lower value than the North Atlantic peak despite the greater local TC forcing. OHU in the West Pacific decreases rapidly between November and March, with less than 1/3 of the maximum heating remaining on 31 May.

In contrast, East Pacific OHU peaks at $\sim 6 \cdot 10^{20} J$, and subsequently increases by $\sim$1/3 after the conclusion of local TC activity. OHU in the Southern Hemisphere begins to accumulate during the northern summer, increasing rapidly in November before leveling off in February. There is a slight decrease in Southern Hemisphere OHU in March, followed by an increase that corresponds with local TC activity. The North Indian Ocean sees a small accumulation through the course of the northern winter.

Comparisons of basin peak OHU to 1/2 the local summer-winter difference in $\Delta OHC_{season}$ are presented in Table 1.4. In the dominant TC regions, TC induced OHU can reach values up to 10% of the maximum seasonal amplitude. While the relative impact of TC OHU in the Southern Hemisphere is lower ($\sim$3%) it is still considerable given the lower direct TC forcing and size of the basin (Table 1.3).

The striking behavior of West Pacific, East Pacific, and Southern Hemisphere TC induced OHU bears deeper analysis, specifically the reasons for their apparently compensatory variability. The heat anomaly budget for the region delineated by the dashed box in Fig. 1.12b and 1.13b is calculated (Fig. 1.17) to understand the reasons for the drastic drop in West Pacific OHU. Accumulated anomalous heating through the ocean surface results in a warming of the ocean. There is a strong and rapid accumulation of anomalous ocean heat transport

$$\Sigma \Delta OHT\,(y,t) = c_p \rho_o \int_{x_w}^{x_e} dx \int_0^H dz \int_0^t dt' \Delta\,(v \cdot T) \tag{1.5a}$$

$$\Delta\,(v \cdot T) = v_{TC} \cdot T_{TC} - v_{con} \cdot T_{con} \tag{1.5b}$$

across the southern boundary. This southward heat export continues through January, with a peak value $\sim 2.75 \cdot 10^{21} J$ before turning northward. A considerably weaker

and slower zonal export of anomalous heat occurs at the eastern boundary. The surface and advective forcing are balanced by a regional change in OHC (Eq. 1.3). This analysis indicates that the drop in West Pacific OHU in Fig. 1.16b is consistent with a redistribution of anomalous heat from the subtropical to the tropical Pacific.

### 1.3.4 Meridional transport

Fig. 1.18a shows the meridional distribution of OHU, integrated 360° zonally. Initially, anomalous heat accumulates between $10°N$ and $40°N$, before decreasing through the northern autumn and winter. OHU between $10°S$ and $10°N$, where there is little to no TC activity, increases as that north of $10°N$ attenuates. By 31 May the largest TC induced heat anomaly is in the deep tropics, with a significant amount remaining in the northern subtropics and a smaller amount having accumulated in the southern subtropics due to austral TC activity. This distribution of OHU illustrates that the southward export of heat from TC forcing regions results in a convergence of heat in the tropics.

Heat export and convergence is more clearly seen in Fig. 1.18b, where Eq. 1.5a has been integrated around the globe every 10° from $30°S$ to $30°N$, producing time series of the accumulated meridional TC induced heat transport anomaly. There is a clear southward transport in the northern hemisphere starting in late summer. This OHT anomaly strengthens between $20°N$ and $10°N$ before penetrating across the equator. By $10°S$ there is no further transport accumulation, confirming the convergence of heat in the equatorial region.

The temporal structure and magnitude of the global OHT anomaly accumulation across $10°N$ is consistent with that across the southern boundary of the West Pacific control volume analyzed in Fig. 1.17, establishing that the equatorial $\Delta OHT$ convergence is dominated by export of TC induced OHU out of the subtropical West Pacific. For this reason, the remainder of the analysis focuses on the West Pacific

transport and circulation. While there is a significant decrease in OHU in the North Atlantic between November and May (∼50%), it is not associated with export of heat to the tropical Atlantic. Rather, this decrease is likely due to the reventilation mechanism of Jansen et al. (2010).

### 1.3.5 Subtropical-tropical interaction

The currents in the West Pacific upper-thermocline are shown in Fig. 1.19. Zonal and meridional currents are averaged from 56 $m$ to 253 $m$ to capture the flow field over the depths where TC mixing deposits heat. The region shown contains nearly all of the West Pacific TC activity (Fig. 1.2). Zonal flow is predominantly westward, carrying TC induced heat anomalies towards the western boundary, where they enter either the Kuroshio Current to be advected poleward or the Mindanao Current to be advected into the deep tropics. Whether a water mass enters the Kuroshio or Mindanao is determined by its latitude upon reaching the western boundary and the location of the bifurcation of the North Equatorial Current (NEC).

The location of the NEC bifurcation varies seasonally, consistent with the observational findings of Qu and Lukas (2003) who hypothesized that changes in local Ekman pumping associated with monsoonal winds alter the circulation such that the bifurcation reaches its northernmost location between November and December, before migrating south through July. The bifurcation point is around $15°N$ between August and October (Fig. 1.19a), $16°N$ between November and January (Fig. 1.19b), and as far south as $12°N$ between February and April (Fig. 1.19c). Times when the bifurcation is further to the north correspond with elevated anomalous heat transport into the tropics, with the proportion of mid-gyre waters flowing into the Mindanao elevated relative to the annual mean.

Warm anomalies are advected equatorward as part of the subtropical cell (McCreary and Lu, 1994). Large scale southward deflection of the NEC between $125°E$

and $130°E$ in the November-January period further enhances the flow into the Mindanao, corresponding with the period of greatest $\Delta OHT$ into the tropics. The late winter period February-April sees a relaxation of the currents consistent with the reduced wind stress curl during the southwest monsoon. Meridional flow in the mid-gyre region ($130°E-150°E$) is now predominantly northward, with waters from the tropics penetrating the gyre interior and entering the Kuroshio. This seasonality in the regional flow results in a reversal of the total regional OHT integrated along the equator and $10°N$, in phase with the reversal in $\Delta OHT$ seen in Fig. 1.17 and 1.18b, providing a physical explanation for the return of anomalous heat to the subtropics.

The model representation of the mean annual equatorial circulation averaged from 56 $m-330$ $m$ is shown in Fig. 1.20. The current experimental design allows for a reasonable representation of the low latitude western boundary currents in the Pacific, and produces a well-resolved Indonesian Throughflow. For example, the Makassar Strait, one of the narrowest choke points in the region has a $\sim$10 grid point representation at this resolution. The rapid flow in the Mindanao is clearly displayed, feeding into the Indonesian Throughflow west of $120°E$ and the Equatorial Undercurrent (EUC) east of the Philippines and eastward into the open Pacific. We estimate that of the $\sim 2.9 \cdot 10^{21} J$ of accumulated $\Delta OHT$ from the Mindanao Current, nearly $0.9 \cdot 10^{21} J$ enters the Indonesian Throughflow via the Makassar Strait, with the rest progressing east via the EUC. This partitioning of the anomalous heat transport between the Indonesian Throughflow and EUC is consistent with observations of the mean volume transport, where $9.3 \pm 2.5$ $Sv$ passes through the Makassar Strait (Gordon et al., 1999) out of the $25-35$ $Sv$ of mean southward transport in the Mindanao (Lukas, 1988). The MOM representation of the EUC reaches speeds exceeding 1 $m\ s^{-1}$ and is sharply sloped zonally along isopycnals, consistent with observations (e.g., see Fig. 13 in Griffies et al. (2009)). Advection by the EUC would

serve as a rapid mechanism of zonal OHU redistribution should TC induced warm anomalies reach the undercurrent. On the eastern boundary, the coastal undercurrent off of Peru (Brockmann et al., 1980) would serve to advect anomalous heat from the tropical East Pacific north of the equator into the Southern Hemisphere, accounting for the offsetting changes in East Pacific and Southern Hemisphere OHU (Fig. 1.16a) seen in April.

For TC heat anomalies to enter the undercurrent, water parcels must reach nearly 100 $m$−200 $m$ depth by the time they enter the deep tropics. Fig. 1.21 shows temperature anomalies averaged from 120°$E$−150°$E$, that being the dominant region of equatorward transport. Most anomalous heat is deposited north of 15°$N$ and below 60m. Meridional flow takes place primarily along isopycnal pathways, subducting water masses as they are advected equatorward (Rothstein et al., 1998; McCreary and Lu, 1994). Advection of warm anomalies is inferred along the 1031−1032 $kg\ m^{-3}$ isopycnals in Fig. 1.21a during the autumn, causing the anomalies to deepen until they intersect with the EUC. Relatively little anomalous heat remains in the Western Pacific south of 10°$N$, implying that the EUC is in fact exporting heat eastward. Some heat anomalies remain at depth in the subtropics during the winter to be ventilated by winter mixed layer deepening (Fig. 1.21b). A persistent upwelling centered around 15°$N$ and flanking downwelling is a prominent feature seen in Fig. 1.21a, resulting from multiple TCs propagating predominantly westward in the region (Fig. 1.2) and subsequent reinforcement of the storm induced Ekman pumping. This cumulative Ekman pumping produces anomalous zonal currents due to the thermal wind balance, directed westward on the northern and eastward on the southern edge of the upwelling region. These currents are expected to be weaker than the mean currents associated with the subtropical gyre, which are primarily responsible for advection of the TC induced heat anomalies.

Fig. 1.22 presents the mean monthly temperature anomalies from $5°S-5°N$. TC induced warm anomalies generated in the subtropics reach the tropics between late July and early August (1.22b-c). Advection within the EUC moves the warm anomalies entering the equatorial Pacific eastward. Warm anomalies can also be carried by eastward propagating Kelvin and Yanai waves excited by West Pacific TCs as demonstrated by Sriver et al. (2013). The phase speeds of the first and second baroclinic Kelvin modes are similar to the EUC velocity. The vertically coherent warm and cold anomalies present in Fig. 1.22e-l are due to the phase differences in tropical instability waves between our two simulations. These phase differences are not expected to contribute to the zonal heat transport.

Warm anomalies reach the East Pacific by mid-autumn, shoaling along the thermocline (Fig. 1.22a-e). Thermocline warm anomalies in the West Pacific are significantly diminished between March and May while persisting in the East Pacific (Fig. 1.22j-l). This behavior is consistent with the seasonal generation of TC induced warm anomalies in the West Pacific.

Rapid relocation of TC induced warm anomalies via the West Pacific subtropical cell, Mindanao Current, EUC, and equatorial waves explains the rapid decrease of OHU in the West Pacific between November and February seen in Fig. 1.16b. This connection between West Pacific TC activity and warming of East Pacific tropical thermocline waters occurs on timescales of less than one year.

## 1.4 Discussion

The interaction of tropical cyclones with the ocean produces a non-negligible heating of the thermocline with potential implications for the ocean climate system. Though a global phenomena, viewing the impact of tropical cyclones (TCs) on the ocean on a regional basis sheds light on the physical mechanisms driving the generation and redistribution of TC induced Ocean Heat Uptake (OHU). Our estimates of

global heat uptake magnitude and rates are consistent with the results of recent observational and modeling studies. We find that TC induced heat uptake can augment the basin heat content by up to 10% of the maximum local seasonal amplitude in those basins with the greatest storm activity. Results from our study are subject to uncertainties associated with model formulation (e.g., parameterizations), grid resolution, and biases due to the lack of atmospheric coupling. We therefore recommend further examinations in global eddying simulations of the mechanisms for TC induced heat transport and quantitative estimates of OHU.

Due to the single year of model integration and analysis, we are unable to address questions related to the poleward export of anomalous heating through the Atlantic meridional overturning circulation predicted by previous studies (Emanuel, 2001; Jansen et al., 2010; Sriver and Huber, 2010; Manucharyan et al., 2011; Scoccimarro et al., 2011). Rather, our analysis identifies a rapid equatorial convergence of heat through the shallower and more rapid wind driven West Pacific subtropical cell. The intense currents near the western boundaries of the ocean basins play a key role, especially in the West Pacific. We do not see this behavior as contradicting findings of poleward transport, but as taking place in parallel and on shorter timescales.

TC induced warm anomalies are efficiently exported to the tropics, where they are moved zonally into the tropical East Pacific by the EUC and equatorial waves. This behavior is consistent with the findings of Manucharyan et al. (2011), but shows strong heat accumulation in the East Pacific over shorter timescales. Convergence of anomalous TC heating in the equatorial East Pacific could have climate implications on inter-annual timescales, with the possibility for modulation of the El Niño-Southern Oscillation (ENSO) (Fedorov et al., 2010).

Our analysis of a single season has provided insight into the potential effect of tropical cyclones on the ocean climate system. Nonetheless, many questions re-

main unaddressed. While we have traced some of the dominant pathways by which anomalous heat is redistributed, a further analysis of the physics of this transport is warranted, as is the study of the fate of these anomalies through subsequent TC seasons. Future work should also address how representative the impact of 1 June 2004-31 May 2005 TC activity is, and if there is a multi-year accumulated effect of storm induced heating. If this heating does continue to accumulate, the mechanisms by which the ocean eventually discharges it in order to remain in thermodynamic balance must be explained, be it by reventilation or interaction with and discharge by ENSO or other large-scale climate processes.

Table 1.1. Sample TCVitals for Hurricane Frances position, central pressure, environmental pressure, maximum wind speed, radius of last closed isobar, radius of maximum wind, radii with wind speed of 18 $m\ s^{-1}$ and 26 $m\ s^{-1}$ in all quadrants (NE, SE, SW, and NW).

| | Position | | Pressure (mb) | | | Radius (km) | | | | | | | | | |
|---|---|---|---|---|---|---|---|---|---|---|---|---|---|---|---|
| | | | | | | | | 18 $m\ s^{-1}$ | | | | 26 $m\ s^{-1}$ | | | |
| Date/Time | Lat (°N) | Lon (°W) | Central | Env | Max Wind Speed ($m\ s^{-1}$) | Last Closed Isobar | Max Wind | NE | SE | SW | NW | NE | SE | SW | NW |
| 200408310000 | 19.6 | 60.7 | 945 | 1012 | 57 | 371 | 28 | 278 | 241 | 185 | 278 | 167 | 148 | 130 | 167 |
| 200408310600 | 19.8 | 62.1 | 951 | 1012 | 57 | 371 | 37 | 278 | 241 | 185 | 278 | 167 | 148 | 130 | 167 |
| 200408311200 | 19.9 | 63.3 | 950 | 1012 | 59 | 371 | 37 | 278 | 241 | 185 | 278 | 167 | 167 | 130 | 167 |
| 200408311800 | 20.3 | 65.1 | 942 | 1012 | 62 | 371 | 37 | 278 | 241 | 185 | 278 | 185 | 185 | 139 | 185 |
| 200409010000 | 20.7 | 66.3 | 939 | 1012 | 62 | 371 | 28 | 278 | 241 | 185 | 278 | 185 | 185 | 139 | 185 |
| 200409010600 | 21.0 | 67.9 | 939 | 1012 | 62 | 371 | 28 | 297 | 241 | 185 | 278 | 222 | 185 | 139 | 185 |
| 200409011200 | 21.4 | 69.1 | 937 | 1012 | 62 | 371 | 28 | 297 | 241 | 185 | 278 | 222 | 185 | 139 | 185 |
| 200409011800 | 21.8 | 70.6 | 941 | 1012 | 62 | 371 | 28 | 297 | 241 | 148 | 278 | 222 | 139 | 111 | 139 |

Table 1.2. Sample TCVitals for Typhoon Songda position, central pressure, environmental pressure, maximum wind speed, radius of last closed isobar, radius of maximum wind, radii with wind speed of 18 $m\ s{-}1$ in all quadrants (NE, SE, SW, and NW). 26 $m\ s^{-1}$ wind radii are not present in JTWC records.

| | Position | | Pressure (mb) | | | Radius (km) | | | | | | | | | |
|---|---|---|---|---|---|---|---|---|---|---|---|---|---|---|---|
| | | | | | | | | 18 $m\ s^{-1}$ | | | | 26 $m\ s^{-1}$ | | | |
| Date/Time | Lat (°N) | Lon (°E) | Central | Env | Max Wind Speed ($m\ s^{-1}$) | Last Closed Isobar | Max Wind | NE | SE | SW | NW | NE | SE | SW | NW |
| 200409010000 | 18.4 | 146.3 | 916 | 1000 | 64 | 370 | 19 | 278 | 241 | 0333 | 0278 | - | - | - | - |
| 200409010600 | 19.6 | 145.4 | 916 | 1001 | 64 | 370 | 28 | 222 | 222 | 0222 | 0222 | - | - | - | - |
| 200409011200 | 20.2 | 143.5 | 916 | 1001 | 64 | 370 | 28 | 278 | 278 | 0278 | 0278 | - | - | - | - |
| 200409011800 | 20.8 | 142.3 | 916 | 1001 | 64 | 370 | 28 | 278 | 278 | 0278 | 0278 | - | - | - | - |
| 200409020000 | 21.1 | 141.1 | 922 | 1001 | 62 | 370 | 28 | 278 | 278 | 0278 | 0278 | - | - | - | - |
| 200409020600 | 21.7 | 139.9 | 933 | 1001 | 57 | 370 | 19 | 148 | 278 | 0278 | 0148 | - | - | - | - |
| 200409021200 | 21.9 | 138.4 | 938 | 1001 | 54 | 370 | 19 | 204 | 278 | 0278 | 0204 | - | - | - | - |
| 200409021800 | 21.9 | 137.4 | 933 | 1001 | 57 | 370 | 19 | 204 | 278 | 0278 | 0204 | - | - | - | - |

Table 1.3. Geographical boundaries and ocean surface area of TC ocean basins.

| Basin | Lon. Bounds | Lat. Bounds | Area (million $km^2$) |
|---|---|---|---|
| Globe | 180°W-180°E | 80°S-90°N | 358.63 |
| West Pacific | 98°E-180°E | 0°-90°N | 39.916 |
| East Pacific | 180°W-100°W* | 0°-90°N | 47.719 |
| North Atlantic | 100°W*-20°E | 0°-90°N | 49.52 |
| North Indian Ocean | 20°E-98°E | 0°-90°N | 15.115 |
| Southern Hemisphere | 180°W-180°E | 80°S-0° | 206.32 |

*South of 17°N the boundary between the East Pacific and North Atlantic is defined by the Central American isthmus and South American continent.

Table 1.4. Maximum global and basin ocean heat uptake, compared to the local maximum of the $\Delta OHC_{season}$ amplitude calculated to 729m (Eq. 1.2). Timing of Maximum OHU are those found in Fig. 1.16.

| Basin | Max OHU ($10^{21}J$) | $\Delta OHC_{season}$ ($10^{21}J$) | $OHU/\Delta OHC_{season}$ |
|---|---|---|---|
| Global | 4.10 | 135.7 | 3.0% |
| West Pacific | 1.52 | 16.9 | 9.0% |
| East Pacific | 1.72 | 17.2 | 10.0% |
| North Atlantic | 1.70 | 26.2 | 6.5% |
| North Indian Ocean | 0.31 | 7.3 | 4.2% |
| Southern Hemisphere | 2.50 | 83.2 | 3.0% |

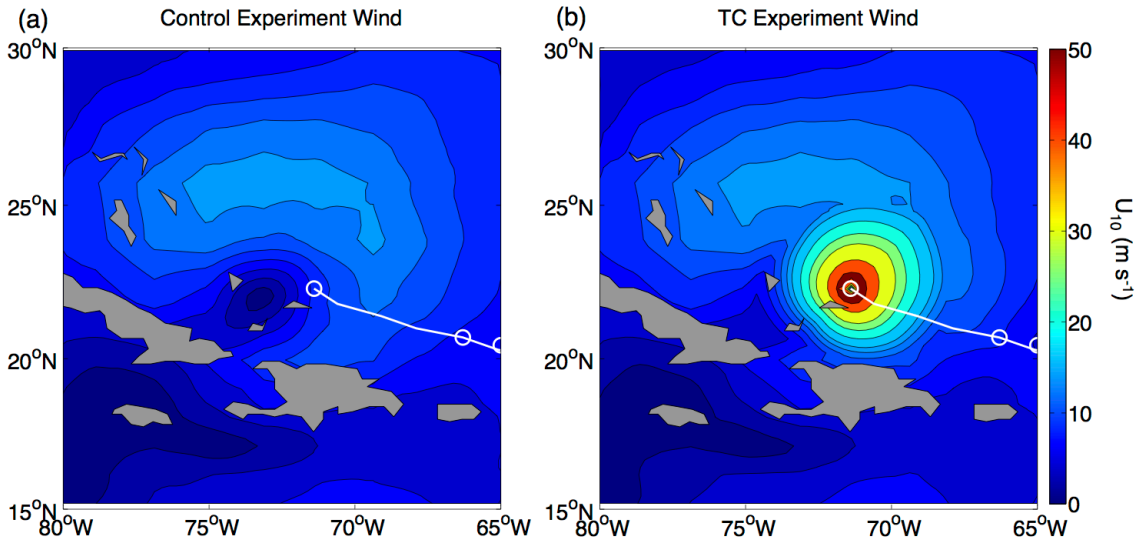


Figure 1.1. 10 $m$ wind speed magnitude during Hurricane Frances from the control experiment (a) and with the embedded TC (b).

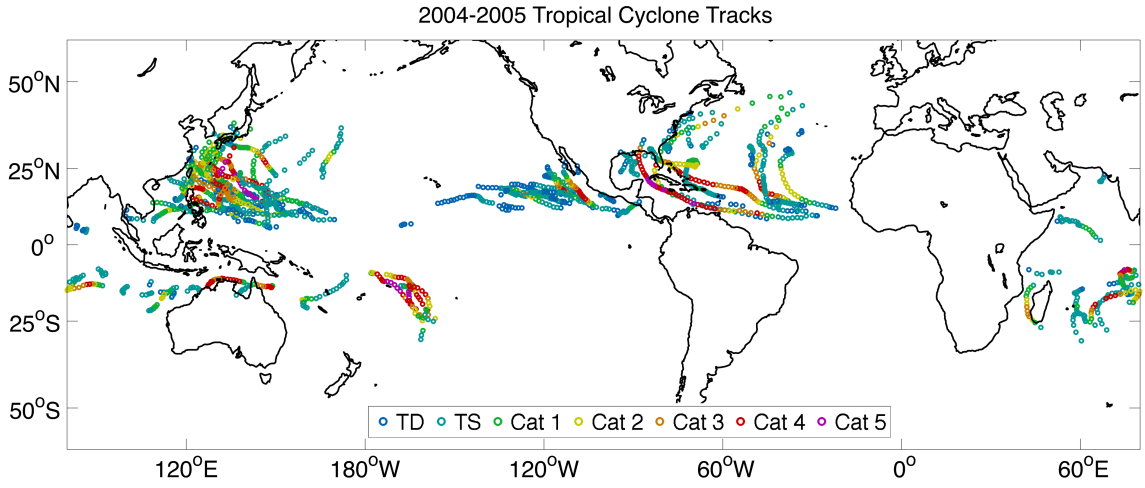


Figure 1.2. Global TC tracks from 1 June 2004 through 31 May 2005, colored by storm intensity.

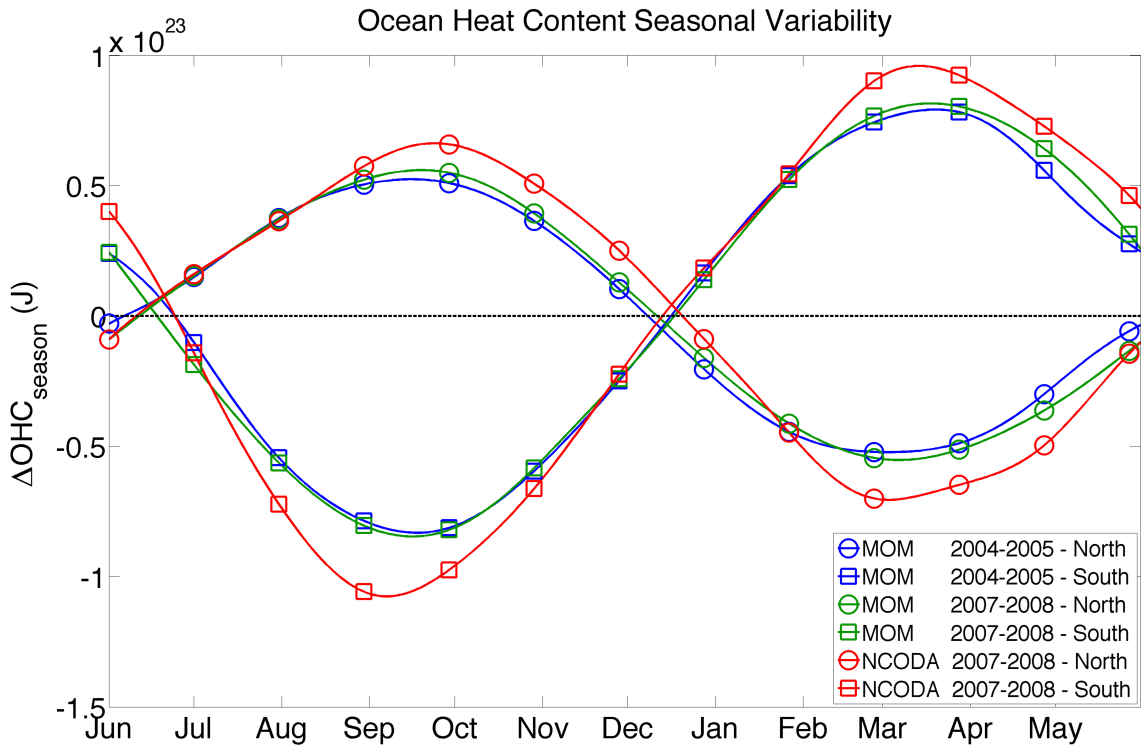


Figure 1.3. Northern and Southern Hemisphere seasonal variability ($\Delta OHC_{season}$) from 1 June 2004-31 May 2005 in MOM, 1 June 2007-31 May 2007 in MOM, and 1 June 2007-31 May 2007 in NCODA.

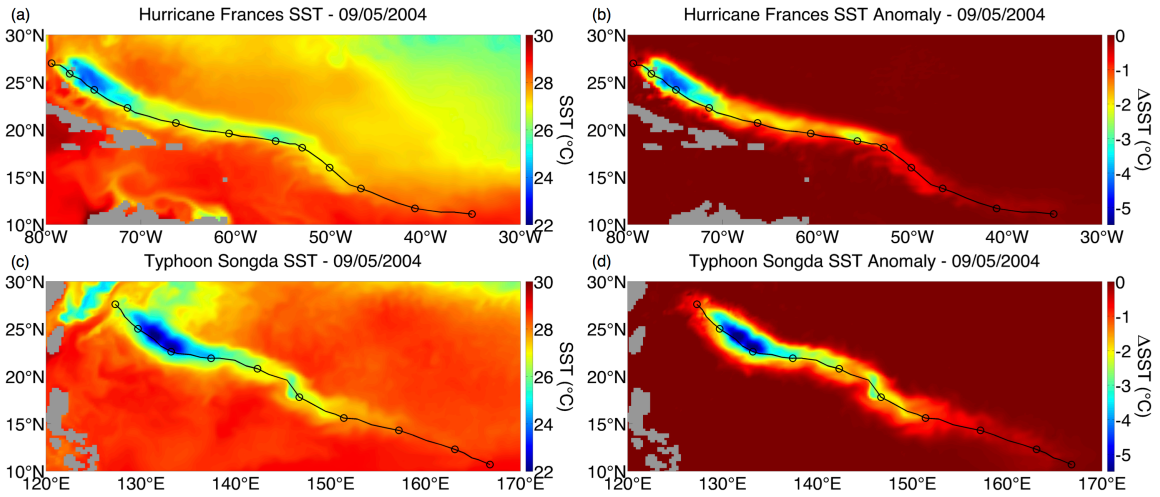


Figure 1.4. Sea surface temperature and SST anomaly fields following passage of Hurricane Frances (a,b) and Typhoon Songda (c,d) with daily track positions on 5 September 2004.

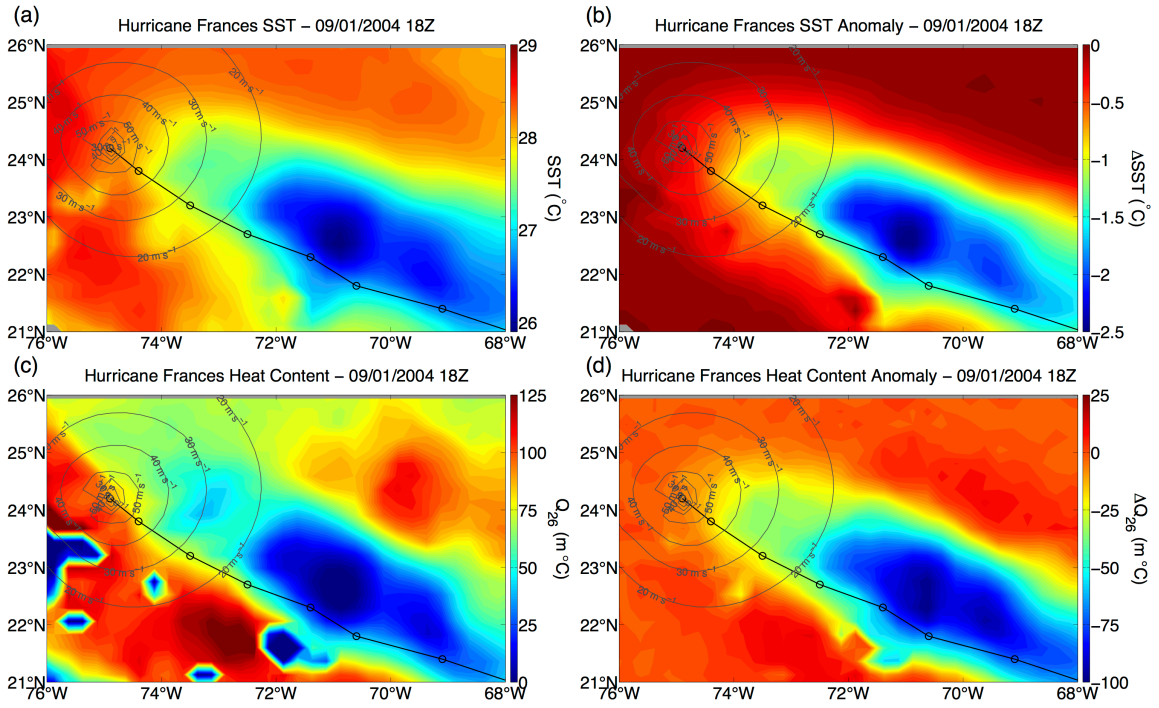


Figure 1.5. Sea surface temperature (a), SST anomaly (b), heat content (c), and heat content anomaly (d) integrated to the $26°C$ isotherm during passage of Hurricane Frances. Wind speed contours and track position are superimposed in grey and black, respectively. The domain limits were selected to approximate those of D'Asaro et al. (2007)

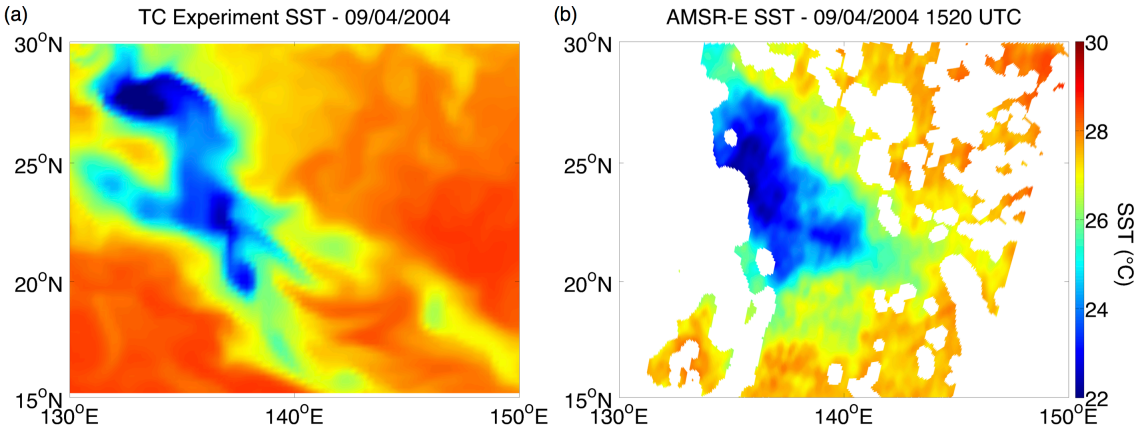


Figure 1.6. Sea surface temperature from MOM (a) and AMSR-E Level 2 satellite swath (b) following passage of Typhoons Songda (27 August-7 September 2004) and Chaba (17 August-31 August 2004). The magnitude and extent of cooling are comparable in the model and satellite data.

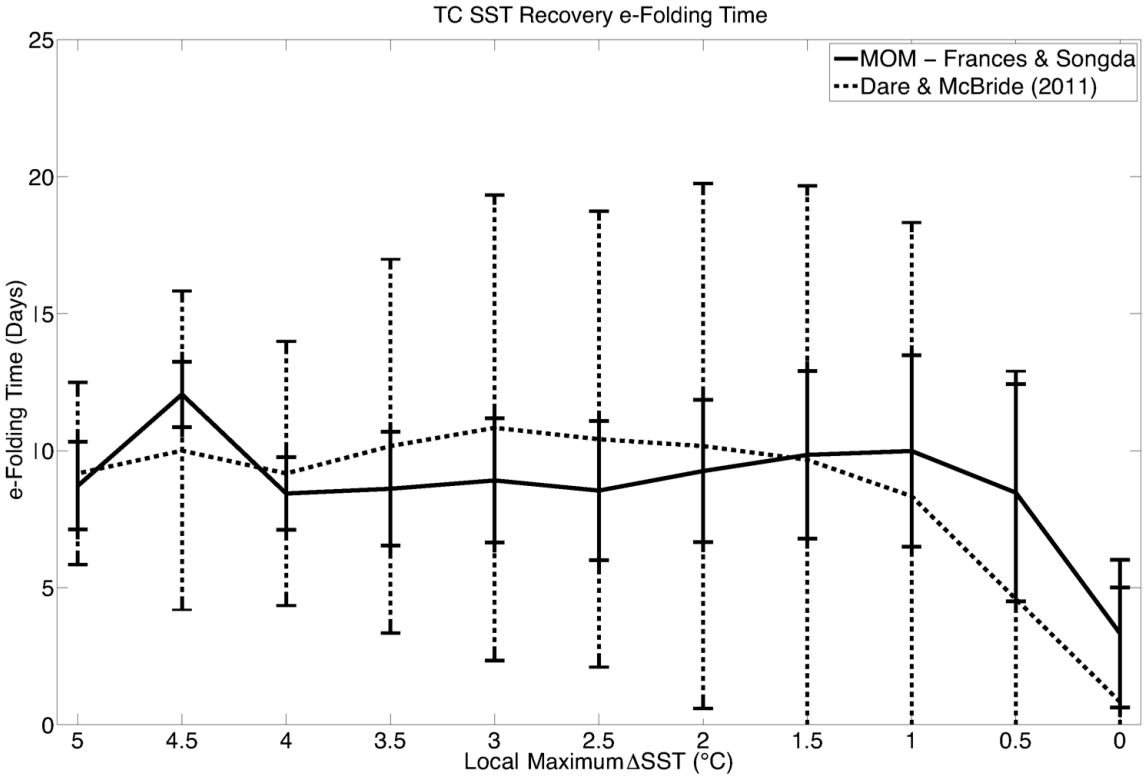


Figure 1.7. SST recovery e-folding time following TC passage (solid), compared with results of Dare and McBride (2011) (dashed). Bars are the standard error on each $0.5°C$ $\Delta$SST bin.

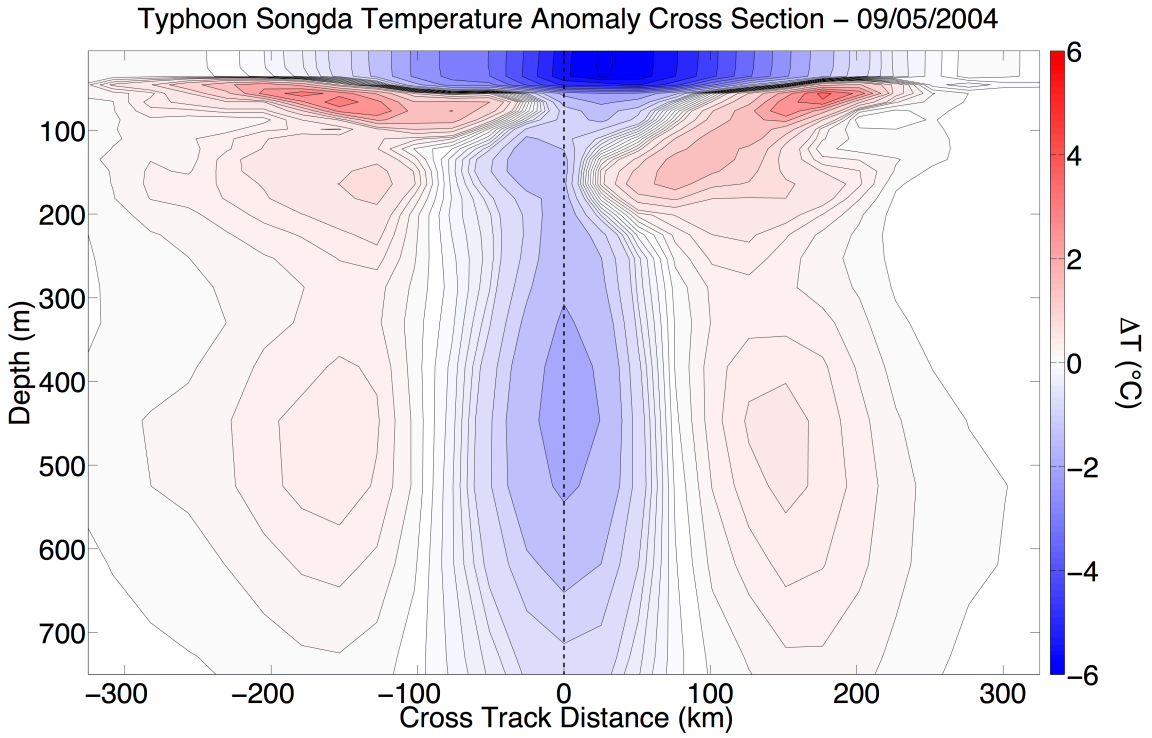


Figure 1.8. Temperature anomaly cross section, taken across the wake of Typhoon Songda centered on $131.6°E$, $24.1°N$. Positive (negative) cross track distances are to the right (left) of the track when oriented in the direction of storm translation.

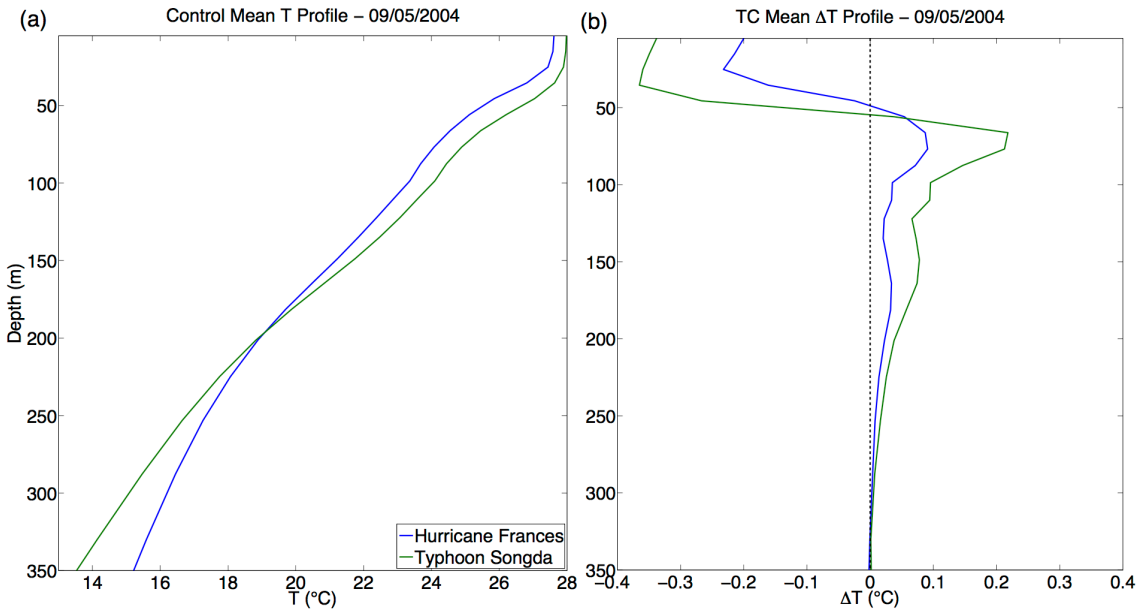


Figure 1.9. Temperature profile in the control experiment (a) and anomaly due to TC passage (b) on 5 September 2004, averaged horizontally over the domains shown in Fig. 1.4.

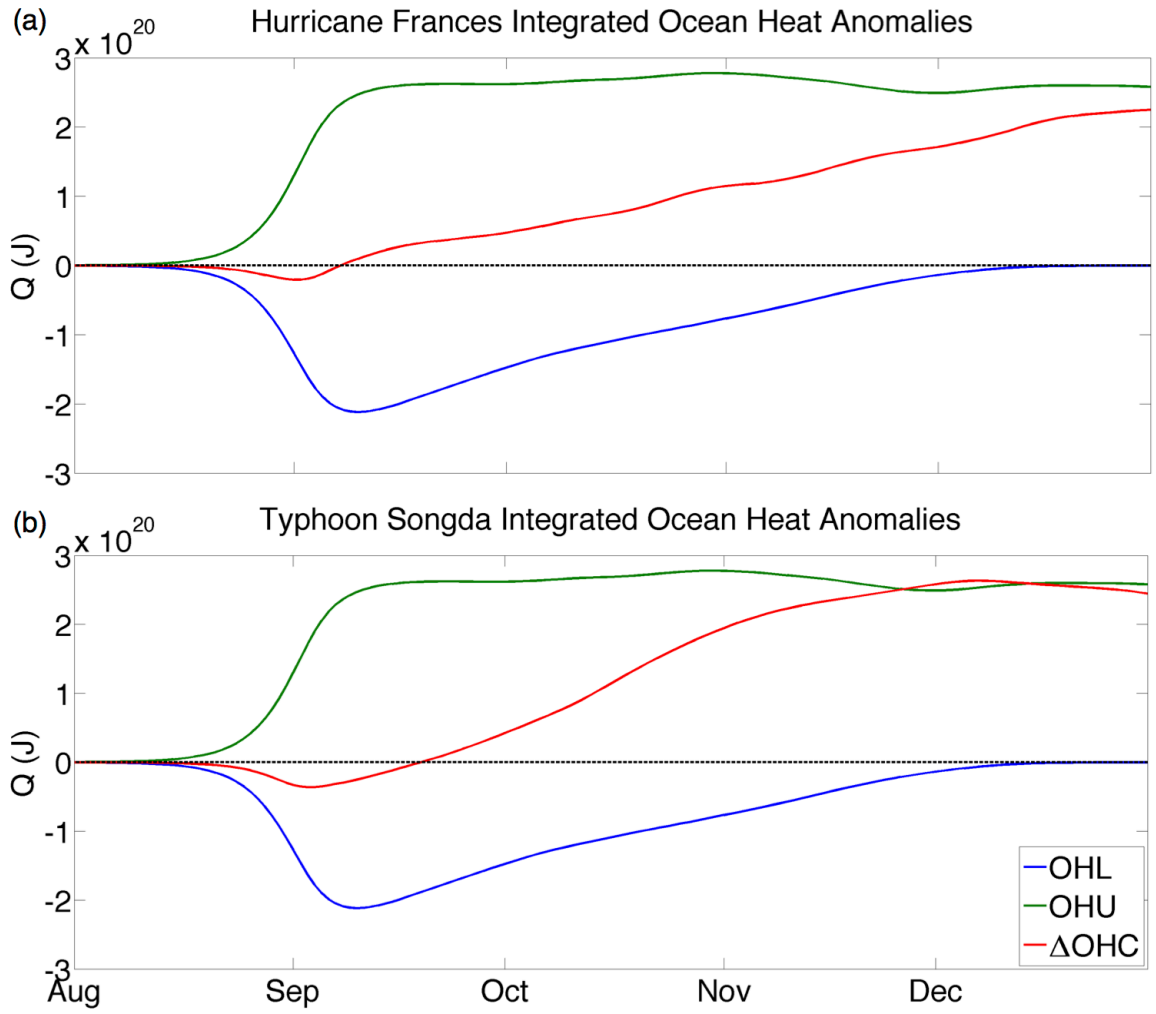


Figure 1.10. Time series of the ocean heat loss, uptake, and content anomaly during and following passage of Hurricane Frances (a) and Typhoon Songda (b), integrated across the North Atlantic and Pacific respectively from 1 August 2004-31 December 2004.

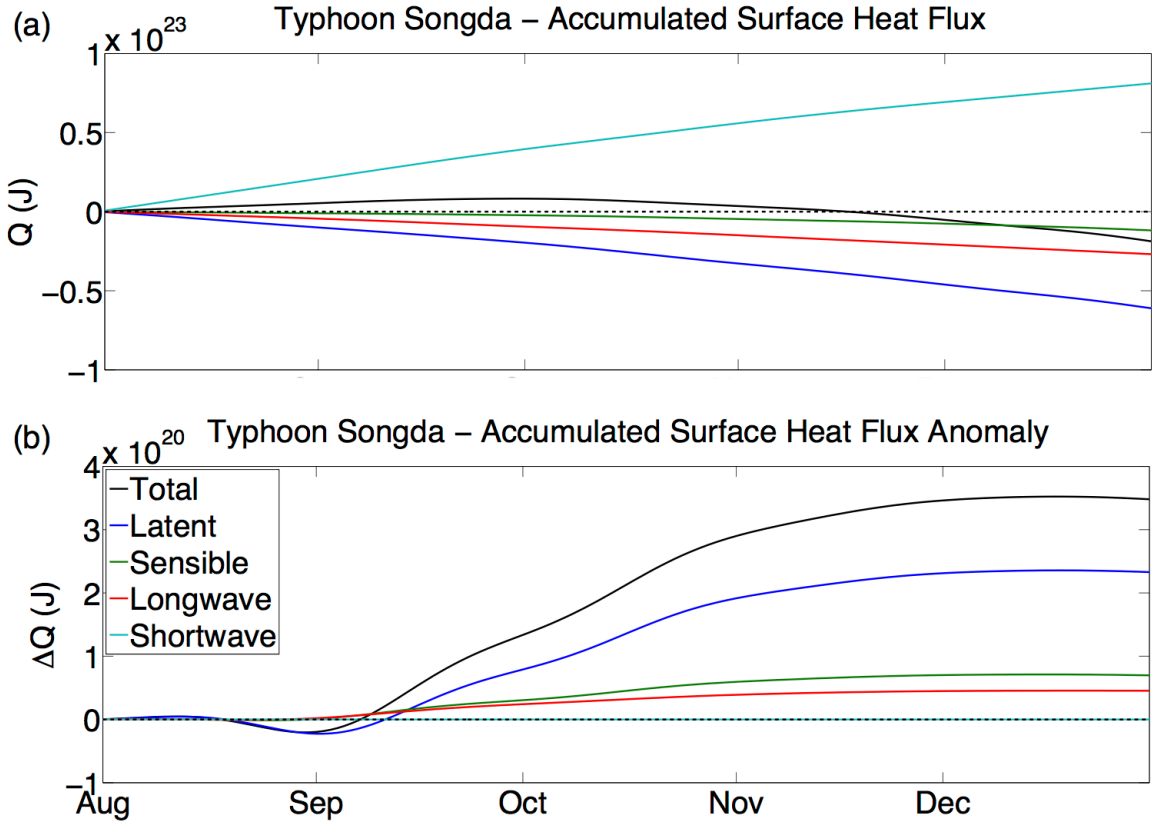


Figure 1.11. Accumulated surface heat flux (a) and heat flux anomaly (b) following passage of Typhoon Songda, with positive values indicating a net heat gain by the ocean. Fluxes were integrated over the domain shown in Fig. 1.4c,d from 1 August 2004-31 December 2004.

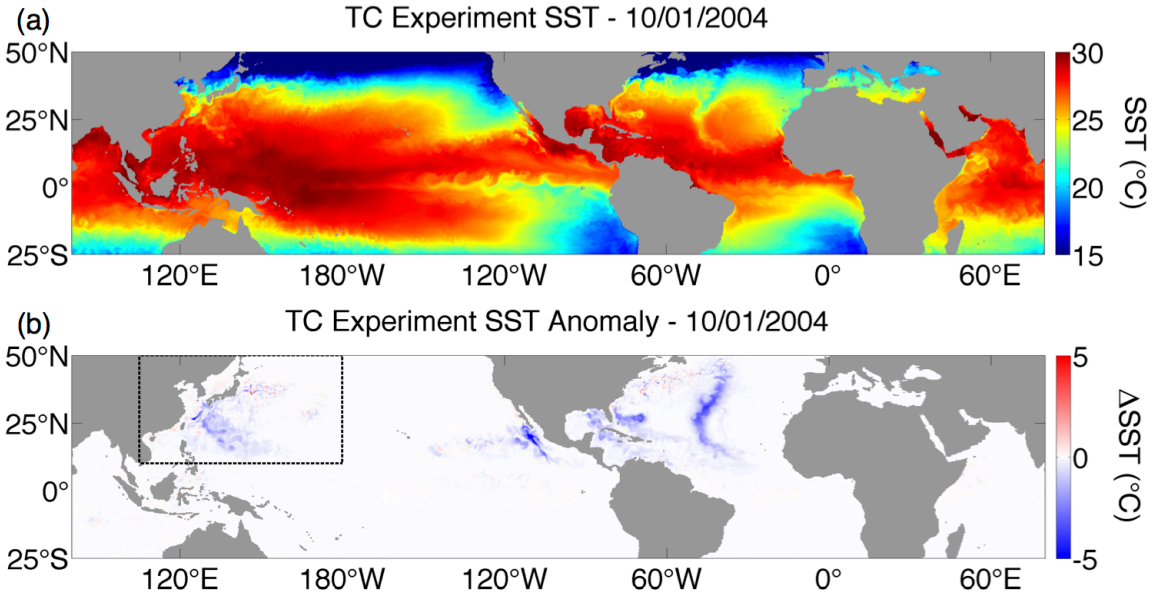


Figure 1.12. Global SST (a) and anomaly (b) fields, demonstrating recent and recovering TC cold wakes in the North Atlantic, West Pacific, and East Pacific on 1 October 2004. The dashed box in panel (b) is the area over which the control volume budget in Fig. 1.17 is calculated.

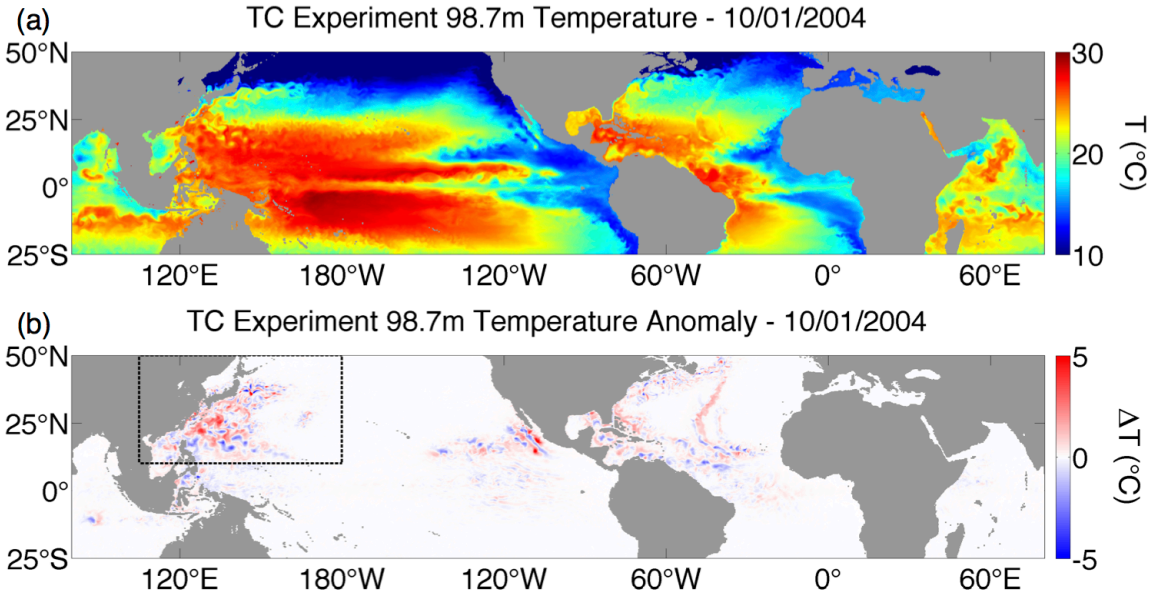


Figure 1.13. Global temperature (a) and anomaly (b) fields at the 98.7m depth level on 1 October 2004, demonstrating the mixing induced warming at depth, as well as warming and cooling from dynamical effects. The dashed box in panel (b) is the area over which the control volume budget in Fig. 1.17 is calculated.

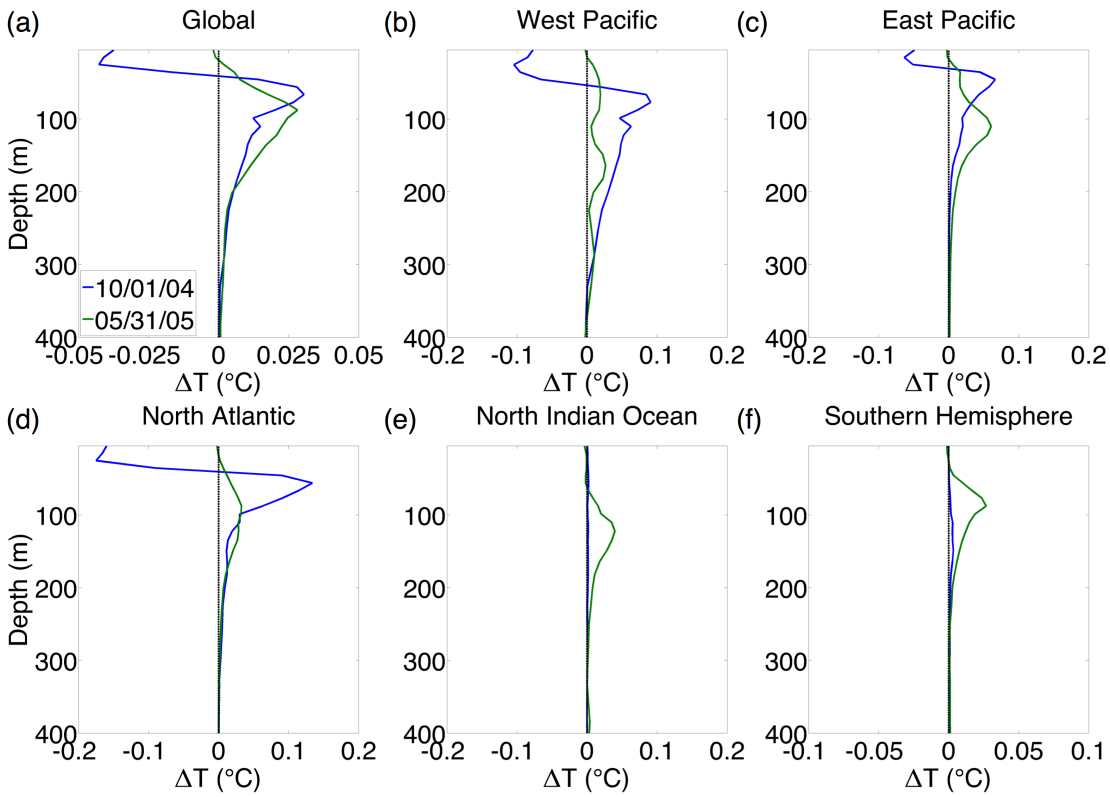


Figure 1.14. Global and basin averaged temperature anomaly profiles at peak of northern TC activity (1 October 2004) and on 31 May 2005. Temperature axes differ between the global (a), basin (b,c,d,e), and hemisphere (f) profiles in order to account for the differences in averaging area (Table 1.3).

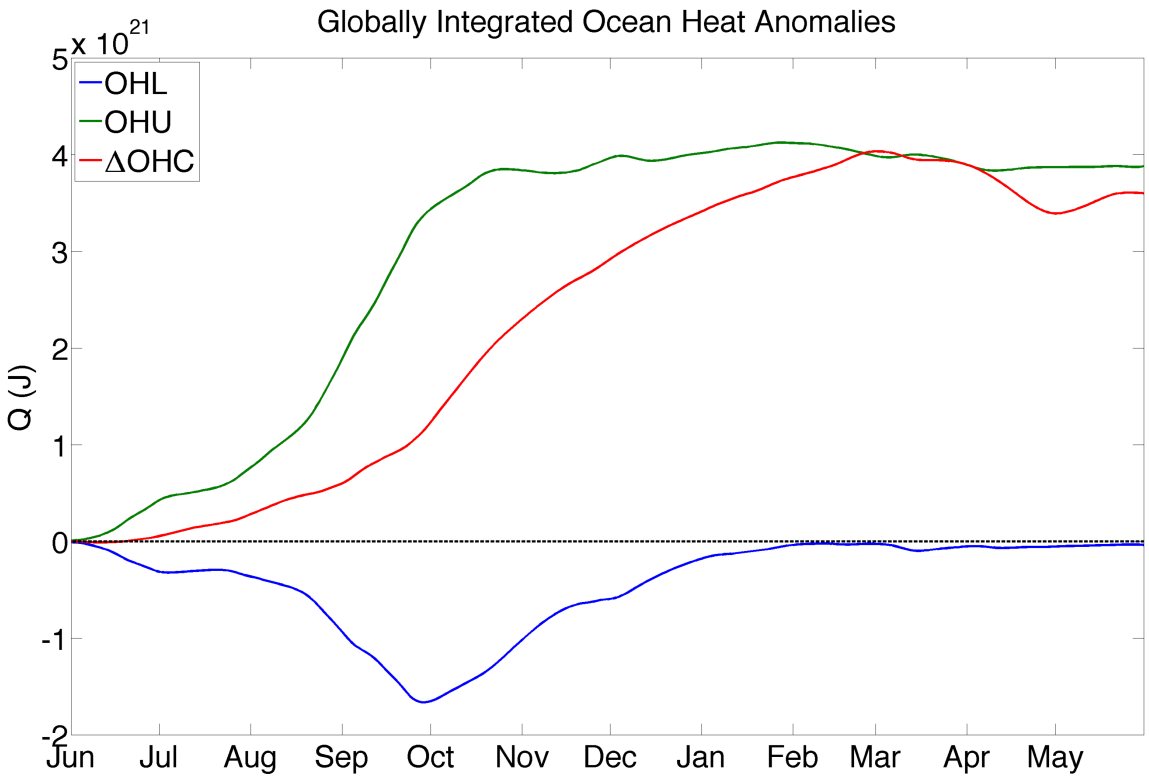


Figure 1.15. Time series of the globally integrated OHL, OHU, and $\Delta OHC$ from 1 June 2004-31 May 2005.

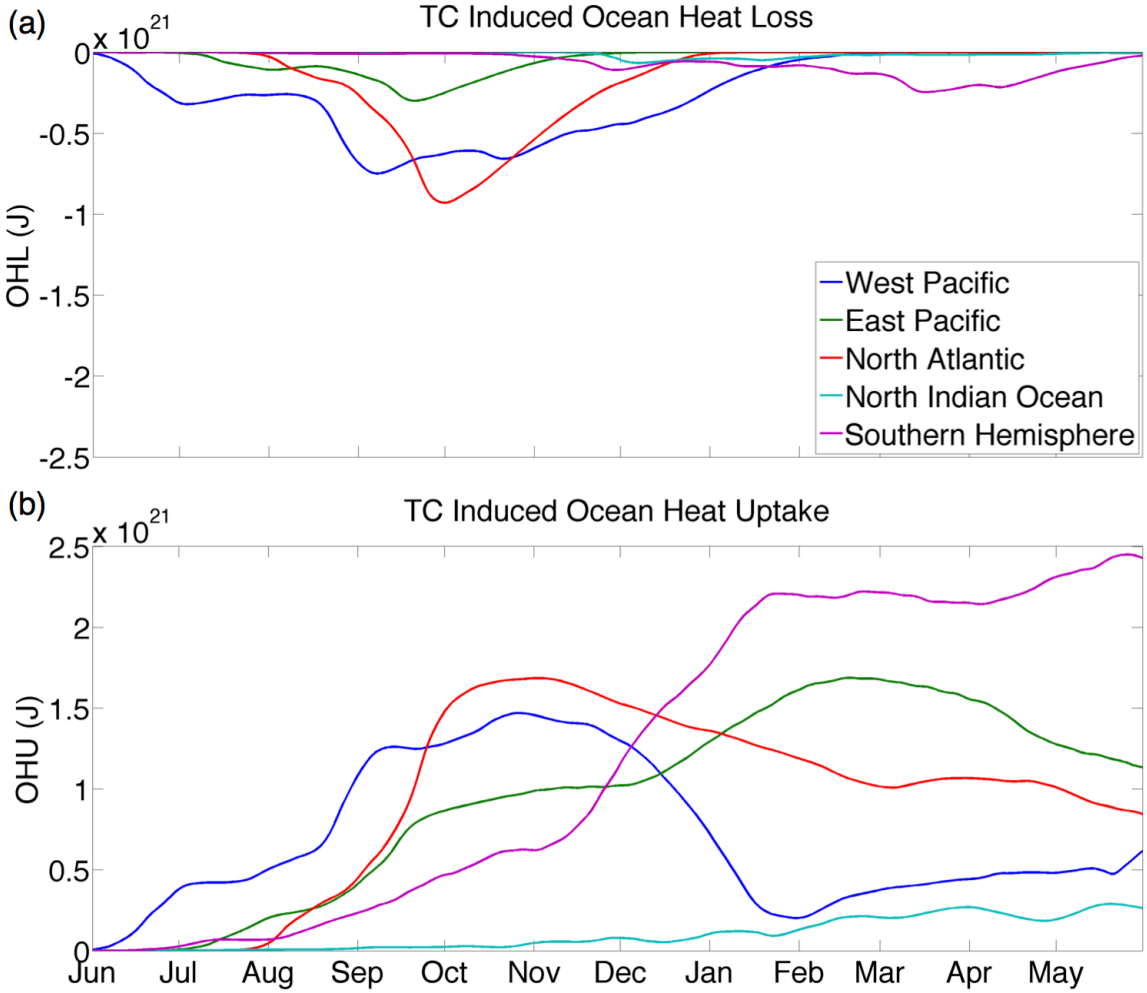


Figure 1.16. Time series of OHL (a) and OHU (b) integrated over the individual ocean basins defined in Table 1.3 from 1 June 2004-31 May 2005.

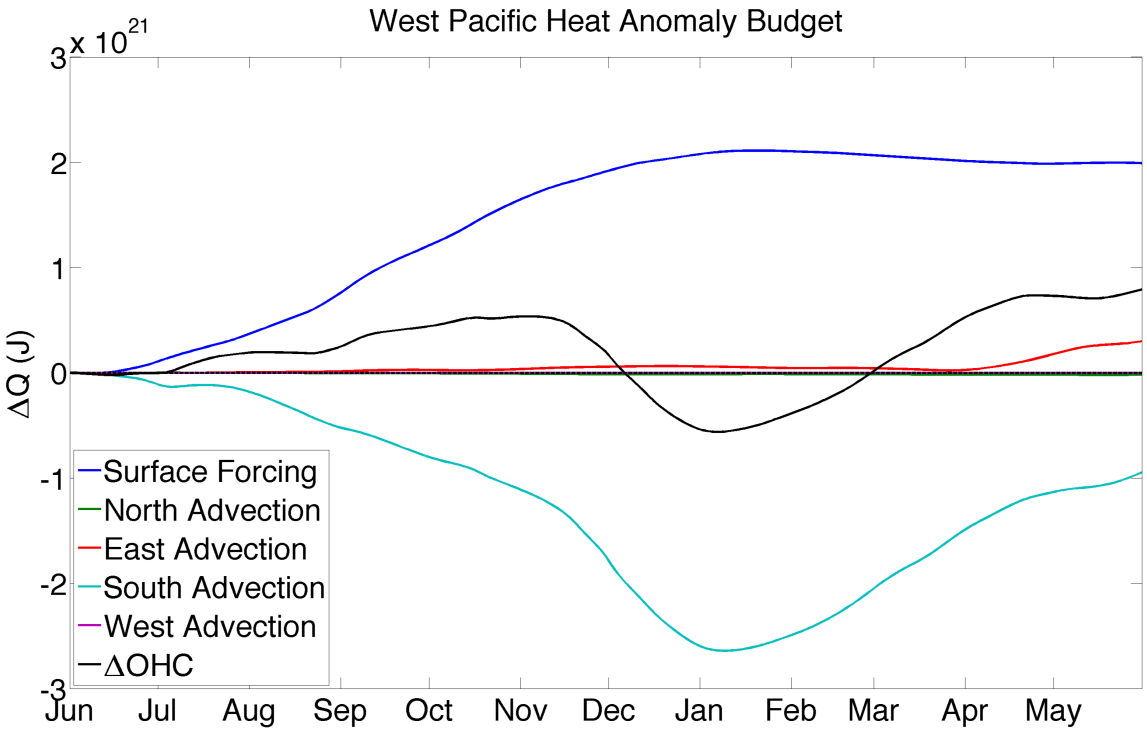


Figure 1.17. Time series of the accumulated heat flux anomalies in the West Pacific TC forcing region, calculated for the domain outlined in Fig. 1.12b and 1.13b from 1 June 2004-31 May 2005. Positive values indicate an increase of heat within the control volume.

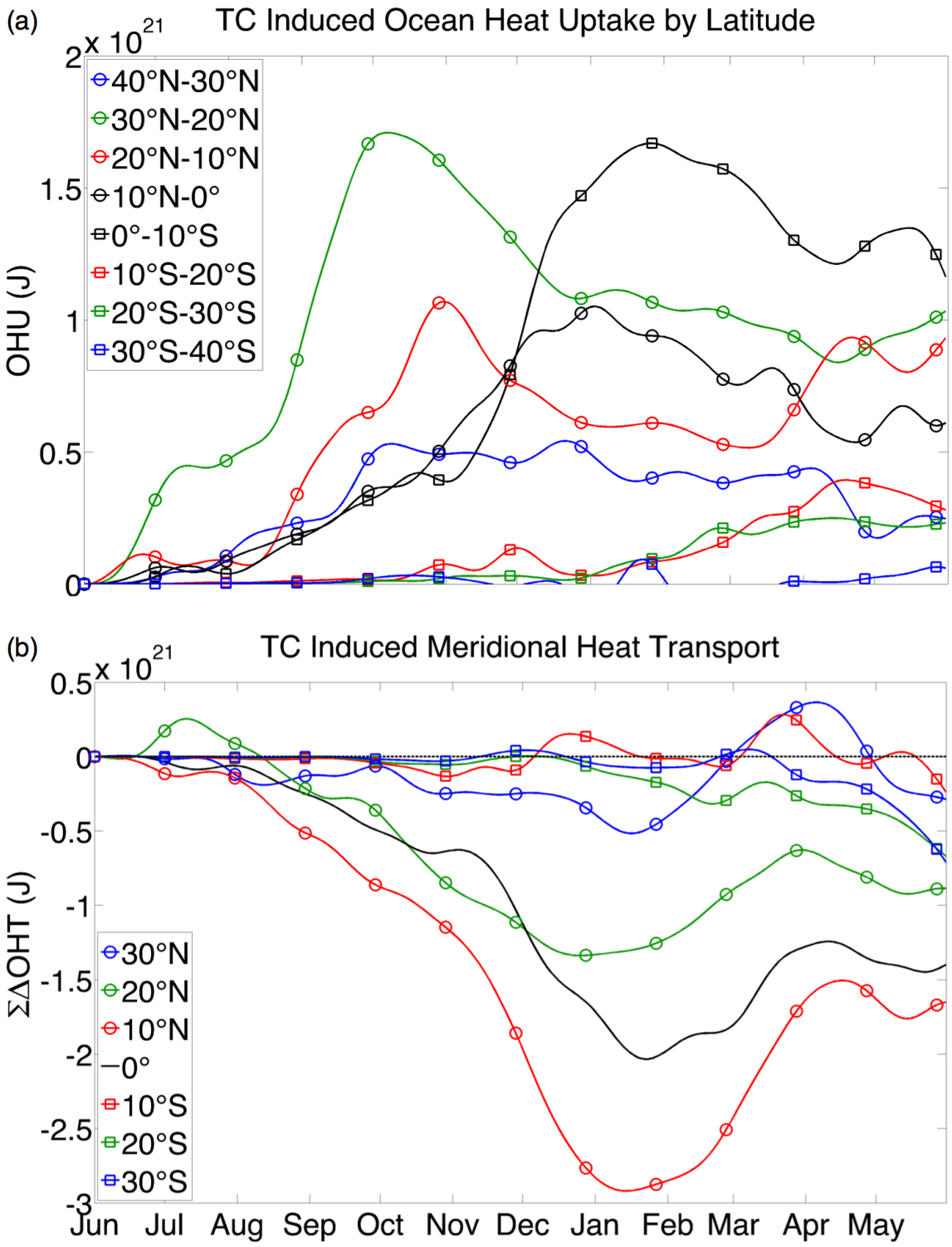


Figure 1.18. Ocean heat uptake integrated by latitude (a) and accumulated meridional heat transport anomaly (Eq. 1.5a) across the boundaries of those bands (b) from 1 June 2004-31 May 2005.Negative values in (b) indicate southward transport.

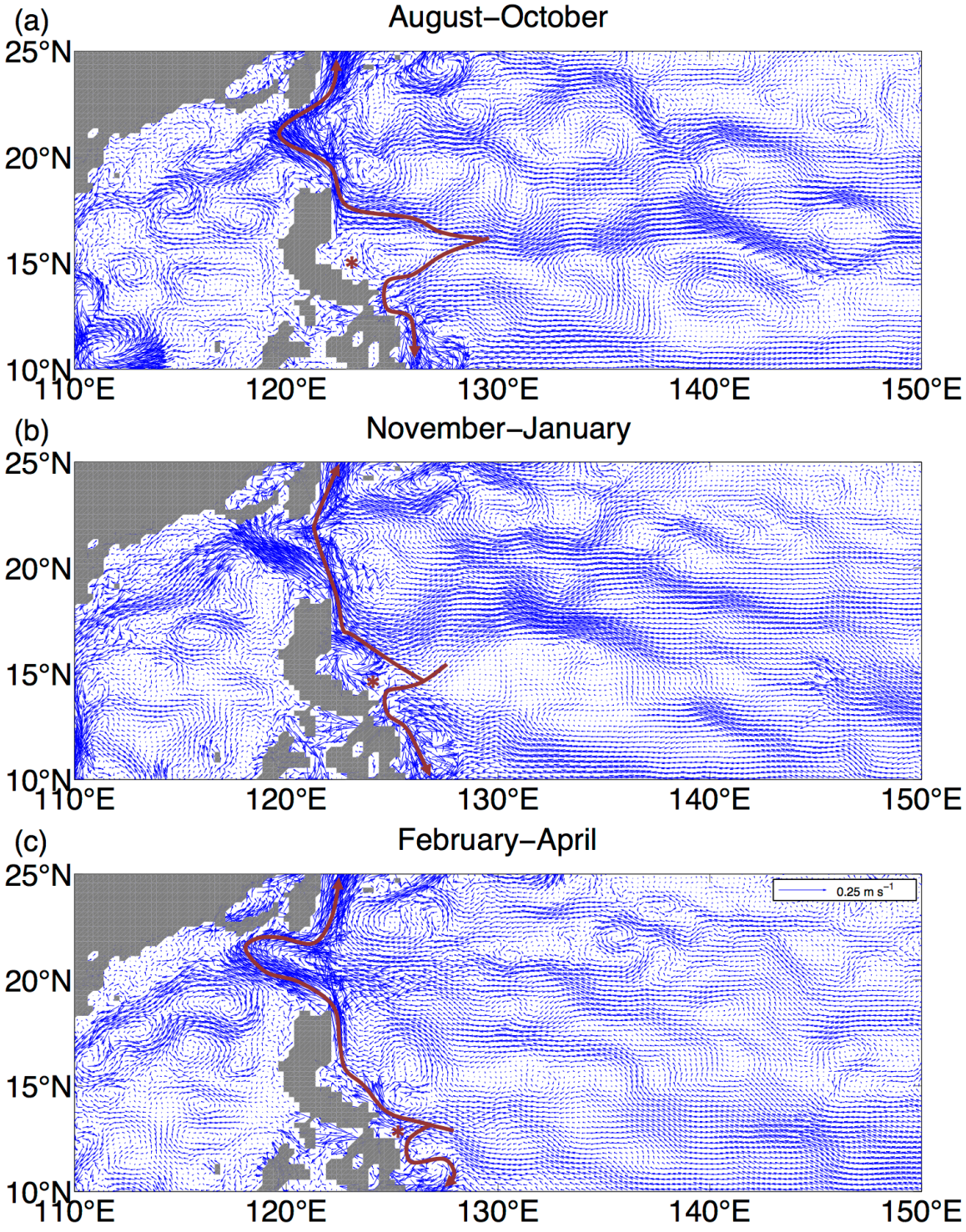


Figure 1.19. Thermocline averaged currents in the West Pacific averaged during the period of peak TC forcing (a), greatest southward advection (b), and reversal(c). Red stars approximate the bifurcation of the North Equatorial Current into the Kuroshio and Mindanao Currents. Red lines are a schematic representation of water parcel trajectories into the Kuroshio Current to the north and the Mindanao Current to the South.

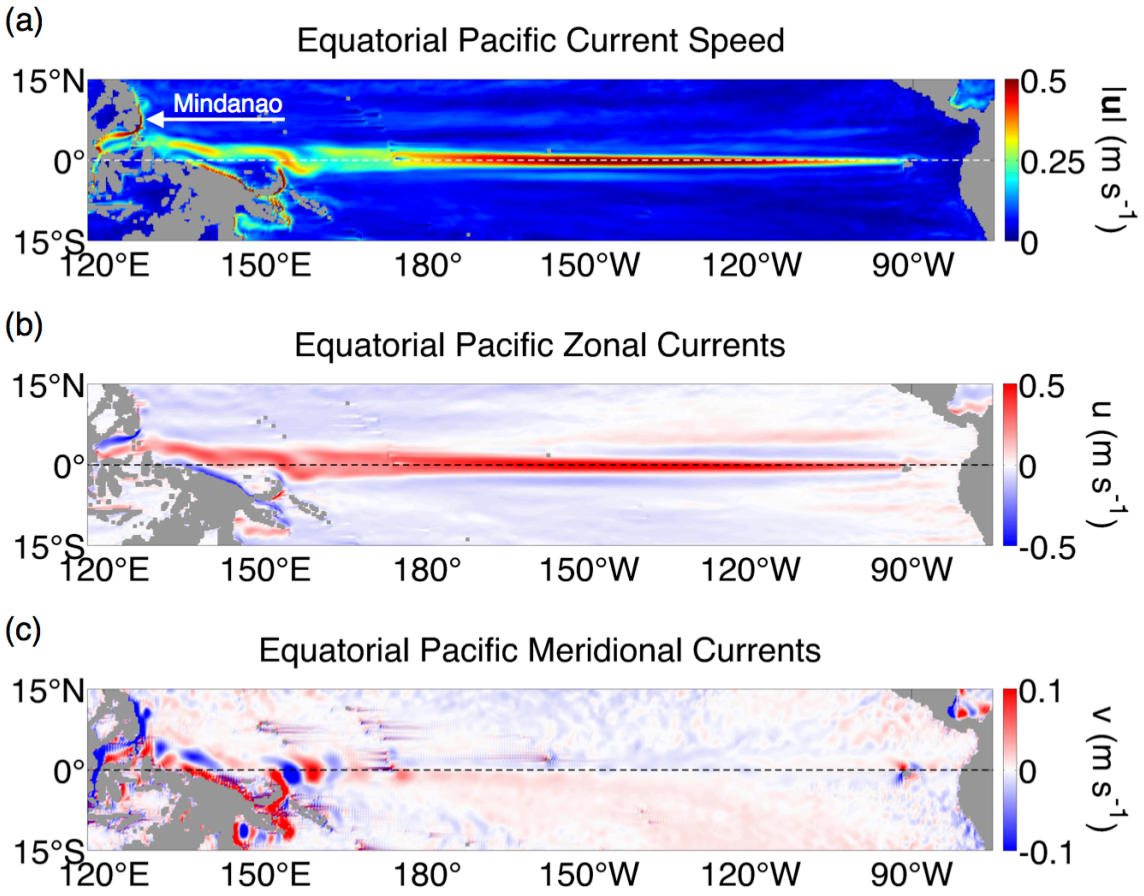


Figure 1.20. Currents in the equatorial Pacific, averaged from 1 June 2004-31 May 2005 and over the 56m-330m depth levels. Presented as current speed (a), zonal currents (b), and meridional currents (c). The scale of meridional currents is reduced due to the greater strength of zonal flow in the tropics.

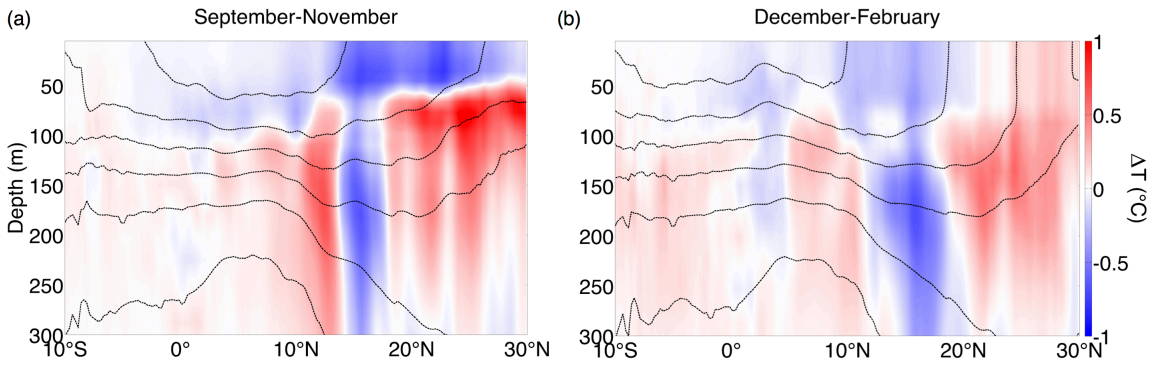


Figure 1.21. West Pacific temperature anomalies averaged over the region of southward advection ($120°E$-$150°E$), with average isopycnals from the same period superimposed, for (a) September, October, November and (b) December, January, February. Isopycnals based on potential density referenced to the surface are averaged over the same region and period as temperature anomalies, and range from $1030 - 1035\ kg\ m^{-3}$ in $1\ kg\ m^{-3}$ increments.

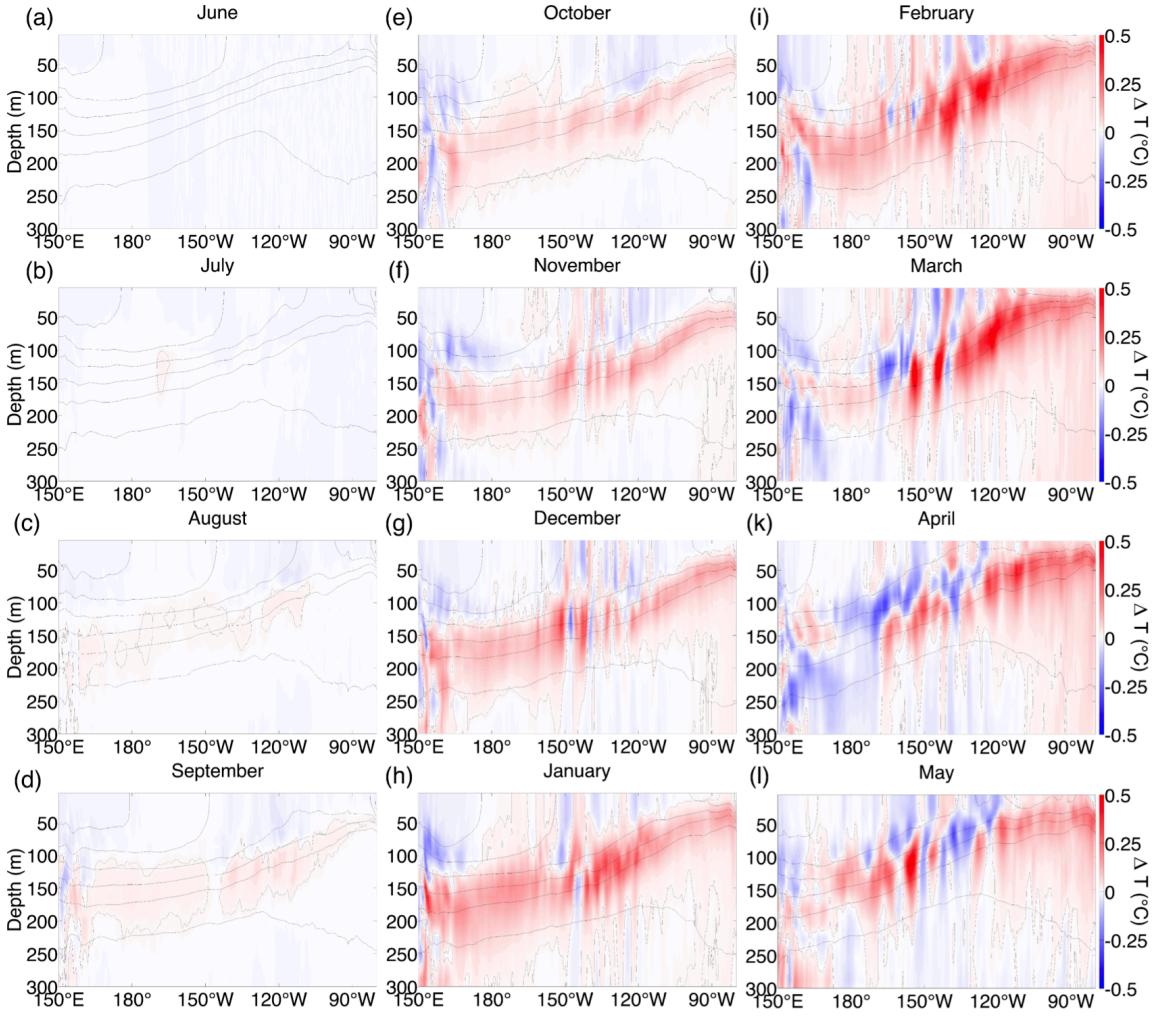


Figure 1.22. Monthly averaged temperature anomalies averaged from $5°S$-$5°N$ in the Pacific Equatorial Undercurrent, with average isopycnals from the same period superimposed. Isopycnals based on potential density referenced to the surface are averaged over the same region and period as temperature anomalies, and range from $1030 - 1035\ kg\ m^{-3}$ in $1\ kg\ m^{-3}$ increments.

# MANUSCRIPT 2

## Interannual Variability of Tropical Cyclone-Induced Thermocline Warming and its Regional Interactions

Michael R. Bueti*, Isaac Ginis, Lewis M. Rothstein

*Graduate School of Oceanography, The University of Rhode Island, Narragansett, Rhode Island*

Stephen M. Griffies

*National Oceanographic and Atmospheric Administration/Geophysical Fluid Dynamics Laboratory, Princeton, New Jersey*

**In preparation for submission to Journal of Climate**

---

* *Corresponding author address:*

Michael R. Bueti,

Graduate School of Oceanography

The University of Rhode Island,

215 South Ferry Road,

Narragansett, RI 02882

Email: mbueti@my.uri.edu

## 2.1 Introduction

The intense and highly coherent winds present in tropical cyclones (TCs) induce strong vertical oceanic mixing over the course of their lifetime. Cyclonic TCs winds can reach magnitudes exceeding 70 $m\ s^{-1}$ at a distance on the order of 50 $km$ from the storm center before gradually decaying. Vertical mixing of mixed layer and upper thermocline waters, anomalous surface buoyancy fluxes, and wind stress curl induced upwelling result in sea surface temperature (SST) cooling, producing the characteristic TC cold wake (Price, 1981). SST cooling is restored within 30-40 days (Dare and McBride, 2011) by anomalous surface heat fluxes within the cold wake (Price et al., 2008). Shallow mixed layer (ML) cooling is restored over similar timescales, although full restoration of the climatological mixed layer can take several months (Park et al., 2011; Price et al., 2008).

Offsetting subsurface warm anomalies are not subject to the same restoration processes as the mixed layer cold anomaly, and decay over much longer timescales (Pasquero and Emanuel, 2008). Emanuel (2001) estimated that the restoration of an idealized cold wake could result in an anomalous increase in ocean heat content (OHC) of up to $5{\cdot}10^{21}\ J$. Analysis of an idealized modeling study of one year of TC activity produced an annual mean OHU rate of $1.4 \pm 0.7\ PW$. Sriver and Huber (2007) derived a mean annual rate of TC induced OHC increase of 0.26 $PW$ from satellite SST and OCCA ocean reanalysis. This value was later revised to a peak value of 0.6 $PW$ and accompanying 60% increase in ocean heat transport (OHT) based on refined estimates of ML deepening (Sriver et al., 2008). Using SST and SSH satellite observations, ML depth and stratification from ocean reanalysis, Jansen et al. (2010) estimated a mean annual seasonal thermocline heating rate of 0.58 $PW$, which may produce a comparable OHU.

Jansen et al. (2010) hypothesized that prior idealized studies contained a sys-

tematic overestimation of persistent TC OHC increases on interannual timescales. They proposed a mechanism whereby upper-thermocline warm anomalies in the mid-latitudes are entrained into the winter ML and reventilated to the atmosphere via enhanced outgoing surface heat flux anomalies. Accounting for this heat release results in a mean annual OHC rate of increase of 0.15 $PW$, a 75% reduction of their previous estimate. Winter reventilation is enhanced by the shoaling of upper-thermocline warm anomalies by baroclinic ML instabilities, a process unaccounted for in most observational estimates (Jansen et al., 2010; Boccaletti et al., 2007). Equatorial upwelling has also been found to play a key role in the release of TC-induced OHC anomalies to the atmosphere Pasquero and Emanuel (2008); Bueti et al. (2014), with low latitude advection providing rapid pathways by which warm anomalies reach the tropical Pacific.

Numerical modeling studies with varying levels of dynamical and thermodynamical idealization have also been used to study the magnitude and mechanisms of TC OHU. Use of enhanced specified mixing to 75 $m$, equivalent to a 25 $m$ deepening of the ML, by Pasquero and Emanuel (2008) in a 4° horizontal resolution ocean general circulation model (OGCM) produced an additional $1.1{\cdot}10^{22}$ $J$ of OHC over 12 months of model integration, with ∼50% of this heating persisting through the winter. Anomalies produced by a similar imposed mixing to 155 $m$ had ∼80% retention. Sriver and Huber (2010) specified realistic TC wind forcing derived from QuikScat data in a 3.6° zonal by 1.5° meridional resolution OGCM. By doubling and tripling the TC winds, mean OHU rates varied from 0.1 $PW$ to 0.3 and 0.8 $PW$ respectively, during 500 years of model integration. Anomalous heat transport was predominantly into the tropics, warming the upper 300 $m$ of the tropical Pacific, with much of the heat deposited in the Equatorial Undercurrent (EUC).

A coupled ocean-atmosphere general circulation modeling study conducted by

Scoccimarro et al. (2011), with a 2° resolution ocean, found a 35% increase in equatorward OHT between 0° and 18°$N$ ($\sim$0.5 $PW$), a 5% increase in poleward OHT between 18°$N$ and 40°$N$ ($\sim$0.1 $PW$) attributed to the presence of TCs during their 120 year experiment. The 3/4° resolution atmospheric component simulated a realistic climatology of spatial TC distribution and movement, but underestimated both the frequency and magnitude of storms. Jullien et al. (2012) conducted finer (1/3°) resolution regional study in the South Pacific using surface forcing from global Weather Research and Forecasting (WRF) model output with and without TCs, from which a regional rate of increase in OHC of $\sim$0.015 $PW$ during the southern TC season was derived, significantly smaller than the global mean OHT.

Vincent et al. (2013) carried out a similar experiment to that presented here and in Bueti et al. (2014), using a 1/2° OGCM initialized from World Ocean Atlas climatology and forced with winds from version 2.0 of the Coordinated Ocean-Ice Reference Experiments (CORE-II) and synthetic vortices based on the IBTrACS record and Willoughby et al. (2006) wind profile formulation to explore the impact of TCs on the mean ocean state. This methodology produced a subsurface temperature anomaly centered around $\sim$75 $m$ due predominantly to vertical mixing. A globally averaged meridional heat transport (MHT) anomaly was inferred from an assumed ocean adjustment to incoming heat anomalies, with anomalous heat moving on average from latitudes of net input to those of heat release, displaying a transport from the subtropics poleward to the mid-latitudes, and equatorward to the deep tropics, equatorward of 5°. As in Scoccimarro et al. (2011), the magnitude of the MHT anomaly was several orders of magnitude smaller than the mean MHT found in their model and derived from in-situ measurements by Wunsch (2005). Due to the apparently small contribution of TC-induced OHC anomalies on the globally averaged MHT, Vincent et al. (2013) concluded that the dominant long-term influence of TCs on the ocean

was a $5-15\%$ reduction in the amplitude of the SST seasonal cycle in the TC basins.

However, a more regionally focused analysis of TC-induced MHT and OHC anomalies may be justified. As discussed in Bueti et al. (2014), there are significant differences in the accumulation of TC warming and the pathways by which it is redistributed between ocean basins, and notable temporal variability in the strength and meridional direction of those pathways. Complementing these differences in the TC anomaly, Jayne and Marotzke (2001) outline the significant inter-basin and interseasonal variability in the total MHT, further supporting the idea that a globally averaged picture of the meridional circulation may be insufficient to properly describe the large-scale impact and redistribution of TC heating on the ocean.

Interaction of TC-induced OHC anomalies with large-scale climate variability is a further area of inquiry. Fedorov et al. (2010) described a process by which TC warming of the equatorial East Pacific sustain El Niño-like conditions in past climates via the positive feedback of the Bjerknes mechanism. In light of the preferential redistribution of TC warm anomalies into the tropical East Pacific thermocline (Bueti et al., 2014), a modulation of the El Niño-Southern Oscillation (ENSO) may present itself in interannual model simulations. Conversely, the strong influence of ENSO on tropical Pacific upwelling (Wang, 2001) presents a potential mechanism for interannual accumulation and ventilation of OHC anomalies in the tropical Pacific.

We expand on the work presented in Bueti et al. (2014) by carrying out a similar global ocean-ice general circulation experiment over the 20-year period from 1985 through 2004 using a semi-idealized distribution of realistic TC surface boundary conditions. In this way, we hope to better understand the magnitude of TC-induced changes in OHC over interannual timescales, focusing on the regional impacts and interaction with large-scale ocean climate processes. Specifically, we will enumerate the amount of anomalous OHC attributable to TC forcing, the regional mechanisms

by which the ocean remains in quasi-equilibrium, the dynamics driving the interannual variability of TC-induced OHC, and explore any regional bias in accumulation of anomalous warming.

## 2.2 Methods

### 2.2.1 The Ocean Model

We use GFDL's Modular Ocean Model (MOM), version 4 (Griffies, 2009). MOM is a hydrostatic primitive equation ocean model configured using a Boussinesq approximation with a free surface algorithm and coupled to the SIS (Sea Ice Simulator) ice model to handle processes in the high latitudes. We utilize an ocean-ice configuration with its resolution taken from the CM2.5 coupled climate model documented in Delworth et al. (2012). The horizontal resolution varies from 28 $km$ at the equator to $8-11$ $km$ at high latitudes. The model has 50 vertical levels, 23 of which are in the upper 500 $m$ of the ocean. The upper ocean mixing and restratification is of particular importance in evaluating the ocean's response to TCs. Vertical mixing of tracers and momentum is handled by the KPP boundary layer scheme (Large et al., 1994) , which computes enhanced mixing within a boundary layer depth determined according to a bulk Richardson number. Mixing of tracers also arises in regions of negative surface buoyancy fluxes from a non-local transport term proportional to surface boundary heat and salt fluxes. Beneath the boundary layer, tracer mixing arises due to parameterized shear instability, tide-induced mixing, double diffusion, and convection due to gravitational instabilities. The parameterized mixing is thus highly variable in both space and time, producing mixing that is strongly dependent on the applied surface forcing. MOM parameterizes the effect of sub-mesoscale mixed layer eddies according to Fox-Kemper et al. (2011), with these eddies enhancing the ventilation of TC warm anomalies (Jansen et al., 2010).

### 2.2.2 Air-sea fluxes and TC forcing

As in Bueti et al. (2014), the ocean model is forced with air-sea boundary conditions as in the CORE-II experiments described by Griffies et al. (2009) and Danabasoglu et al. (2014). The prescribed atmospheric state is from the Corrected Inter-Annual Forcing product (Large and Yeager, 2009) with a 1.9° resolution, providing sea level pressure, air temperature, specific humidity, zonal and meridional winds at 10 $m$, every six hours; daily average values for incoming shortwave and longwave radiation; and monthly averages of liquid and frozen precipitation rates.

The CORE-II winds are relatively coarse, so that TC winds are poorly resolved, if present at all. Strong winds in the compact TC eye-wall region, critical for producing ocean mixing, are entirely absent. In this study we introduce two changes to the CORE-II boundary conditions. First, the parameterization of the drag coefficient, $C_D$, is modified for strong winds. The linear relationship between wind speed and $C_D$ (Large and Yeager, 2004) used in CORE-II greatly overestimates the wind stress for high wind speeds, particularly those present in tropical cyclones (Powell et al., 2003; Moon et al., 2007). The high $C_D$ values result in unrealistically intense vertical mixing (Sanford et al., 2007). For wind speeds greater than 12.5 $m\ s^{-1}$, we replace the Large and Yeager (2004) parameterization with the formulation of Moon et al. (2007), empirically derived from coupled wave-wind model simulations in hurricanes. The hybrid drag coefficient increases more slowly than in Large and Yeager (2004) and levels off for wind speeds greater than 40 $m\ s^{-1}$.

Second, we modify the CORE-II winds by introducing synthetic TCs based on the National Hurricane Center (NHC) and Joint Typhoon Warning Center (JTWC) Tropical Cyclone Vitals Database (TCVitals). This database contains cyclone location, intensity, and structure information, generated in real time by forecasters. TCVitals are used to initialize cyclones in operational forecasting models. We use

TCVitals because they contain parameters such as radius of maximum wind, radius of last closed isobar, and the radii at which winds reach values of 18 $m\ s^{-1}$ and 26 $m\ s^{-1}$ in the northeast, southeast, southwest, and northwest quadrants of the storm (extended structure data), which are not consistently available for all basins from IBTrACS (International Best Track Archive for Climate Stewardship) or NHC's North Atlantic hurricane database (HURDAT2). While there are statistical biases in storm intensity (weakening of $\sim 0.25-1\ m\ s^{-1}$) and location ($0-5\ km$) compared to the best track database (Trahan and Sparling, 2012), these errors should have negligible impact on the results of this study.

Air-sea heat fluxes are calculated from bulk formulae as described in Griffies et al. (2009). No explicit SST restoration is applied. Surface heat fluxes are allowed to freely evolve under the specified atmospheric state and respond to both the enhanced TC winds and cooled SSTs in the storm cold wakes.

Synthetic TC wind speeds are generated for each storm in the TCVitals as is done for operational hurricane forecasting (Bender et al., 2007). The cyclone wind field is projected onto the ocean model grid, and at any location where the CORE-II wind speed is lower than the TC wind speed it is replaced by the latter. For cases when the extended structure data is unavailable, the axisymmetric wind profile of Holland (1980) is used. The Holland (1980) axisymmetric profile comprises only $\sim$20% of storm hours, typically during cyclogenesis and storm dissipation. Further details of the wind formulation and the blending method as well as more detailed treatment of the air-sea fluxes can be found in Bueti et al. (2014).

### 2.2.3 Experiment procedure

The model is run from 1 January 1985 through 31 December 2004 in two forcing configurations. The first has surface forcing based on the CORE-II atmospheric state, and we will refer to this experiment as the "control experiment". The other

configuration has the CORE-II surface wind augmented by embedding the synthetic TCs, and will be referred to as the "TC experiment". An "anomaly" is defined as the difference between the oceans in the TC and control experiments, thus yielding the net thermal and dynamical effect of TC activity.

TCs from the actual simulation dates are not used. Rather, we repeat the same TC forcing five times over the 20 year period and base that forcing on the TCs that actually occurred over a 5 year period. We select the 5 year period, 1 January 2004 through 31 December 2008, as being representative of TC interannual variability and spatial distribution (Fig. 2.1). Using this semi-idealized framework, we hope to untangle the influence of internal ocean variability and large-scale climate oscillations such as ENSO and the North Atlantic Oscillation (NAO) on TC induced heating from the signature of implicit variability of the TC forcing. The use of a 5-year repeating TC cycle imposed a 5-year signature to the forcing and ocean that was accounted for in analysis of processes taking place over shorter and longer timescales. The model's specific ability to reproduce ENSO variability will be discussed in Section 2.3.7.

Ocean initial conditions are derived from GFDL's Ocean Data Assimilation Experiment (ODAE) product, described by Zhang et al. (2007). This product provides the average monthly temperature and salinity fields at 1° grid spacing. MOM is started on 1 January 1984 from the ODAE January 1984 field interpolated onto the ocean model grid, with air-sea fluxes computed based on the CORE-II atmospheric state. The model is run for one year. At this point, the ocean has reached a mechanical quasi-steady state.

## 2.3 Results

### 2.3.1 SST and air-sea heat flux anomalies

Shown in Fig. 2.2 is the SST anomaly ($\Delta SST$) averaged in 3-month windows over the 20 year simulation: prior to the northern TC season (February-April, Fig.

2.2a), early in the TC season (May-July, Fig. 2.2b), at the peak of the TC season (August-October, Fig 2.2c), and following the TC season (November-January, Fig. 2.2d). These averaging windows are shifted by 1 month in relation to those used in Vincent et al. (2013) in order to more completely capture the seasonality of the TCs used here. $\Delta SST$ in May-July exhibits weak cooling ($\sim 0.5°C$) in the regions of high TC activity (North Atlantic, West Pacific, East Pacific) illustrated in Fig. 1.2, with weak warming poleward of the cooling (Fig. 2.2b). Cooling is strongest during the peak northern TC season, exceeding $1°C$ in the West Pacific, East Pacific, and Gulf of Mexico, with little surface warming evident (Fig. 2.2c). Little mid-latitude cooling remains by the onset of winter, while warming poleward of $20°N$ and $20°S$ has become evident (Fig. 2.2). The magnitude and extent of late winter warming (Fig. 2.2a) is shifted poleward of the winter warming found by Vincent et al. (2013). Surface cooling greater than $0.5°C$ is found between $15°S$ and $30°S$ during the boreal winter due to the impact of southern hemisphere TCs.

Numerous eddies are present in the Southern Ocean, with differences in their location between the TC and control experiments exhibited as offsetting warm and cold SST anomalies. This pattern is not expected to contribute to net changes in ocean heat or transport, and will not be explored further.

Negative summer $\Delta SST$ is associated with accumulated cooling in TC cold wakes. Higher latitude winter warming indicates entrainment of upper-thermocline warm anomalies into the winter mixed layer and subsequent ventilation as discussed in Jansen et al. (2010) and Vincent et al. (2013). Warming is present in the tropical Pacific east of 180° throughout the year, a result of TC-induced warm anomaly advection by low latitude western boundary current and equatorial undercurrent (EUC) pathways described in Bueti et al. (2014). Warm anomalies shoal along the tropical thermocline and are brought to the surface as part of the equatorial Pacific upwelling

(Wyrtki, 1981), producing anomalously warm SSTs in the equatorial cold tongue.

Fig. 2.3 shows the incoming surface heat flux anomaly ($\Delta F$) averaged over the 20-year simulation. F is the sum of the shortwave, longwave, sensible, and latent heat fluxes at the ocean surface. Regions of positive (negative) $\Delta F$ correspond with those of negative (positive) $\Delta SST$. Negative $\Delta F$ indicates ventilation of TC-induced warm anomalies to the atmosphere. In the mid-latitudes, this ventilation is a result of the winter deepening of the mixed layer in response to strong momentum and negative buoyancy fluxes at the ocean surface. Warm anomalies are entrained into the winter mixed layer and ventilated to the atmosphere via anomalous outgoing surface heat fluxes (Jansen et al., 2010). In the tropics thermocline waters are upwelled towards the surface, with anomalous heat fluxes again ventilating warm anomalies to the atmosphere.

Negative flux anomalies are somewhat weaker and display less meridional extent than those shown in Fig. 13c of Vincent et al. (2013), often reflecting the mesoscale structure of the western boundary currents due to meandering of the ocean fronts. Positive $\Delta F$ tends to be stronger and broader than in Vincent et al. (2013), a reflection of the differences in air-sea flux parameterizations, TC wind intensity and structure representation due to finer model resolution, and biases in the TC distribution due to repeated use of 2004-2008 storm tracks.

$\Delta F$ is greatest in the West Pacific east of Taiwan, exceeded 15 $W\ m^{-2}$ and reaching values greater than 20 $W\ m^{-2}$ at the core of TC activity. These values exceed the incoming fluxes seen in Vincent et al. (2013) by $\sim$20%. These differences may be due to differences in the TC forcing and horizontal model resolution. Heat flux anomalies in other regions are generally smaller, $\sim$10 $W\ m^{-2}$ in the East Pacific and Gulf of Mexico, and $\sim$6 $W\ m^{-2}$ in the Southern Hemisphere. Average incoming $\Delta F$ was compared to representative locations in the North Atlantic ($50°W$, $30°N$)

and Pacific (180°, 30°$N$). Incoming $\Delta F$ represents an enhancement of summer heat uptake of 7% in the North Atlantic, 5% in the East Pacific, and 11% in the West Pacific. Average outgoing $\Delta F$ values represent increased heat loss compared to peak winter conditions of 15% in the North Atlantic, 3% in the East Pacific, and 8% in the West Pacific. The greatest TC heat input relative to background conditions is in the subtropical West Pacific, while the North Atlantic has the greatest release of heat to the atmosphere relative to typical heat flux values. The outgoing $\Delta F$ of $\sim$10 $W\ m^{-2}$ in the tropical Pacific cold tongue equates to a nearly 10% reduction in typical incoming heat flux values of $\sim$100 $W\ m^{-2}$ there.

Regionally, $\Delta F$ can exceed 20 $W\ m^{-2}$ near Gulf Stream and Kuroshio. The positive and negative $\Delta F$ along these strong fronts are associated with phase shifting meanders of these boundary currents between the TC and control experiments. The equatorial Pacific exhibited $\sim$6 $W\ m^{-2}$ of outgoing $\Delta F$.

### 2.3.2 Global subsurface temperature and ocean heat content anomalies

The globally averaged temperature anomaly ($\Delta T$) as a function depth is shown in Fig. 2.4b to illustrate the vertical ocean response to TC wind forcing. It is instructive to compare the global temperature anomalies to global TC forcing, represented by TC power dissipation (Fig. 2.4a) adapted from Emanuel (1999) as

$$PD\,(t) = \iint dAC_D\Delta U_{10}^3\,(x, y, t) \tag{2.1}$$

where integration in x and y is carried out across the area ($A$) of the region in question, $C_D$ is the surface drag coefficient, and $\Delta U_{10}$ is the magnitude of the 10 $m$ wind speed.

Distinct upper layer cooling, extending to $\sim$40 $m$, is present during periods of high PD. Warm anomalies are generated below the cooling that deepen and spread through the water column with time. Warming reaches its maximum between 125 $m$ and 150 $m$, but extends as deep as 500 $m$. The seasonal peak attenuates during austral

summers as warm anomalies in the northern hemisphere are ventilated between TC seasons. The imposed 5-year TC forcing cycle is present in the annual cooling and warming events, but inter-annual variability of different periods is noticeable. The temporal and vertical structure of analogous years within each repeat (e.g. 1993, 1998, and 2003) is markedly different, reflecting the significance of internal ocean variability in the ocean response to TC forcing.

The ocean heat content anomaly ($\Delta OHC$) between the TC and control experiments is calculated as

$$\Delta OHC\,(t) = c_p \rho_o \iint dA \int_h^{0\ m} dz \Delta T\,(x, y, z, t) \tag{2.2}$$

where $c_p$ is the heat capacity of seawater ($\sim 4,000\ J\ kg^{-1}\ K^{-1}$), $\rho_o$ is the Boussinesq reference density, and h is either the full ocean depth or the 739 $m$ depth level. 739 $m$ is chosen as it is the closest model level to the 700 $m$ depth used in upper ocean in situ analyses, such as Levitus et al. (2012b), allowing consistent comparison with observations.

Area integrated $\Delta OHC$ is analyzed first, shown in Fig. 2.5j. An area averaged $\Delta OHC$ is also calculated, which is defined as Eq. 2.2 normalized by the integration area, shown in Fig. 2.6. A three-month smoothing is applied to integrated and averaged time series in order to highlight variability at greater than seasonal timescales. We begin with analysis of the globally integrated $\Delta OHC$ (Fig. 2.5) and globally averaged $\Delta OHC$ (Fig. 2.6).

$\Delta OHC$ increases steadily during the first 5-6 years. These years are treated as an adjustment period as in Vincent et al. (2013) , during which $\Delta OHC$ has not yet fully traversed the ventilation pathways described later. $\Delta OHC$ generally exhibits oscillatory behavior around $\sim 1.6 \cdot 10^{22}\ J$ with an amplitude $\sim 0.2 \cdot 10^{22}\ J$ on timescales similar to the duration of the repeated TC cycle. This mean value is a vanishingly

small percentage of the total OHC (0.15% of $\sim 1 \cdot 10^{25}\ J$). However, $\Delta OHC$ represents a significant portion of the interannual change in global OHC from Levitus et al. (2012a) ($OHC'_{Lev}$) over the same period (30% of $\sim 5 \cdot 10^{22}\ J$). Seasonal accumulation and ventilation is superimposed on the interannual variability, characterized by warm events of $\sim 1 \cdot 10^{21}\ J$, the amplitude of which were reduced by the applied smoothing. Periods of reduced upper ocean $\Delta OHC$ correspond with an increase in deep versus shallow warming.

The global meridional heat transport is integrated to the ocean bottom

$$MHT\left(y,t\right) = c_p \rho_o \int dx \int_H^{0\ \ m} dz v\left(x,y,z,t\right) \cdot T\left(x,y,z,t\right) \tag{2.3}$$

where H is the ocean depth and $v$ is the magnitude of the meridional currents. MHT is averaged over each of the 5-year TC repeats (Fig. 2.7), and is predominantly poleward in both the northern and southern hemisphere. Poleward transport reached maxima of $\sim 2\ PW$ near $35°N$ and $30°S$. On average the northern hemisphere has a small equatorward heat transport at very low latitudes, indicated by a shifting of the MHT zero crossing north of the equator. Mean MHT is consistent with prior modeling (Trenberth and Caron, 2001) and observational (Wunsch, 2005) estimates, and again the first five years appear to be a transient adjustment period.

In contrast, the meridional heat transport anomaly ($\Delta MHT$) displays poleward transport north of $\sim 25°N$. The negative slope in $\Delta MHT$ about the equator represents a tropical heat convergence, as discussed in Bueti et al. (2014). Latitudes of $\Delta MHT$ convergence (e.g. poleward of $30°N$ and $40°S$, $10°S{-}10°N$) corresponded with those of outgoing heat flux anomalies due to winter ventilation and tropical upwelling (Fig. 2.2a,d, Fig. 2.7a) while heat divergence is present at latitudes of direct TC forcing and $\Delta OHC$ generation (e.g. $10°N - 30°N$, $40°S - 10°S$). While strong mesoscale longitudinal variability is present in regions of winter reventilation, primar-

ily due to differences in the location of Gulf Stream and Kuroshio meanders between the TC and control experiments, on average these regions provide for a significant anomalous outgoing heat flux at the ocean surface.

This structure is consistent with the large-scale balance of incoming to outgoing heat flux anomalies from which Vincent et al. (2013) derived $\Delta MHT$. The latitudinal structure of MHT and $\Delta MHT$ here are consistent with their findings. The peak poleward heat export is shifted towards higher latitudes, from $20°S$ and $25°N$ in Vincent et al. (2013) to $42°S$ and $30°N$ here. The amplitudes of MHT is greater than in their results, indicating a more vigorous mean overturning, as is $\Delta MHT$, suggesting greater $\Delta MHT$ in response to increasing $\Delta OHC$ as heat anomalies are advected more rapidly than in prior studies.

### 2.3.3 Atlantic ocean heat content anomalies

A regional analysis of temperature and OHC anomalies is carried out next, over the domains defined Fig. 2.8 and Table 2.1. The average $\Delta T$ response over the North Atlantic (Fig. 2.9b) is highly seasonal, with direct TC forcing (Fig. 2.9a) temperature anomalies that propogate downward along isopycnals as they are advected within the subtropical gyre. A weak warm anomaly centered around 125 $m$ persists through the simulation. The depth of mixing and subsequent warm anomalies is sensitive to the strength and duration of TC wind forcing and the ocean stratification, as discussed in Ginis (2002).

Strong entrainment of warming into the winter mixed layer and reventilation to the atmosphere, indicated by upward extension of warm anomalies to the ocean surface with time (Fig. 2.9b) and anomalous fluxes of heat through the ocean surface

$$\Delta Q = \iint dA \Delta F\left(x, y, t\right) \tag{2.4}$$

shown in Fig. 2.10, prevent strong accumulation of TC warming in the region. This

reventilation is in line with the seasonal hypothesis of Jansen et al. (2010) which showed that ∼25% of the warming introduced during the TC season remains after winter ventilation. However, upper thermocline $\Delta OHC$ is more persistent here, with 36% of the anomalous heat uptake remaining unventilated by local wintertime effects (Table 2.2). Between 1995 and 1999 $\Delta T$ extent deepens significantly, with an interannually persistent warm anomaly centered at 200 $m$ during this period (Fig. 2.9b).

North Atlantic $\Delta OHC$ (Fig. 2.5a, 2.6a) is steady through the early 1990s, before rising sharply between 1995 and 1996, with a large portion of the anomalous heat accumulating below 739 $m$. $\Delta OHC$ subsequently declines precipitously through the late 1990s and early 2000s, by $2.8 \cdot 10^{21}$ $J$ in the upper ocean and nearly $7 \cdot 10^{21}$ $J$ through the full water column. These values are equivalent to an 11% and 24% decreases in the shallow and deep trends in $OHC'_{Lev}$ over the same period. Following 1999, the ocean below 739 $m$ is cooled relative to the control run.

The abrupt decline in North Atlantic $\Delta OHC$ (Fig. 2.5a, 2.6a) coincides with a shift in poleward $\Delta MHT$ (Fig. 2.11), with regions of mid-latitude convergence and ventilation (Fig. 2.12) of heat moving equatorward. An abrupt shift in the state of the NAO (Barnston and Livezey, 1987) from neutral to negative after a persistent positive period in the late 1980s and early 1990s (Fig. 2.13) induces a change in the regional circulation and subsequently impacts $\Delta OHC$ accumulation and ventilation.

Yeager et al. (2012) showed that this prolonged positive NAO phasing results in a spin-up of the Atlantic meridional overturning circulation in the Community Climate System Model, version 4 (Gent et al., 2011). This spin-up is accompanied by increasing transport poleward from the subtropical gyre (STG;$50°W10°W$, $50°N60°N$) to the subpolar gyre (SPG; $70°W30°W$, $32°N42°N$) which is balanced by enhanced outgoing heat fluxes under the relatively strong winds during this period. The sudden

NAO weakening creates an imbalance between poleward transport and ventilation in the SPG, producing a surge in otherwise slackening transport north out of the subtropics (Yeager et al., 2012).

MOM produces similar changes in inter-gyre heat transport in response to the changing NAO. Northward transport out of the subtropics increases through the early 1990s, before a drop and subsequent surge between 1995 and 1996 in both the TC and control simulations (Fig. 2.14a). This increase in STG to SPG heat transport is prolonged by ∼1 year in the TC run, resulting in poleward $\Delta OHT$ out of the STG of $0.2-0.25$ $PW$ between 1996 and 1998 (Fig. 2.14b). During the same period there is increased OHT across the southern face of the SPG region (Fig. 2.14c), in agreement with Yeager et al. (2012). The increased OHT into the SPG does not fully account for increases in heat export out of the STG (Fig. 2.14d).

This enhanced poleward transport of heat anomalies poleward as part of the large-scale changes in subtropical and subpolar gyre circulation is followed by increased outgoing heat flux in the subtropics (Fig. 2.15a). These OHT changes redistribute thermocline heat anomalies poleward within the STG, making them more susceptible to winter reventilation. The SPG loses heat through the ocean surface for prolonged periods between late-1992 and early-1995, and mid-1996 and late-1998 (Fig. 2.15b). Both periods correspond with elevated mean outgoing heat flux in the SPG under above average surface forcing during strongly positive NAO phasing shown in Fig. 2.13 (Yeager et al., 2012). The first of these OHT changes produces a small but sharp drop in North Atlantic $\Delta OHC$ in 1993 (Fig. 2.5a, 2.6a). The second, paired with the strong and prolonged heat loss within the STG is responsible for the ∼75% reduction in North Atlantic $\Delta OHC$ during the late 1990s.

The South Atlantic exhibits weaker $\Delta T$ than the North Atlantic, (Fig. 2.16), an expected consequence of the absence of direct TC forcing. Therefore, $\Delta T$ in

the South Atlantic must originate in regions of higher TC activity. An intermittent $\Delta T$ anomaly is present above $\sim$100 $m$, with $\sim$3$-$5 warm pulses per year, similar to the frequency of Agulhas Ring shedding found by Schouten (2002), implying an important teleconnection between warm anomalies generated in the South Indian Ocean and warming in the South Atlantic (Fig. 2.12). Formation of Agulhas Rings carrying positive $\Delta T$ into the South Atlantic is seen in the time evolution of the $\Delta T$ and $\Delta OHC$ fields (not shown).

South Atlantic $\Delta OHC$ (Fig. 2.5b, 2.6b) is small but relatively steady through the early 1990s. High frequency $\Delta OHC$ variability provides further evidence of export from the South Indian Ocean via Agulhas rings. A late-1990s drop in $\Delta OHC$ is due to a period of elevated $\Delta MHT$ towards the Southern Ocean (Fig. 2.11), resulting in the increases in $\Delta OHC$ seen there (Fig. 2.5h, 2.6h). After 1997, the deep ocean is noticeably greater negative $\Delta OHC$.

### 2.3.4 Indian ocean heat content anomalies

Seasonal increases in $\Delta T$ extend to nearly 150 $m$ in the South Indian Ocean (Fig. 2.18), with the warm anomaly at depth centered around 110 $m$. Much of the temporal variability is driven by seasonal heat uptake and ventilation, as in the North Atlantic. However, the relative impact of $\Delta T$ is large compared to the local TC forcing, with warming present below 110 $m$ that do not appear to originate in the downward propagating anomaly. These depths are the same as those reached by West Pacific warm anomalies advected equatorward, with one third of that anomalous heat entering the Indian Ocean via the Indonesian Throughflow (Bueti et al., 2014). Thus, while there is a local seasonal uptake of heat due to direct TC forcing, a significant portion of South Indian Ocean warm anomalies originate in the West Pacific.

South Indian Ocean $\Delta OHC$ (Fig. 2.5g, 2.6g) is steady and fairly consistent between the shallow and deep ocean until 1998, after which there is a sharp decline

through 2000. After 1998, the difference between shallow and deep $\Delta OHC$ increases, with the ocean below 739 $m$ cooled by $\sim 2 \cdot 10^{21}$ $J$. The $\sim 2 \cdot 10^{21}$ $J$ and $5 \cdot 10^{21}$ $J$ in the shallow and deep ocean, $\sim$10% and $\sim$40% of the respective trends in $OHC'_{Lev}$.

Higher frequency variability in South Indian $\Delta OHC$ exhibits strong covariance with that in South Atlantic $\Delta OHC$ (Fig. 2.5g/b, 2.6g/b), with a cross-covariance of 0.75 at lag times of around 2 months. As discussed in Section 2.3.3, this is suggestive of a pathway whereby Agulhas rings carry TC-induced heat anomalies from the South Indian Ocean into the South Atlantic, supplying a great deal of the $\Delta OHC$ present there. Export of heat anomalies from the South Indian to South Atlantic Ocean as part of the $\sim$0.5 $PW$ Agulhas Leakage (Ruijter et al., 1999) is consistent with a redistribution of locally generated South Indian and imported West Pacific warm anomalies via the South Equatorial, Mozambique, and Agulhas Currents (Fig. 2.12).

Periods of sharp interannual increases and decreases in $\Delta OHC$ are related to increasing and decreasing export of $\Delta OHC$ out of the West Pacific. The mechanisms driving this variability are discussed in Section 2.3.5. As in the South Atlantic, $\Delta OHC$ is exported out of the South Indian Ocean, illustrated by the MHT anomaly (Fig. 2.19). As $\Delta T$ is advected poleward (Fig. 2.17) some portion undergoes ventilation along the Antarctic Circumpolar Current (ACC).

The magnitude of $\Delta T$ in the North Indian Ocean is greater than expected given the local TC forcing (Fig. 2.20). As in the South Indian Ocean, heat input between 100 $m$ and 150 $m$ is present, resulting from leakage of West Pacific warm anomalies through the Indonesian Throughflow. This input of $\Delta OHC$ is further supported by the presence of intense ventilation that more than compensates for the TC induced warming (Fig. 2.21), with total heat loss through the ocean surface being equivalent to 140% of the direct TC driven warming (Table 2.2). In order for the noted strong warm anomaly in the upper thermocline to persist, a significant lateral heat flux

anomaly must be present. This North Indian Ocean warm anomaly (Fig. 2.20) averaged slightly less than $0.25°C$. $\Delta T$ in the North Indian Ocean extended fairly deeply and is persistent through the simulation, with the exception of particularly strong ventilation in 1998.

North Indian Ocean $\Delta OHC$ (Fig. 2.5f, 2.6f) slowly increases through the 1990s before decreasing after 1998. Shallow and deep $\Delta OHC$ are comparable until 1998, after which the North Indian Ocean below 739 $m$ is cooled by $\sim 0.5 \cdot 10^{21}$ $J$. The $\sim 1 \cdot 10^{21}$ $J$ variability in the shallow ocean and $\sim 1.75 \cdot 10^{21}$ $J$ through the full water column are equivalent to $\sim$20% and $\sim$24% of the respective trends in $OHC'_{Lev}$ over the same period. While the magnitude of the integrated $\Delta OHC$ is small compared to the other basins (Fig. 2.5f), the basin average $\Delta OHC$ is large (Fig. 2.6f), a result of the small size of the North Indian Ocean relative to other ocean regions (Table 2.1).

The impact of winter mixed layer deepening (Jansen and Ferrari, 2009) is not expected cause significant ventilation in the North Indian Ocean, as most of this region is equatorward of $20°N$. However, the continuing input of $\Delta OHC$ from the West Pacific and direct TC forcing does not result in continuously strengthening temperature and heat content anomalies (Fig. 2.20, Fig. 2.5f, Fig. 2.6f). Rather, strong ventilation is seen during the boreal summer, as shown by $\Delta Q$ integrated over the North Indian Ocean (Fig. 2.21).

### 2.3.5 South Asian Monsoon interaction

This enhanced outgoing heat flux corresponds with the onset of the summer southwest monsoon over the Arabian Sea and Bay of Bengal. The change in the monsoon is associated with a seasonal reversal in the NIO currents, most notably the Somali Current, that leads to periods of coastal upwelling off of Somalia, in the Arabian Sea, and Bay of Bengal (Schott and McCreary, 2001). Ventilation in these

regions is reflected in the outgoing heat flux anomalies in those regions present in Fig. 2.3. Rather than a balance between $\Delta OHC$ uptake due to summer TC forcing and winter reventilation by mixed layer deepening, the significant warming of the North Indian Ocean is supported by a balance between lateral import of heat anomalies from the West Pacific and ventilation by monsoon driven upwelling.

SST anomalies in the Arabian Sea have long been seen as a control on the strength of the South Asian summer monsoon (Shukla, 1975) with positive $\Delta SST$ associated with a more intense summer monsoon due to enhanced evaporative heat fluxes at the ocean surface. More recent coupled-model work by Yang et al. (2007) connected early summer mixed layer temperature anomalies of $\sim 0.5^{\circ}C$ off of the Somali coast to a strengthening of cross-equatorial southwest monsoon winds and elevated precipitation over the Indian subcontinent.

While of a lesser spatial extent, the TC-induced SST and corresponding mixed layer temperature anomalies found in this region between May and July (Fig. 2.2) are of a similar magnitude to those imposed by Yang et al. (2007). This early summer SST anomaly suggests a potential influence of TC warming on monsoon variability, further exploration of which is precluded by the uncoupled nature of the experimental design.

### 2.3.6 Pacific ocean heat content anomalies

$\Delta T$ in the West Pacific (Fig. 2.22) undergoes periods of generation and ventilation similar to the North Atlantic. Warm anomalies are stronger and of greater duration, consistent with the greater duration and intensity of the West Pacific typhoon season. The warm anomaly is centered somewhat deeper than in the North Atlantic, at 150 $m$, reflecting the impact of both higher wind speeds and weaker stratification in the region, allowing for deeper penetration of mixing as discussed in Bueti et al. (2014). While ventilation is present, it is not of a great enough magnitude or

depth to prevent continuing accumulation of West Pacific warming, a fact reflected in the dominantly positive phasing of the surface heat flux anomaly in the West Pacific (Fig. 2.23), with 65% of anomalous heat input through the ocean surface either accumulating in the upper-thermocline or exported laterally (Table 2.2). Anomalous heat is advected by the tropical pathways described in Bueti et al. (2014) (Fig. 2.12), deepening as it moves equatorward through the fall and winter to $\sim$160 $m$ and shoaling along the EUC through spring, entering either the East Pacific (Fig. 2.24) at $\sim$130 $m$ or the South Pacific (Fig. 2.25) at $\sim$160 $m$. The amplitude of the West Pacific temperature anomaly is modulated on interannual timescales, with warming amplified in 1992 and 1997-1998, a small decrease in 1995, and sharp attenuation between 1999 and 2002.

West Pacific $\Delta OHC$ ($\Delta OHC_{WP}$; Fig. 2.5c, 2.6c) is relatively steady at $\sim 2 \cdot 10^{21}$ $J$ from 1992-1998, with a sharp drop and recovery in 1995. This period is bounded by a $\sim 3 \cdot 10^{21}$ $J$ decline in $\Delta OHC_{WP}$ in late-1991 and nearly $5 \cdot 10^{21}$ $J$ decline between 1998 and 2000. Shallow and total $\Delta OHC_{WP}$ are fairly consistent until the mid-1990s, after which an increasing amount of anomalous heat is found below 739 $m$. The late-1990s decline in $\Delta OHC_{WP}$ is equivalent to a 33% and 25% decrease in the respective $OHC'_{Lev}$ trends during the same period. Note that this comparison is made against the increase in total North Pacific OHC, as Levitus et al. (2012a) did not separate out the West and East Pacific.

$\Delta T$ is more persistent in the East Pacific (Fig. 2.24) and somewhat shallower, with the anomaly centered around 100 $m$. Warming at depth is not proportional to local TC forcing or mixed layer cooling, reflecting the input of $\Delta T$ from the West Pacific. Ventilation is stronger here than the downward heat pumping (Fig. 2.26), reflecting the near constant upwelling of warm anomalies in the tropical East Pacific and releasing anomalous heat up to 170% of that added to the ocean by local TC

forcing. Lateral import of warm anomalies must be present in order to close the heat anomaly budget in the East Pacific and maintain a warm anomaly at depth. The signature of $\Delta T$ ventilation is strongly suppressed in 1992, 1997, and 2002, while it is enhanced in 1996, 1999, and 2001.

The East Pacific accumulates $\Delta OHC$ ($\Delta OHC_{EP}$) through the 1990s (Fig. 2.5d, 2.6d). This trend is particularly large in late-1991, and between 1999 and 2000, and is the reverse of interannual variability seen in $\Delta OHC_{WP}$. This result is consistent with the large-scale redistribution of heat anomalies from the West to the East Pacific, consistent with the discussed EUC pathways. Deep $\Delta OHC_{EP}$ exceeds that in the upper ocean by $\sim 0.75 \cdot 10^{21}\ J$ in the mid-1990s. The $5.5 \cdot 10^{21}\ J$ increase in shallow $\Delta OHC_{EP}$ and $7.6 \cdot 10^{21}\ J$ increase in deep $\Delta OHC_{EP}$ corresponds with 37% and 38% of the respective $OHC'_{Lev}$ trends in the North Pacific, more than compensating for the decreases in $\Delta OHC_{WP}$.

$\Delta T$ in the South Pacific (Fig. 2.25) exhibits warming patterns similar to those in the East Pacific, with direct generation of TC warm anomalies during the austral summer and import of heat from the West Pacific at $150-160\ m$ that shoals along the tropical thermocline. Both seasonal reventilation due to local winter mixed layer deepening (Jansen and Ferrari, 2009) and year-round reventilation induced by tropical upwelling are present (Fig. 2.12). While interannual variations in $\Delta T$ follow a similar pattern to those in the East Pacific, they are neither as strong nor as persistent, with export to the Southern Ocean mitigating long-term accumulation.

South Pacific $\Delta OHC$ ($\Delta OHC_{SP}$; Fig. 2.5d, 2.6d) increases somewhat through 2001, with a sharp decrease and recovery in late 1994. $\Delta OHC_{SP}$ decreases sharply after 2001 and recovers in 2004. As with $\Delta OHC_{EP}$, $\Delta OHC_{SP}$ variability is counter to that in $\Delta OHC_{WP}$, with much of the anomalous heat supply in the South Pacific coming at the expense of the subtropical West Pacific. Most $\Delta OHC_{SP}$ is contained

above 739 $m$, with a non-negligible portion penetrating into the deeper ocean during the 1990s. Fluctuations in shallow $\Delta OHC_{SP}$ ($\sim 2.5 \cdot 10^{21}$ $J$) and deep $\Delta OHC_{SP}$ ($\sim 5 \cdot 10^{21}$ $J$) corresponds with $\sim$33% and 75% of the trends in $OHC'_{Lev}$ in the region.

The picture of $\Delta OHC_{WP}$ export to the East and South Pacific via tropical pathways as inferred here from the regional $\Delta OHC$ and described in more detail in Bueti et al. (2014) is further supported by analysis of the Pacific-Indian $\Delta MHT$. (Fig. 2.19). $\Delta MHT$ exhibits a consistent poleward export of heat from the northern subtropics which is reventilated during the austral summer. As expected, a strong equatorward export of heat is present, with $\Delta MHT$ convergence between $10°N$ and $10°S$. Also of note is the relatively weak accumulation of heat in the tropics during the 2000s compared to the 1990s.

Redistribution of heat from the subtropical West Pacific to the equatorial region by $\Delta MHT$ is linked to a zonal heat transport anomaly across the boundary between the tropical West and East Pacific (Fig. 2.12,2.27)

$$\Delta OHT_x(t) = \left[ c_p \rho_o \int_{10°S}^{10°S} dy \int_{-739\ m}^{0\ m} dz \Delta \left( u(x,y,z,t) \cdot T(x,y,z,t) \right) \right]_{x=180°} \tag{2.5}$$

that is responsible for increases in $\Delta OHC_{EP}$ at the expense of $\Delta OHC_{WP}$. $\Delta OHT_x$ transitions between positive (eastward) and negative (westward) phases, with predominantly eastward $\overline{\Delta OHT_x} \approx 76$ $TW$ (0.3 $PW$ during positive phases). $\Delta OHT_x$ is suppressed in late 1991, mid-1997 through mid-1998, and early-2001 through 2002. These periods of decreased $\Delta OHT_x$ corresponds with those of increases in $\Delta OHC_{WP}$ and either decreasing or stable $\Delta OHC_{EP}$.

### 2.3.7 El Niño-Southern Oscillation interaction

Large changes in $\Delta OHT_x$ and $\Delta OHC_{WP}$ take place on timescales comparable to those of ENSO. With the redistribution of heat anomalies in the Pacific being dictated by tropical pathways, changes in those pathways linked to ENSO variability

are expected to modulate TC-induced heating. To that end, the skill of the model configuration in reproducing ENSO variability is evaluated. The SST time anomaly ($SST'$) in the Niño-3.4 region, referred to as the "Oceanic Niño Index" (ONI), is a well-accepted metric for capturing the ocean's ENSO variability (Trenberth, 1997). ONI observation data is obtained from the NOAA Climate Prediction Center (CPC) for comparison with the model output (Fig. 2.28). MOM captures the observed ONI variability extremely well, as expected under the constraint of a prescribed atmosphere. TC heating is not found to have a significant influence on ENSO SST variability in the ocean only simulation.

The subsurface ENSO response in MOM is expressed as the temperature time anomaly ($T'$) in the central tropical Pacific ($160°E-80°W$) averaged to 300 $m$ (Fig. 2.29a,b,c). While MOM exhibits warm/cold phasing consistent with the CPC observational record through 2000, the last 5 years are characterized by a distinct cold bias in $T'$. The amplitude of the subsurface ENSO variability is generally lower than in the CPC data. Specifically, the El Niño events of 1992, 1994-1995, 1997, and 2002 are $50-75\%$ cooler than those in the CPC record, while the 1998 La Niña is $\sim 50\%$ warmer.

TC warming has a small but non-negligible effect on the subsurface expression of ENSO (Fig. 27d). The 1992 El Niño is $\sim 20\%$ weaker in the TC run than control, the 1994-1995 and 2002 events are 8% weaker, and the 1998 La Niña is $\sim 5\%$ weaker at its peak. The 1997 El Niño, notable for being the most intense in the CPC record, is unaffected by TC warming at its peak, with the only notable changes being a $\sim 30\%$ intensification of the early phase of warming and a delay in the transition from El Niño to La Niña conditions. Much of the impact is on so-called El Niño "Modoki" events (Ashok et al., 2007), characterized by a deepening of the tropical Pacific thermocline (specified by the $27°C$ isotherm depth in Fig. 2.30a,b) between $\sim 170°E$ and $155°W$.

In contrast, the "classical" El Niño of 1997 exhibits a greater eastward relocation in the maximum thermocline depth to $160°W-120°W$. The impact of TC-induced thermocline anomalies on thermocline depth (Fig. 2.30c) is constrained to west of $\sim 140°W$ (a pattern present in analysis of the $22°C$ and $25°C$ isotherms as well).

A deepening of the Central Pacific thermocline and eastward shift of outcropping isotherms is found in non-El Niño years. This deepening biases the average state of the Central Pacific in the TC runs towards a more El Niño-like state, and subsequently reduces the amplitude of the El Niño Modoki signature at depth. Warming at depth weakens La Niña cooling, damping the negative ENSO signal. Together, these effects result in an overall damping ENSO variability in the ocean interior due to TC forcing. Given this impact, a feedback between TC warming, changes in surface temperatures, outgoing fluxes, and the atmospheric side of ENSO may be expected. However, the uncoupled configuration of the model used here precludes exploration of such a feedback, as the specified surface conditions in the tropics highly constrain the near-surface ENSO variability and do not allow for the ocean to influence atmospheric conditions.

ENSO variability is expected to have a greater impact on the redistribution of $\Delta OHC$ in the tropical Pacific. A strong correlation exists between ONI (Fig. 2.28), $\Delta OHC_{WP}$ (Fig. 2.5c), $\Delta OHT_x$ (Fig. 2.27), $\Delta OHC_{Eq}$ (Fig. 2.31), and tropical East Pacific $\Delta Q$ (Fig. 2.32). $\Delta Q$ here is integrated from $180°W$ to $70°W$ and $10°S$ to $10°N$. Izumo (2005) showed that mass transport in the shallow Pacific meridional overturning cells (McCreary and Lu, 1994) and the EUC is weaker during El Niños and stronger during La Niñas, driving corresponding changes in OHT. Upwelling in the East Pacific is found to vary over the same timescales, with La Niña characterized by enhanced upwelling and El Niño by weakened upwelling (Wang, 2001). Changes in subtropical-tropical overturning, tropical East Pacific upwelling, and ENSO mod-

ulation of mean heat transport in tropical pathways have implications for anomalous heat transport discussed in Bueti et al. (2014) and tropical ventilation of $\Delta OHC$ presented here and in Vincent et al. (2013).

The onset of an El Niño leads to reductions in $\Delta OHT_x$ and $\Delta Q$. Heat export out of the subtropical West Pacific weakens during these periods, with longer residence time of warm anomalies in the subtropics leading to greater outgoing heat fluxes in the region during the winter (Fig. 2.23) driven by the mixed layer deepening mechanism of Jansen et al. (2010). Slackening in anomalous heat transport in the EUC produces a sharp reduction in $\Delta OHC_{Eq}$ relative to the mean trend (Fig. 2.27). Below average $\Delta Q$ (Fig. 2.32) allows above average accumulation of $\Delta OHC_{Eq}$ to occur as the El Niño evolves. The subsequent transition to La Niña accelerates EUC heat transport and enhances equatorward $\Delta MHT$ in the subtropical-tropical cell, leading to an initial increase in both $\Delta OHT_x$ and $\Delta OHC_{Eq}$. Upwelling increases as the La Niña deepens, enhancing $\Delta Q$ and decreasing $\Delta OHC_{Eq}$ relative to the average trend.

With the 1997 El Niño as an example, reduced $\Delta OHT_x$ in the EUC and corresponding below average upwelling in the East Pacific leads to reduced $\Delta F$ in the equatorial East Pacific. Lower $\Delta Q$ allows for above average increases in $\Delta OHC_{Eq}$. The subsequent transition to La Niña is accompanied by a sharp increase in $\Delta OHT_x$, accelerated ventilation of warm anomalies under increased upwelling, and reduced $\Delta OHC_{Eq}$.

Transitions to El Niño provide for increased $\Delta OHC_{WP}$, and flat or decreasing $\Delta OHC_{EP}$ and $\Delta OHC_{SP}$ as less $\Delta OHC_{WP}$ is exported to the tropics. Transitions to La Niña accelerate the increase of $\Delta OHC_{EP}$ and $\Delta OHC_{SP}$ at the expense of $\Delta OHC_{WP}$, and are the periods during which accumulated TC-induced heating in the Pacific is most efficiently released to the tropical atmosphere. In this way, ENSO

driven changes in ocean circulation are a key mechanism in the modulation of TC-induced warming in the Pacific.

## 2.4 Discussion

As discussed by Bueti et al. (2014), TC-induced thermocline warming is a non-negligible source of heat uptake to the ocean over the course of a single simulated year. Such a heat input has been hypothesized to have a significant impact on the total meridional heat transport poleward out of the subtropics (Emanuel, 2001). However, we find that the long-term TC impact on MHT is not a significant driver of the ocean climate system, on the order of 2% of the mean global, Atlantic-Arctic, and Pacific-Indian MHT, in agreement with the work of Vincent et al. (2013) and Scoccimarro et al. (2011), both of which showed a negligible average contribution by TCs to the MHT over 20-year runs in ocean only and fully coupled modeling frameworks. However, the impact of TC heat pumping on the ocean heat content, both globally and regionally, reaches a significant percentage of the increases in OHC over the same period quantified by Levitus et al. (2012a), signifying that regional TC-induced warm anomalies are a non-negligible part of regional ocean heat budgets.

Past studies have focused on the importance of interseasonal variability in the uptake, persistence, and ventilation of TC-induced ocean heating (Bueti et al., 2014; Vincent et al., 2013; Jansen and Ferrari, 2009). While the annual uptake and discharge of TC heating is an important mechanism in maintaining the oceans quasi-equilibrium, we find greater modulation over interannual timescales. The character of global variability described in Section 2.3.2 is in fact set by regional climate processes, which allow for periods of anomalous heat accumulation and ventilation. In many ways, TC-induced $\Delta OHC$ behaves as an active tracer in the ocean circulation (Fig. 2.12) and as such its accumulation and discharge is governed by the large-scale variability of the ocean climate system. The persistence of warm anomalies in the

Atlantic, Indian, and Pacific oceans is largely modulated by the ocean response to the North Atlantic Oscillation, monsoon winds, and the El Niño-Southern Oscillation.

While an average global ocean response to TC warming can be derived, ocean adjustment is taking place on a regional basis, and should be quantified as such. Laterally advected TC-induced temperature anomalies make significant contributions to the upper-thermocline temperatures of the North Indian Ocean and East Pacific, and are responsible for as much as $0.25°C$ of warming there. At the same time, seasonal ventilation and lateral advection curtail the long-term warming effect of TCs on the North Atlantic and West Pacific, the regions of greatest TC activity. The continuing increase of $\Delta OHC$ in the equatorial Pacific (Fig. 2.31) had not fully adjusted in the integration time of this experiment, and may very well play an important role in augmentation of the heat budget and fluxes in this important region.

The experimental design used here provides an improved understanding of the processes, pathways, and timescales by which the ocean adjusts to TC heat uptake in a straightforward manner. However, the ocean-only nature of the model framework precludes quantification of any downstream effects that anomalous heat exchange between the ocean and atmosphere may have on the climate system. Changes in the heat flux anomalies in the tropical East Pacific upwelling region and North Indian Ocean upwelling regions could have an impact on coupled ocean-atmosphere processes such as ENSO and the South Asian monsoon. The inability of the prescribed atmosphere to respond to the sea surface state also provided somewhat less realistic air-sea heat fluxes than would be desired. As such, we advocate the use of a fully coupled model framework, such as that utilized by Scoccimarro et al. (2011), with an ocean model of sufficient resolution to address the processes discussed here.

Heat export into the polar basins is found over the course of the experiment,

with sub-surface warming of the Arctic Ocean (Fig. 2.5i, 2.6i) and ACC (Fig. 2.5h, 2.6h). The direct impact of this warming is not addressed here, as this study sought to address the upper-ocean response to TC warming. However, warm anomalies exported to high latitudes appear to be subducted in the Southern Ocean (Fig. 2.17) and mixed downward in the Arctic. These processes have potential implications for altering the water mass properties of the Antarctic Intermediate and North Atlantic Deep Waters, and may explain the differences between deep and shallow $\Delta OHC$ seen in the 2000s. Given the long timescales over which the deep circulation evolves, a 15-year simulation such as the one presented here is insufficient for evaluating such an impact, and a multi-decadal, high-resolution ocean study would prove a valuable tool in properly capturing the full impact of tropical cyclone warming on the full ocean.

Table 2.1. Surface area of analysis ocean basins from Fig. 2.8.

| Region | Area (million $km^2$) |
|---|---|
| North Atlantic | 49.13 |
| South Atlantic | 22.64 |
| West Pacific | 36.86 |
| East Pacific | 45.39 |
| South Pacific | 55.98 |
| North Indian | 11.97 |
| South Indian | 34.51 |
| Southern Ocean | 94.28 |
| Arctic Ocean | 12.87 |
| Global Ocean | 357.63 |

Table 2.2. Total changes in $\Delta OHC$ due to surface fluxes anomalies ($\Delta OHC_{\Delta Q}$), and due to its positive ($\Delta OHC_{\Delta Q+}$) and negative ($\Delta OHC_{\Delta Q-}$) excursions. These values are calculated as the time integral of the time series presented in Fig. 2.10, 2.21, 2.23, 2.26.

| Region | $\Delta OHC_{\Delta Q}$ ($10^{21}$ $J$) | $\Delta OHC_{\Delta Q+}$ ($10^{21}$ $J$) | $\Delta OHC_{\Delta Q-}$ ($10^{21}$ $J$) |
|---|---|---|---|
| North Atlantic | 6.64 | 18.45 | -11.81 |
| West Pacific | 18.96 | 29.37 | -10.42 |
| East Pacific | -6.21 | 9.11 | -15.32 |
| North Indian | -0.89 | 2.32 | -3.22 |

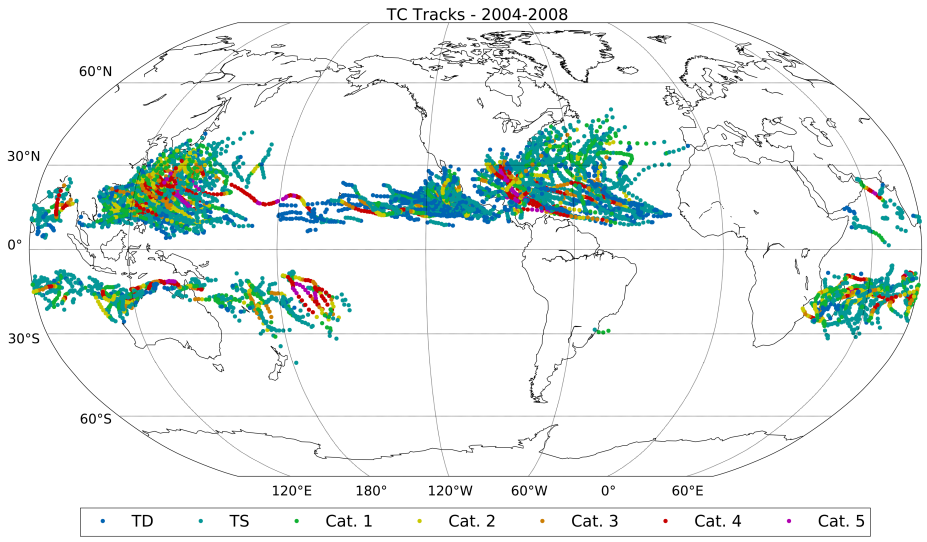


Figure 2.1. TC tracks from 1 January 2004 through 31 December 2008, used as the 5-year repeated forcing in the TC experiment.

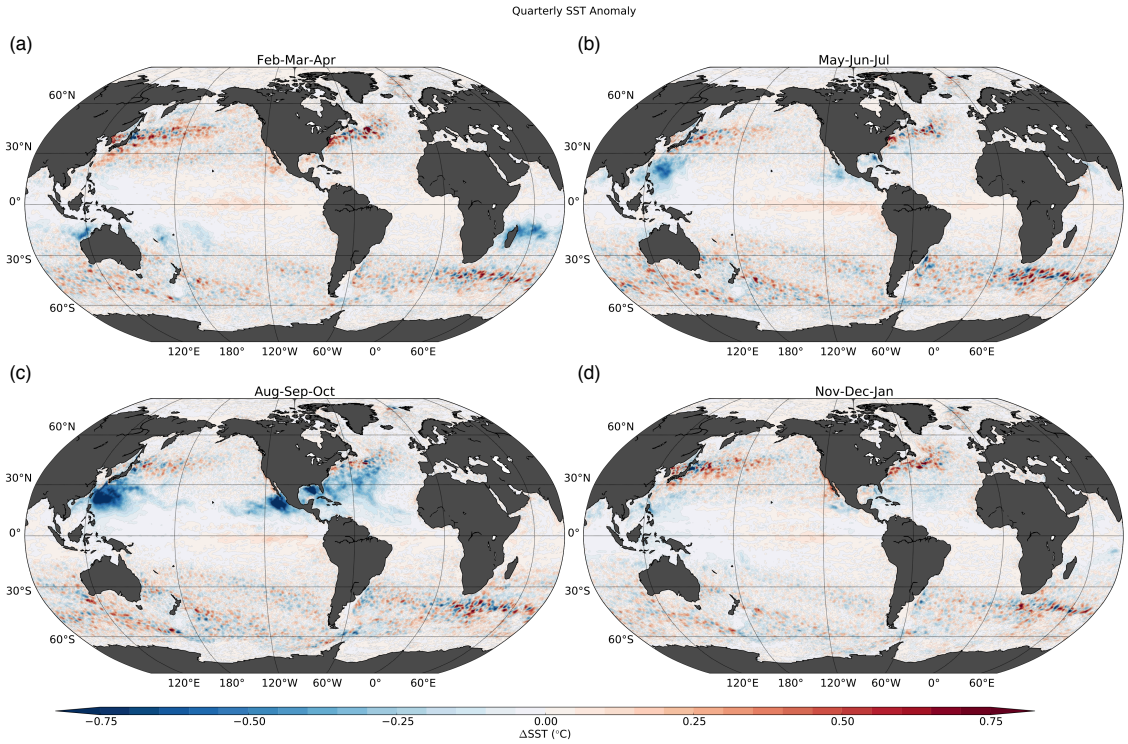


Figure 2.2. (a) February-April, (b) May-July, (c) August-October, and (d) November-January $\Delta SST$ averaged from 1985 through 2004.

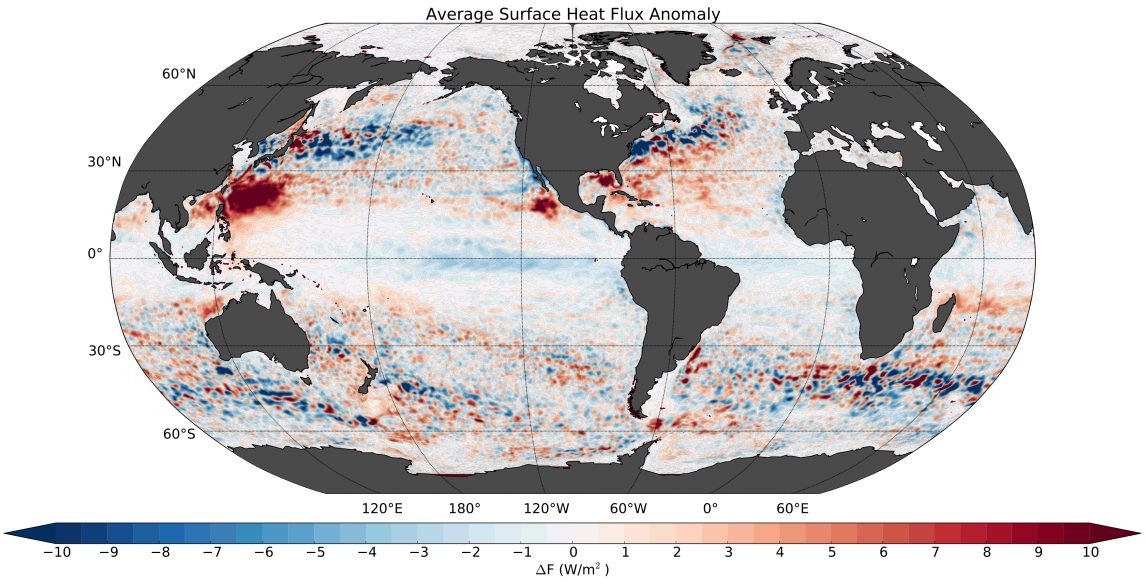


Figure 2.3. Total incoming heat flux anomaly ($\Delta F$) at the ocean surface, averaged from 1985 through 2004.

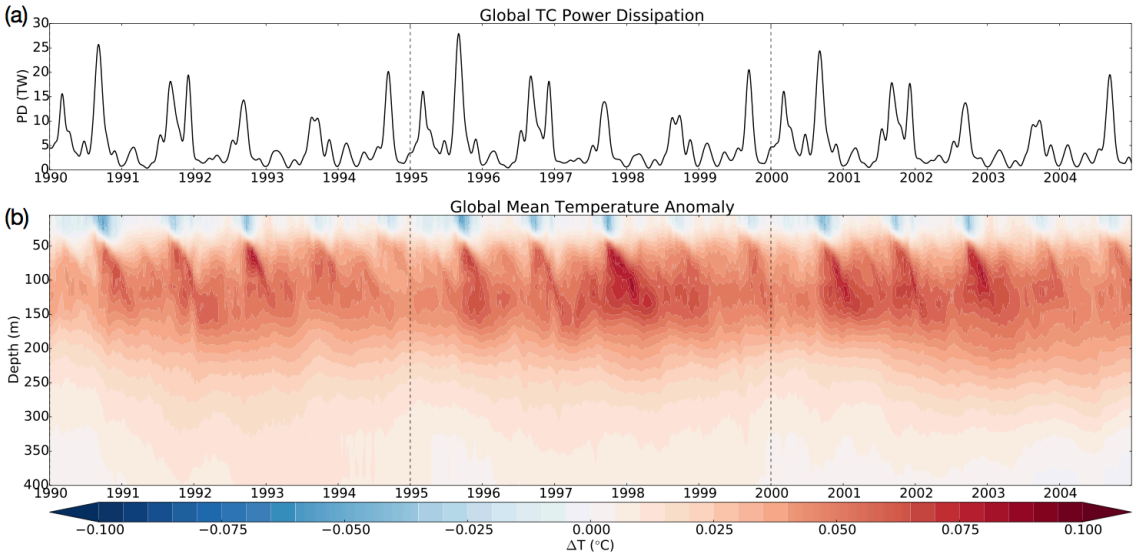


Figure 2.4. (a) Globally integrated TC power dissipation (91-day smoothed), showing the magnitude of TC forcing on the ocean. (b) Mean global temperature anomaly as a function of time and depth.

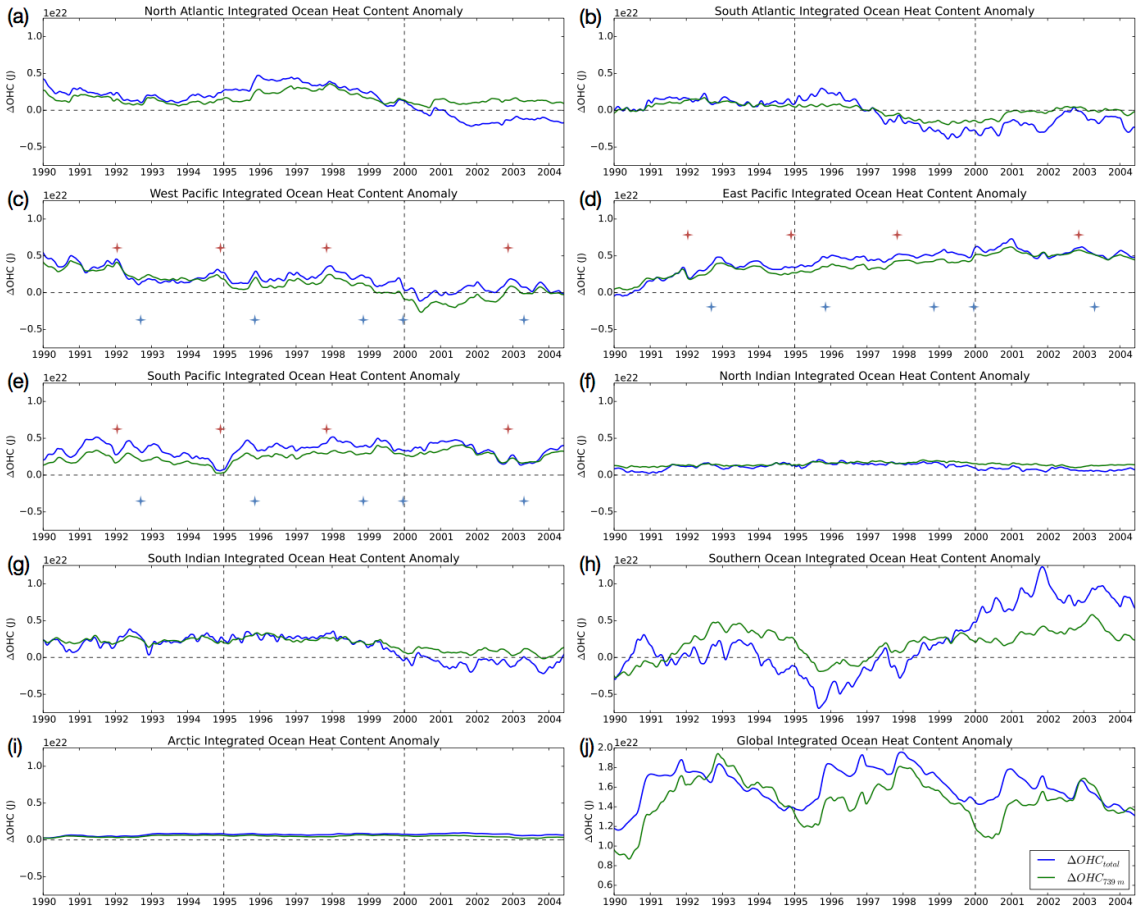


Figure 2.5. Ocean heat content anomaly integrated over the ocean regions shown in Fig. 2.8 and enumerated in Table 2.1. $\Delta OHC$ is calculated to the ocean bottom (blue) and the 739 $m$ depth level (green). Red (blue) markers in the Pacific time series indicate peak El Niño (La Niña) events.

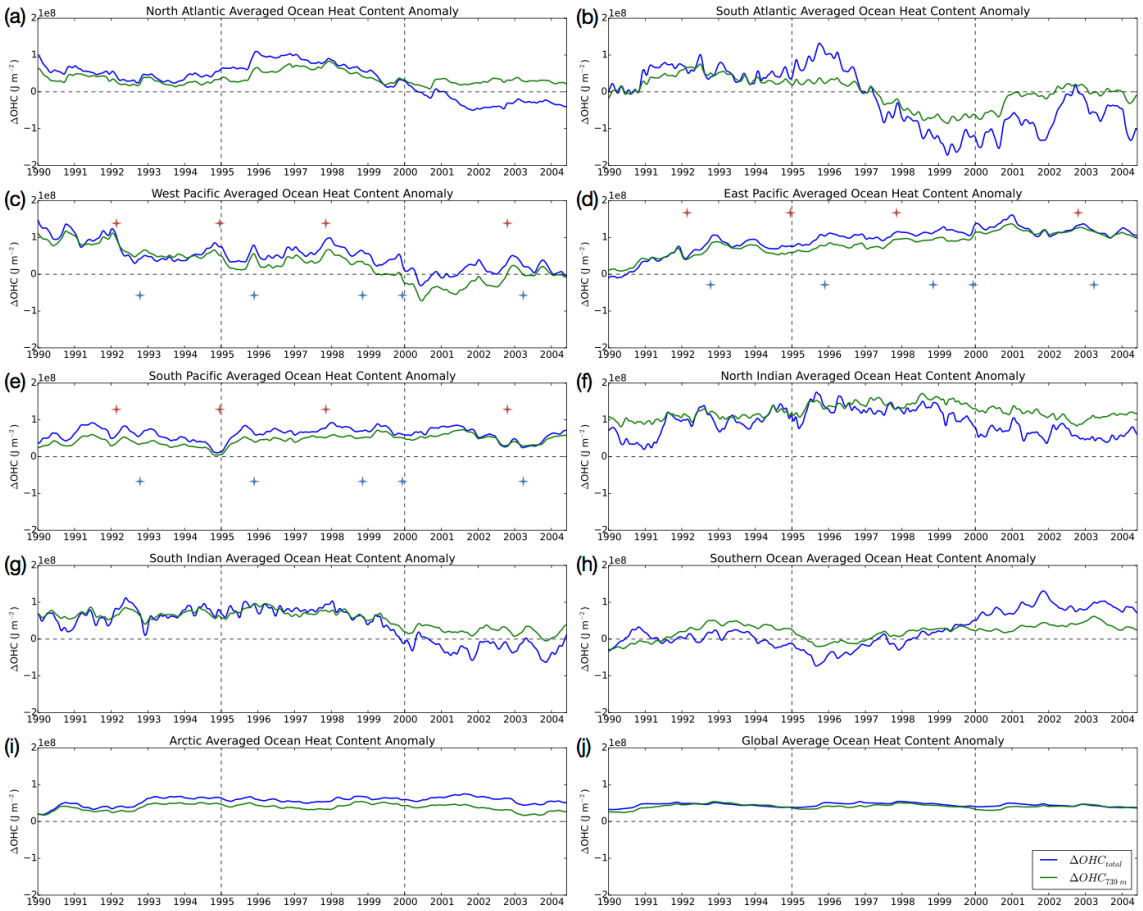


Figure 2.6. Ocean heat content anomaly averaged over the ocean regions shown in Fig. 2.8 and enumerated in Table 2.1. $\Delta OHC$ is calculated to the ocean bottom (blue) and the 739 $m$ depth level (green). Red (blue) markers in the Pacific time series indicate peak El Niño (La Niña) events.

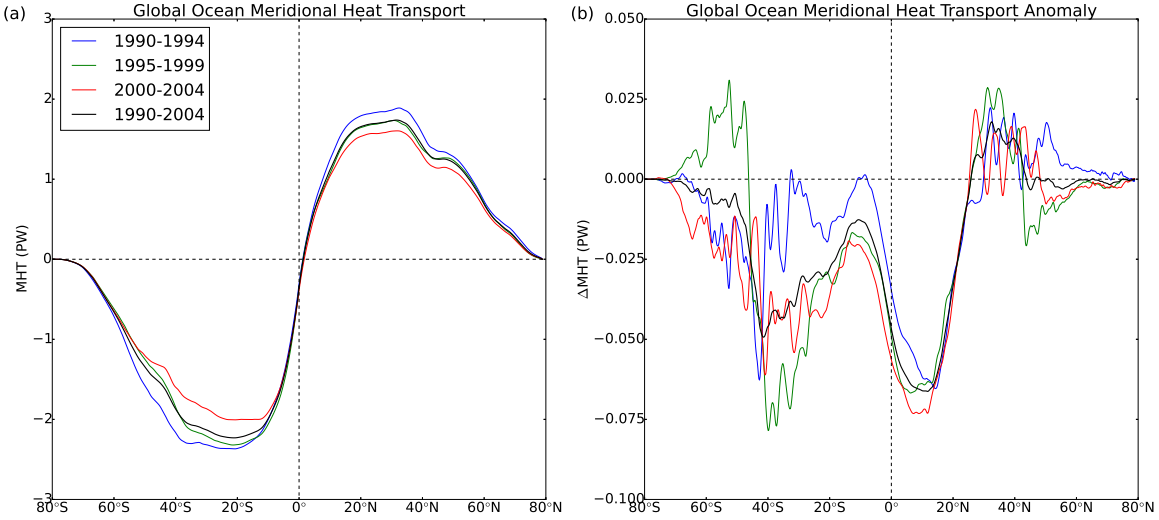


Figure 2.7. TC-induced anomaly in (a) and total (b) globally integrated meridional heat transport. $\Delta MHT$ and MHT are averaged from 1990-2004, and within each of the 5-year TC repeats.

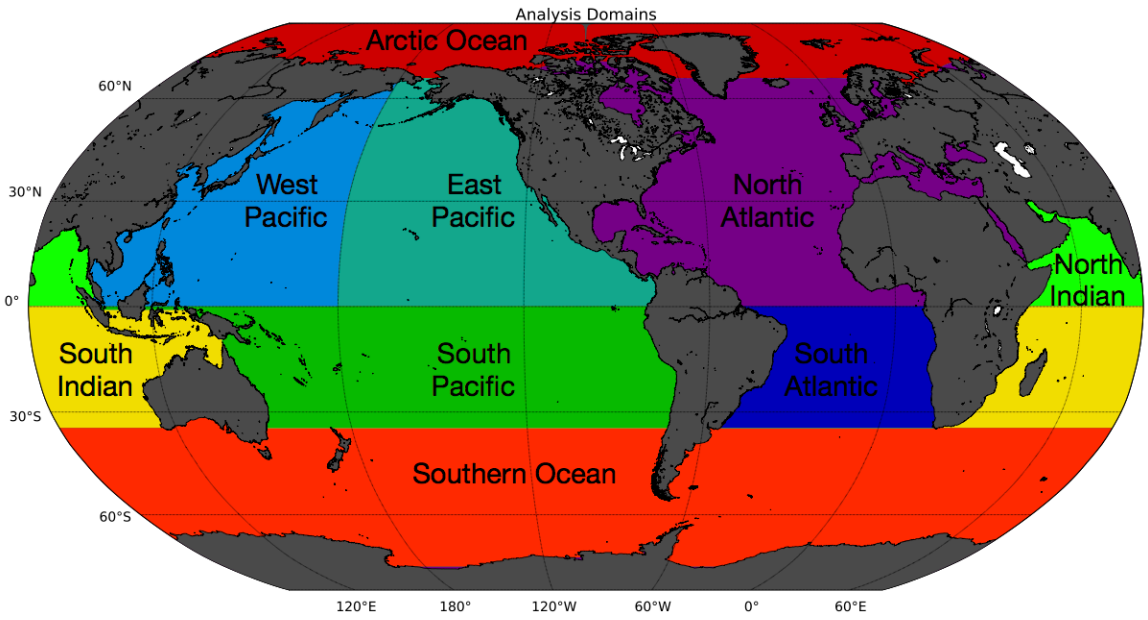


Figure 2.8. Map of the ocean domains used in average and integrated analyses, as described in Table 1.

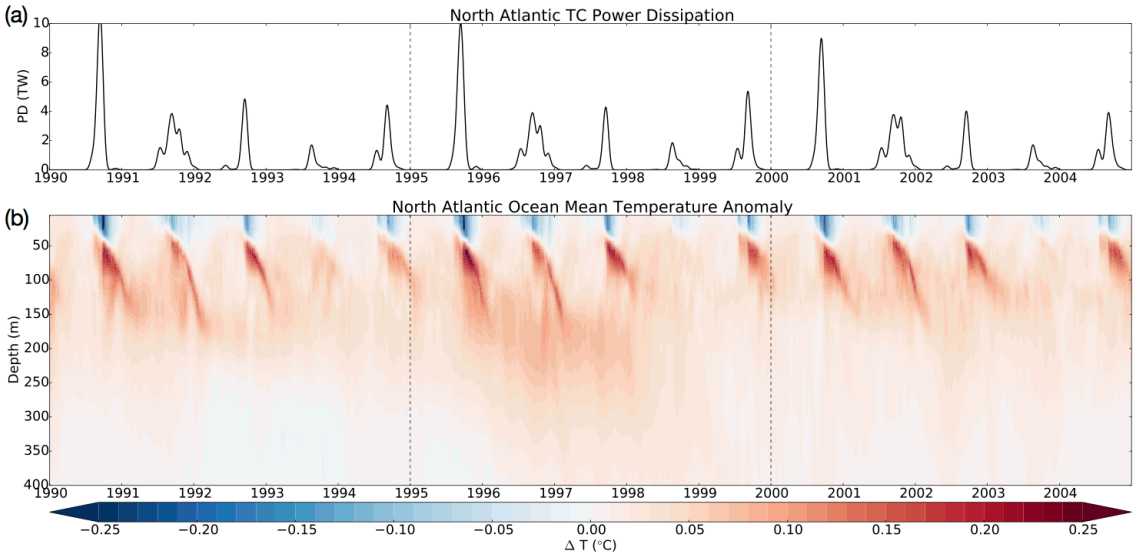


Figure 2.9. (a) TC power dissipation (91-day smoothed) integrated over the North Atlantic, showing the magnitude of TC forcing on the ocean. (b) Mean North Atlantic temperature anomaly as a function of time and depth.

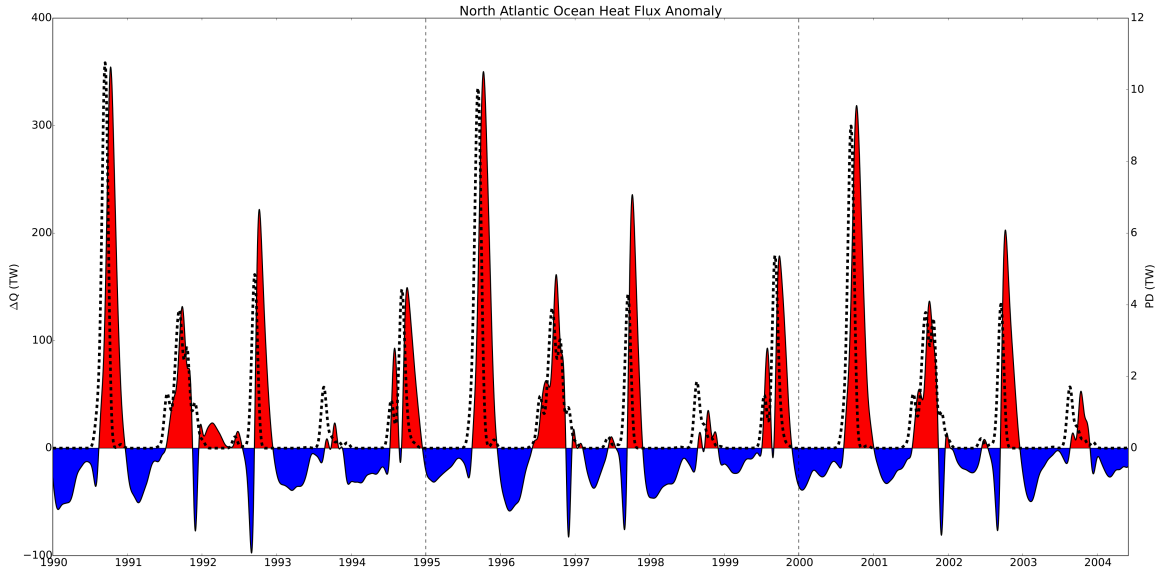


Figure 2.10. The difference between the total incoming surface heat flux between TC and control in the North Atlantic. Positive values indicate anomalous heat uptake, negative ventilation of TC anomalies to the atmosphere, and the dashed line is the TC power dissipation in the region.

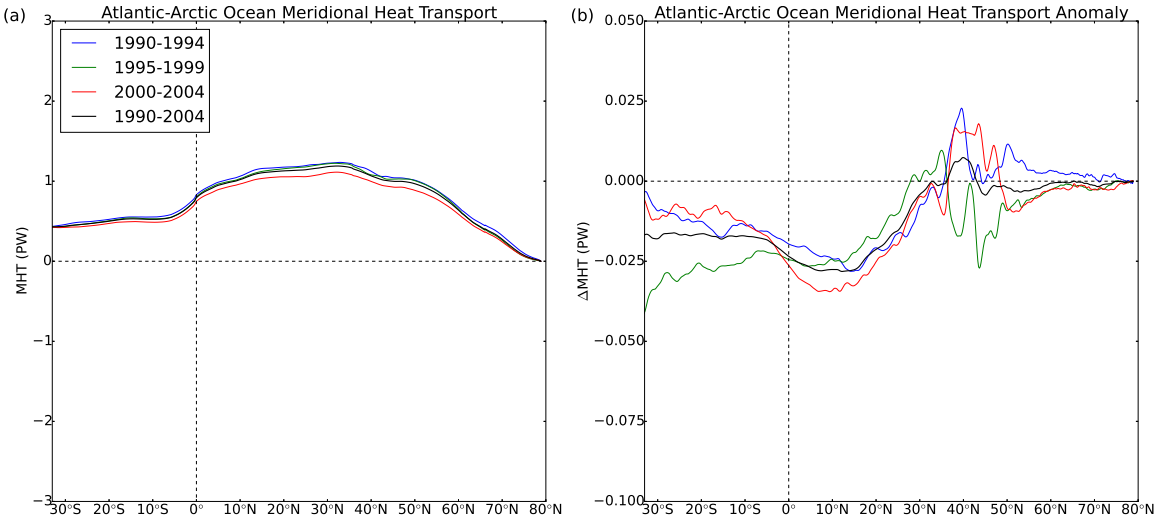


Figure 2.11. TC-induced anomaly in (a) and total (b) Atlantic-Arctic Ocean integrated meridional heat transport. $\Delta MHT$ and MHT are averaged from 1990-2004, and within each of the 5-year TC repeats.

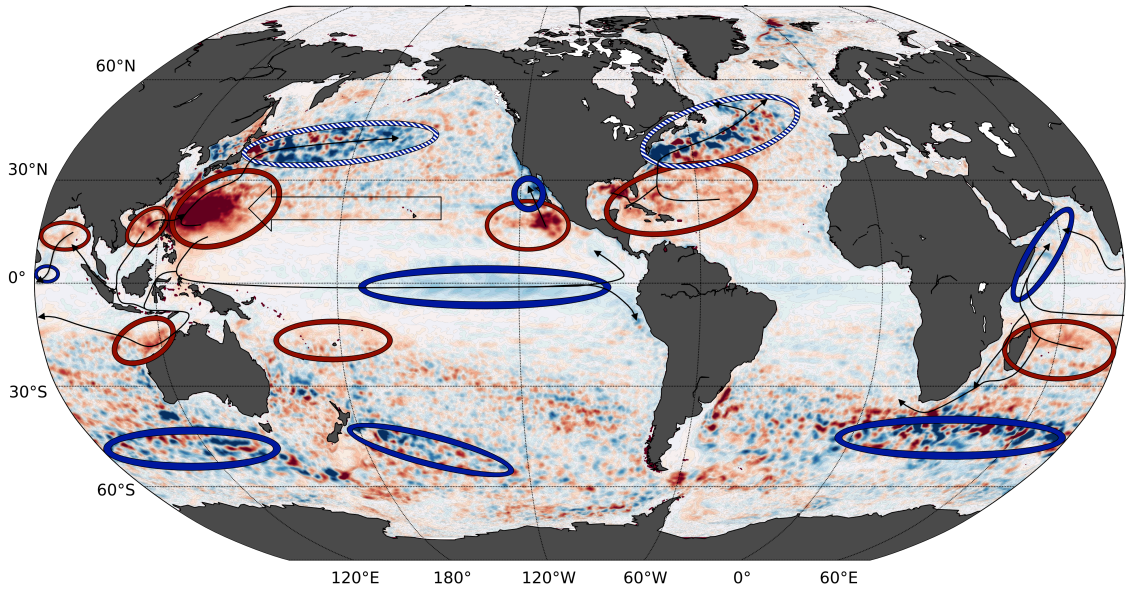


Figure 2.12. Schematic displaying regions of heat uptake and ventilation by the ocean, overlaid on the average surface heat flux anomalies from Fig. 2.3. Red circles indicate regions of anomalous heat gain due to anomalous incoming heat fluxes. Solid blue circles indicate regions of anomalous outgoing heat fluxes due to warm anomalies brought to the surface in equatorial, frontal, and coastal upwelling regions, while dashed blue circles indicate reventilation of $\Delta OHC$ due to winter mixed layer deepening (Jansen et al., 2010). Solid black arrows represent rapid advective pathways which redistribute heat to regions of ventilation and accumulation. The large outlined arrow indicates slower self-propagation of TC warm anomalies as nonlinear Rossby-like eddy (Jansen et al., 2010). Note that this schematic is illustrative, and not intended to be a precise or comprehensive representation of the physical mechanisms of interest.

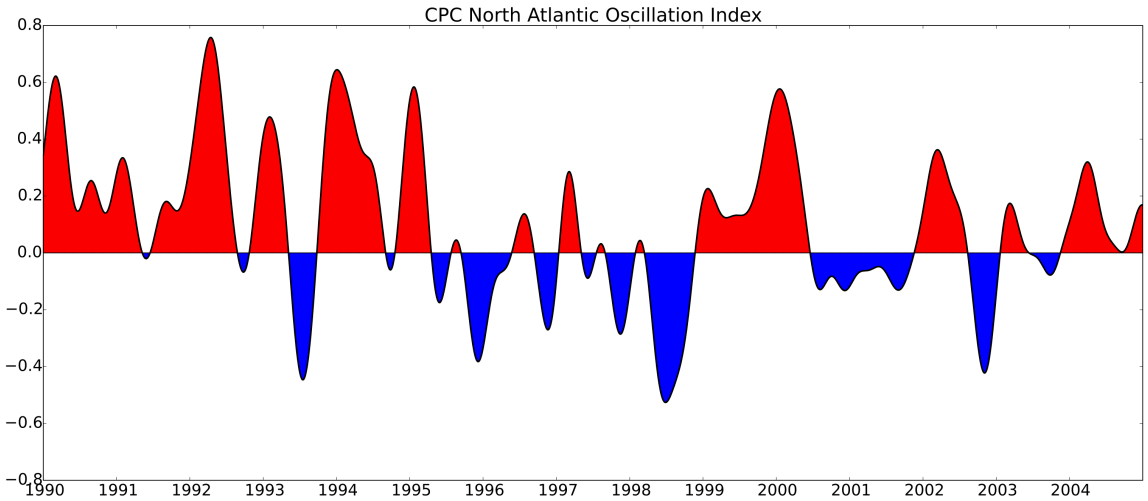


Figure 2.13. The North Atlantic Oscillation index CPC time series, representing the relative change in atmospheric sea level pressure between the Icelandic low and Azores high.

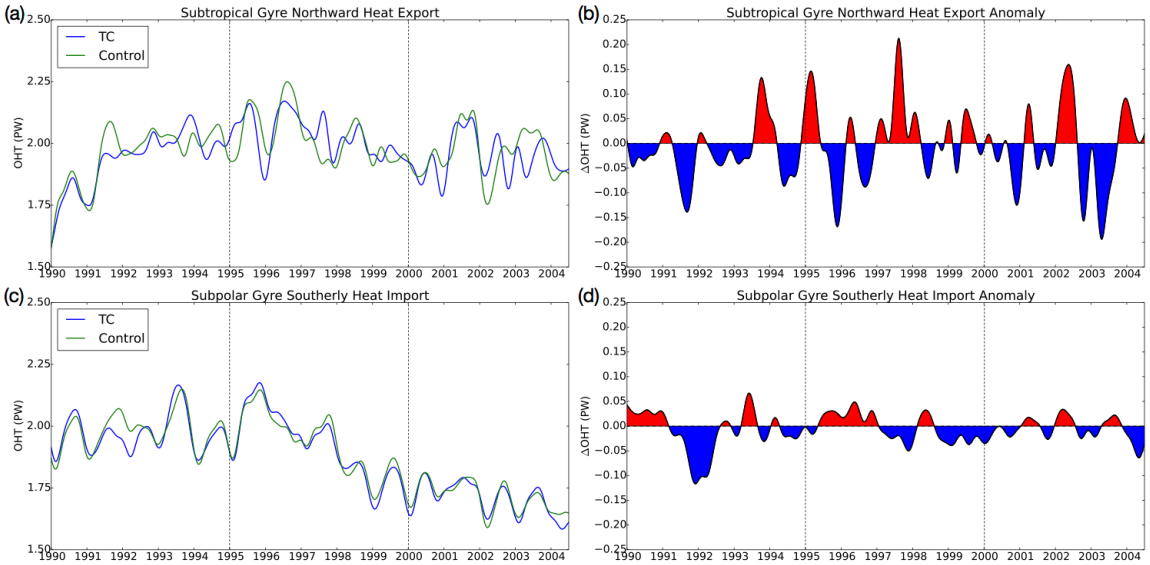


Figure 2.14. 3-month smoothed northward advective heat transport out of the Atlantic subtropical gyre region (a) and its anomaly between the TC and control experiments (b). The same for the northward advective heat transport into the Atlantic subpolar gyre region (c) and its anomaly (d).

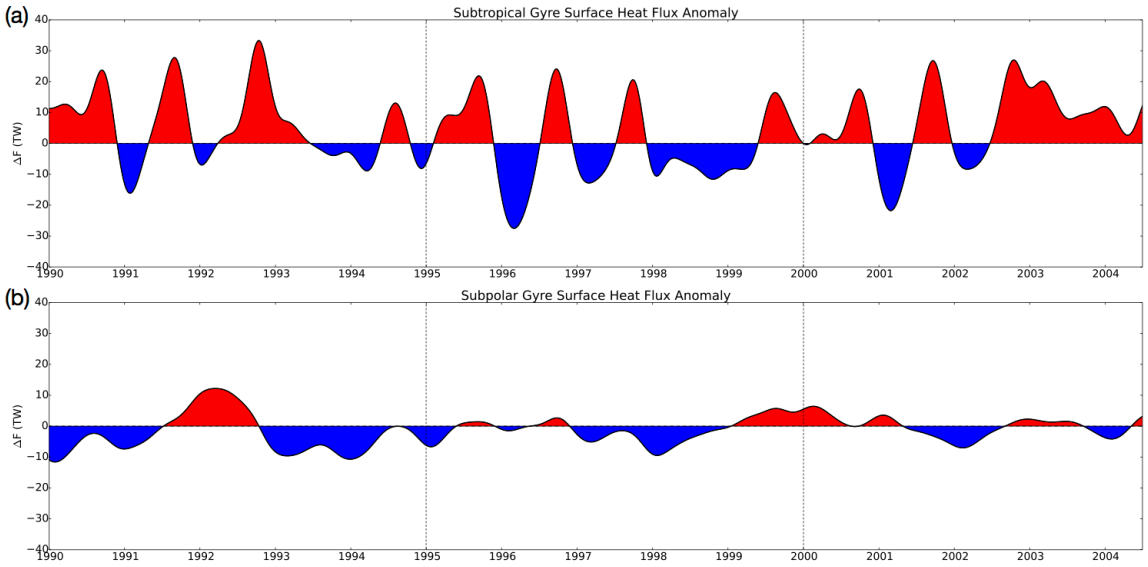


Figure 2.15. 3-month smoothed anomalous incoming heat flux across the ocean basin the subtropical gyre region (a) and subpolar gyre region (b).

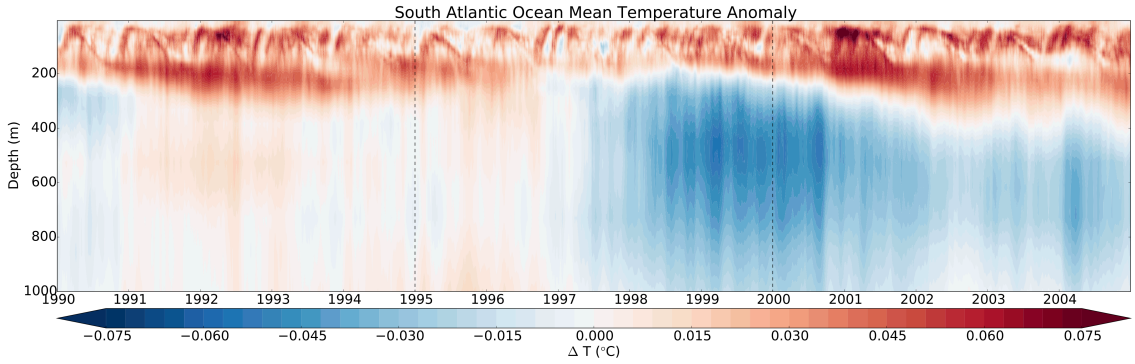


Figure 2.16. Mean South Atlantic temperature anomaly as a function of time and depth.

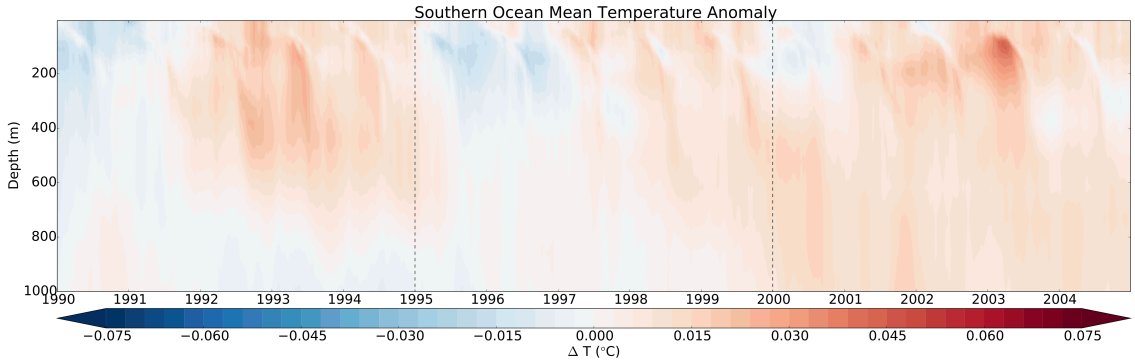


Figure 2.17. Mean Southern Ocean temperature anomaly as a function of time and depth.

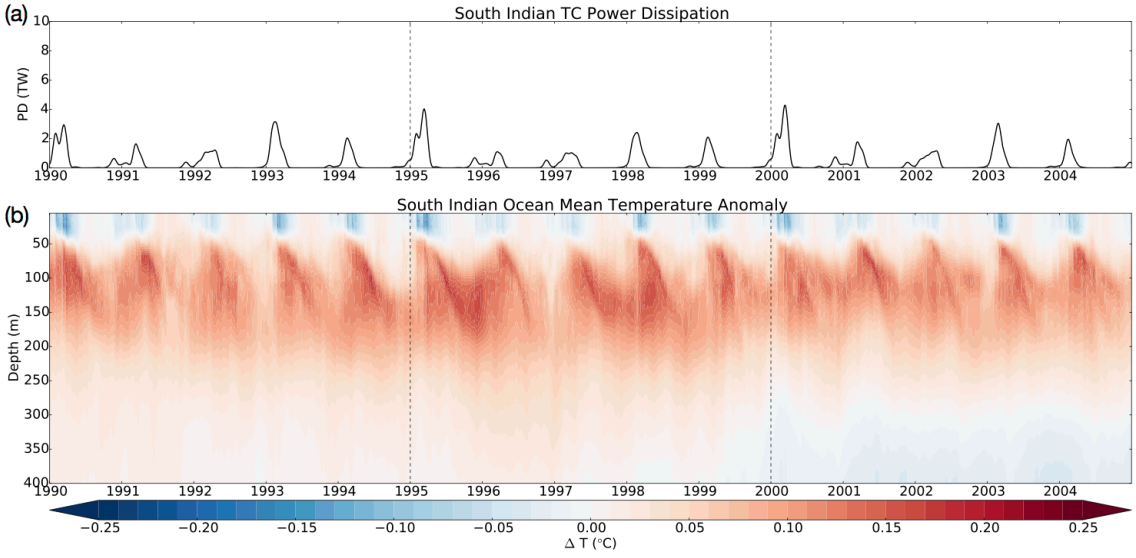


Figure 2.18. (a) TC power dissipation (91-day smoothed) integrated over the South Indian Ocean, showing the magnitude of TC forcing on the ocean. (b) Mean South Indian Ocean temperature anomaly as a function of time and depth.

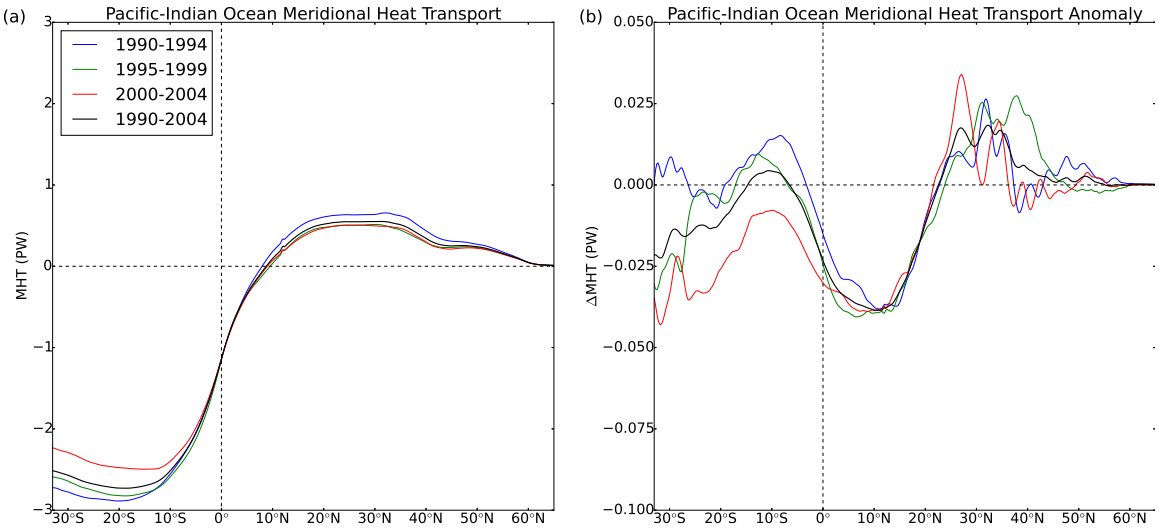


Figure 2.19. TC-induced anomaly in (a) and total (b) Pacific-Indian Ocean integrated meridional heat transport. $\Delta MHT$ and MHT are averaged from 1990-2004, and within each of the 5-year TC repeats.

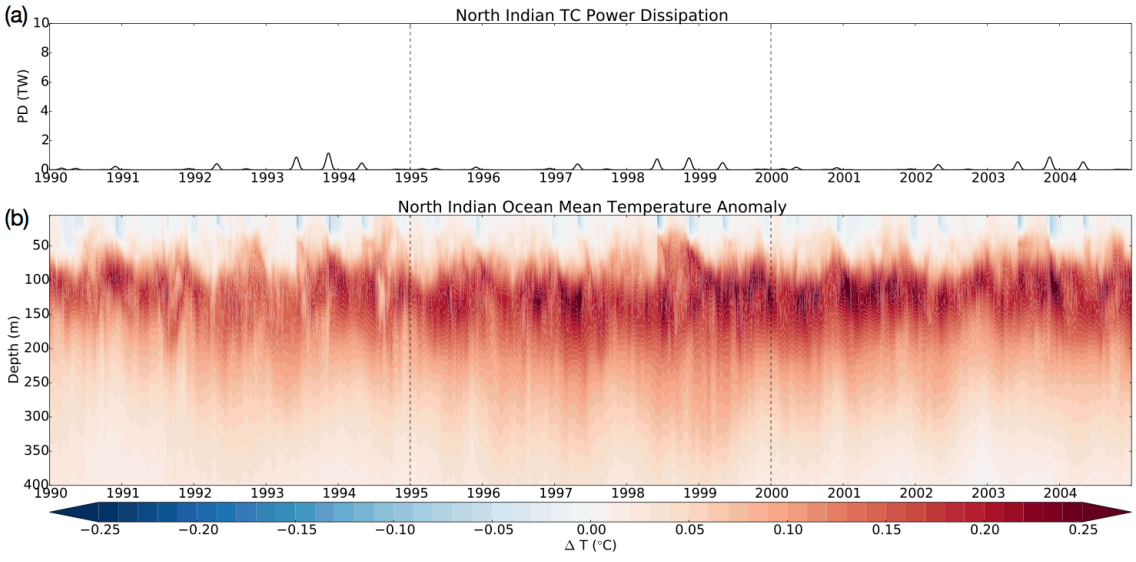


Figure 2.20. (a) TC power dissipation (91-day smoothed) integrated over the North Indian Ocean, showing the magnitude of TC forcing on the ocean. (b) Mean North Indian Ocean temperature anomaly as a function of time and depth.

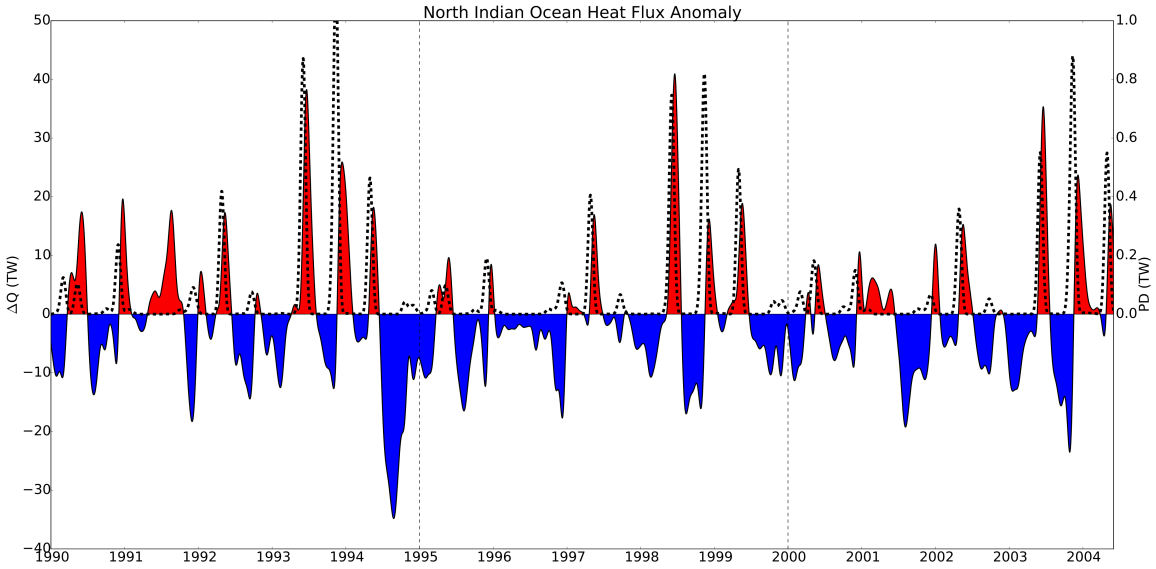


Figure 2.21. The difference between the total incoming surface heat flux between TC and control in the North Indian Ocean. Positive values indicate anomalous heat uptake, negative ventilation of TC anomalies to the atmosphere, and the dashed line is the TC power dissipation in the region.

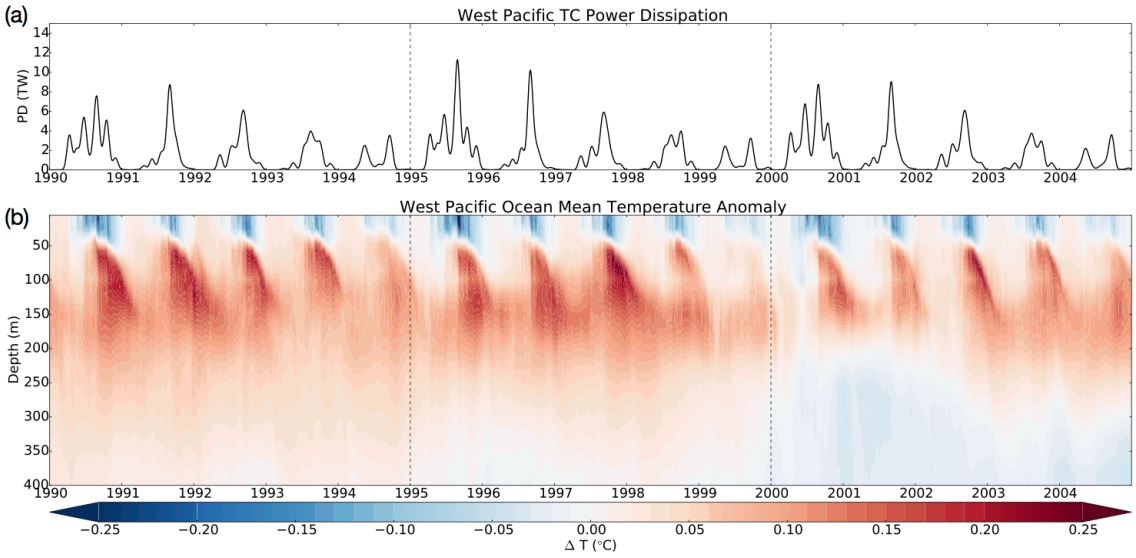


Figure 2.22. (a) TC power dissipation (91-day smoothed) integrated over the West Pacific, showing the magnitude of TC forcing on the ocean. (b) Mean West Pacific temperature anomaly as a function of time and depth.

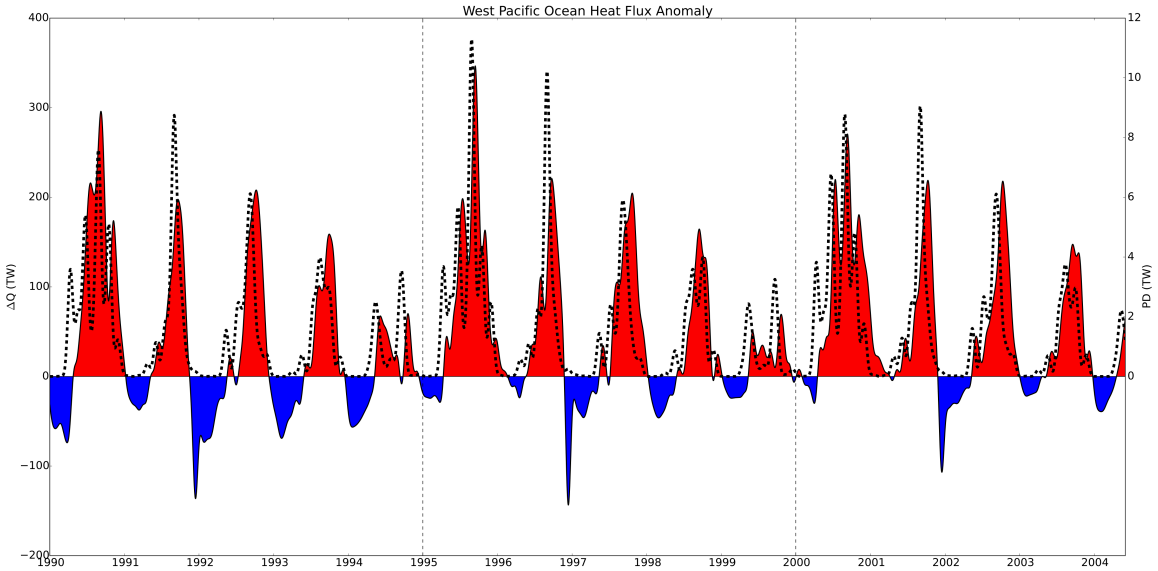


Figure 2.23. The difference between the total incoming surface heat flux between TC and control in the West Pacific. Positive values indicate anomalous heat uptake, negative ventilation of TC anomalies to the atmosphere, and the dashed line is the TC power dissipation in the region.

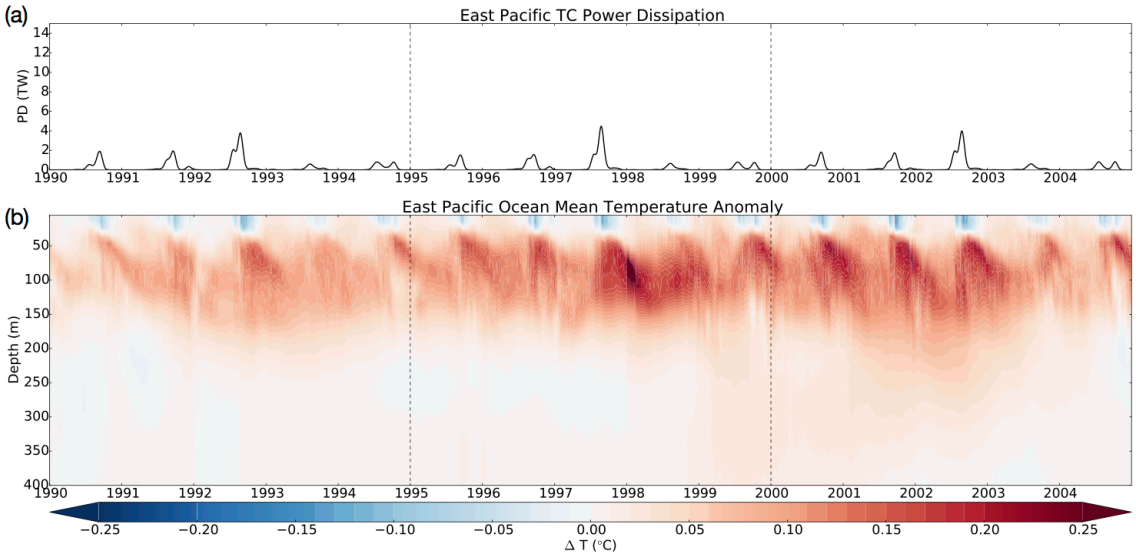


Figure 2.24. (a) TC power dissipation (91-day smoothed) integrated over the East Pacific, showing the magnitude of TC forcing on the ocean. (b) Mean East Pacific temperature anomaly as a function of time and depth.

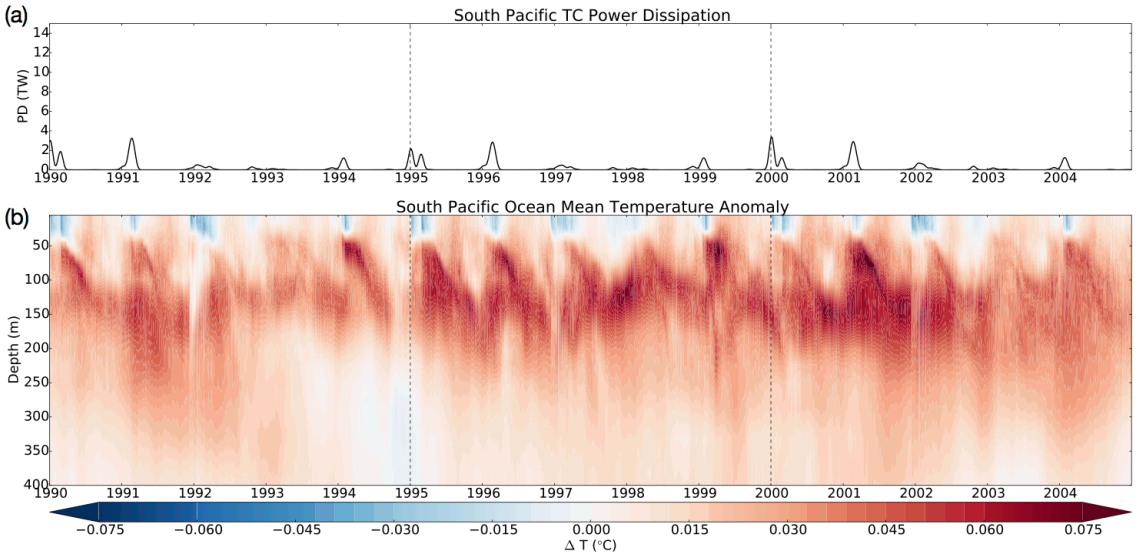


Figure 2.25. (a) TC power dissipation (91-day smoothed) integrated over the South Pacific, showing the magnitude of TC forcing on the ocean. (b) Mean South Pacific temperature anomaly as a function of time and depth.

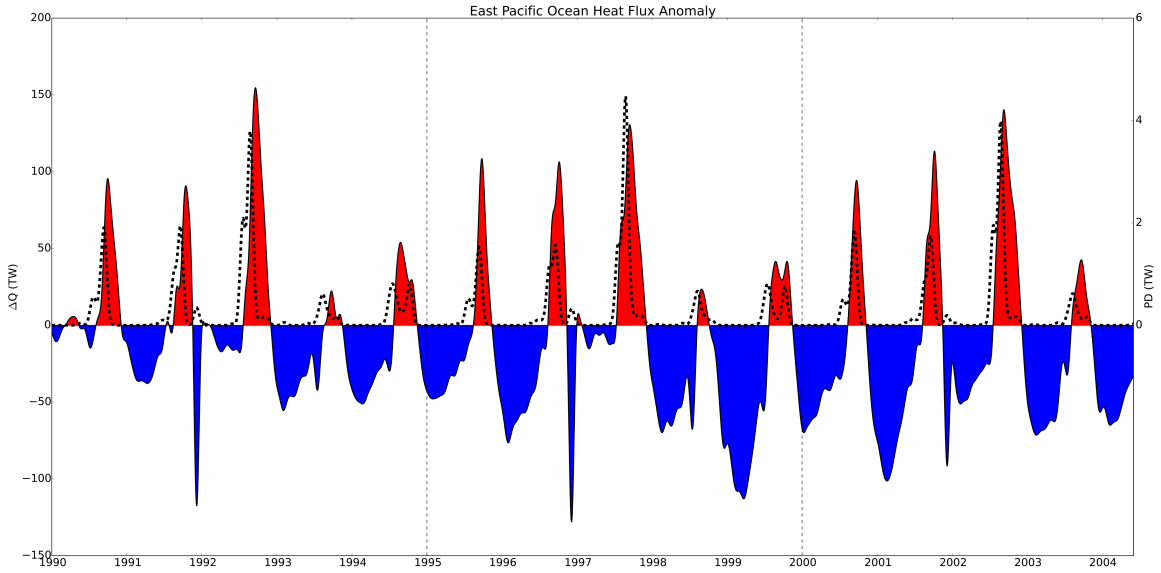


Figure 2.26. The difference between the total incoming surface heat flux between TC and control in the East Pacific. Positive values indicate anomalous heat uptake, negative ventilation of TC anomalies to the atmosphere, and the dashed line is the TC power dissipation in the region.

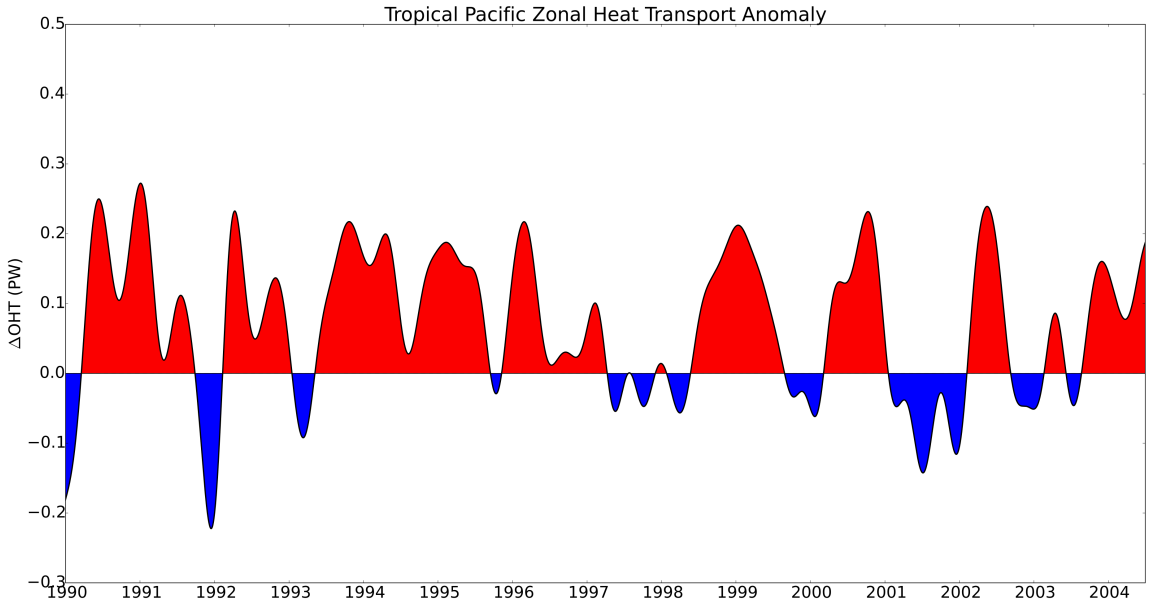


Figure 2.27. Anomalous zonal ocean heat transport from the West to East Pacific, integrated to 739 m in the tropics ($10°S$–$10°N$). Positive values indicate eastward redistribution of TC warm anomalies.

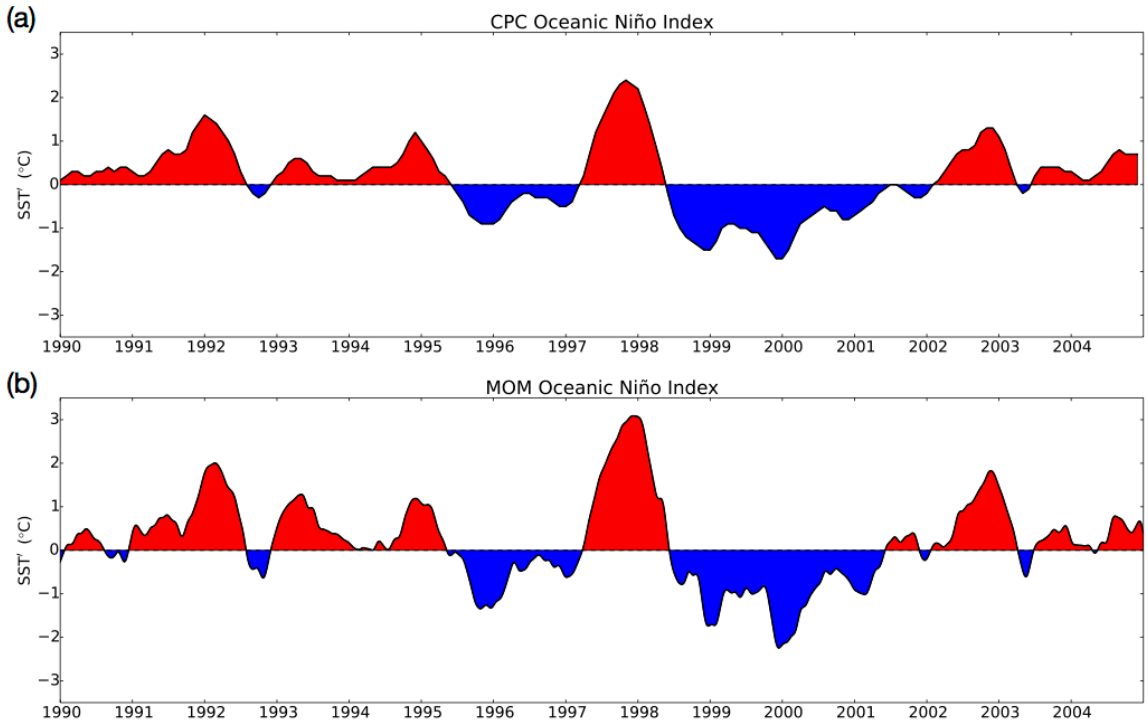


Figure 2.28. 3-month smoothed Oceanic Niño Index from the CPC time series (a) and calculated from MOM output (b). ONI is equivalent to the departure of the SST averaged over the Niño 3.4 region from its climatological mean.

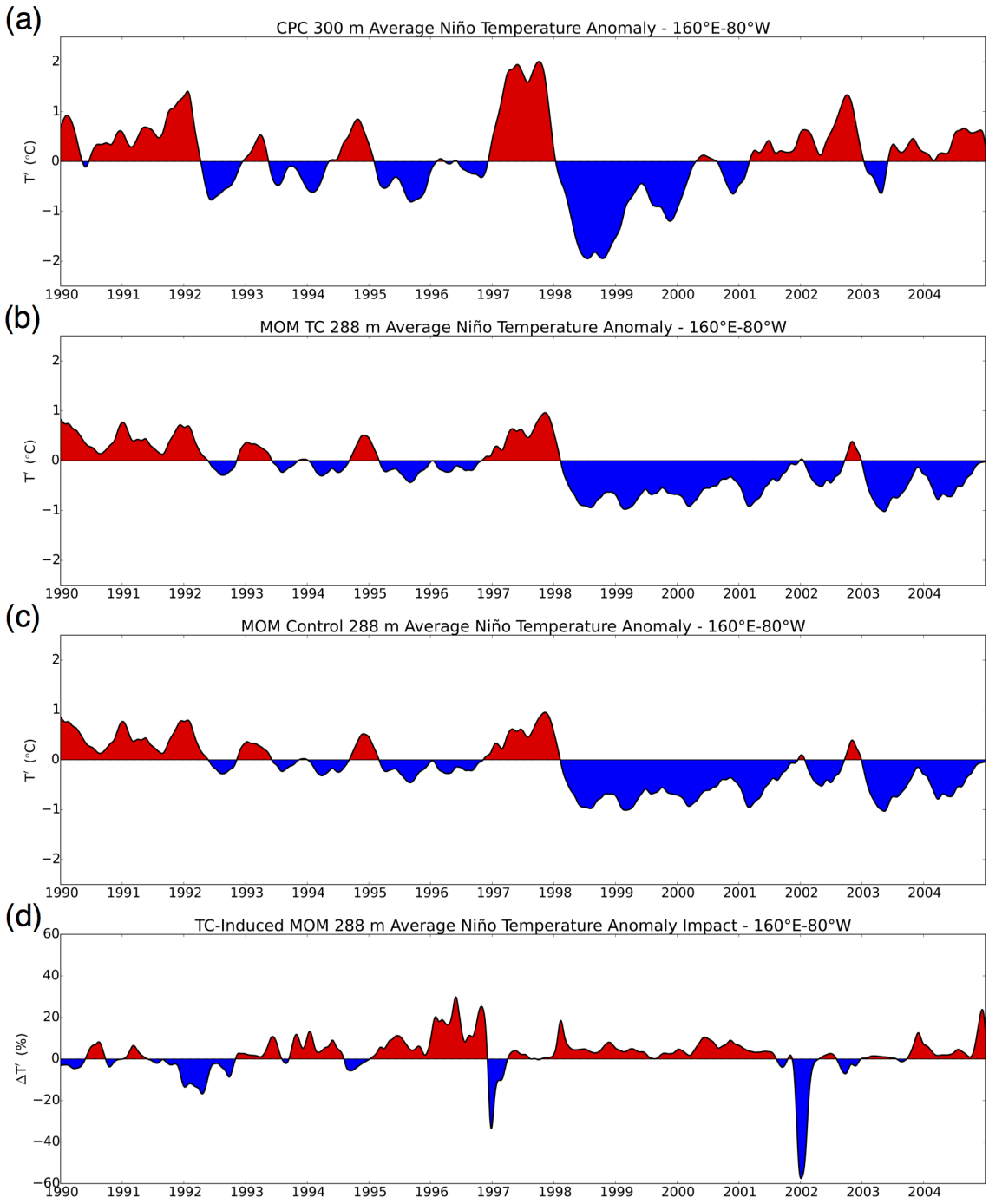


Figure 2.29. 3-month smoothed Niño heat content anomaly from (a) CPC time series, (b) the TC experiment, and (c) the control experiment. The Niño heat content anomaly defined as the departure of the temperature in the upper 300 m of the ocean, averaged between $160°E$ and $80°W$ and $10°S$ and $10°N$, from its climatological mean. The percent change in the Niño heat content anomaly (d) between TC (b) and control (c) is an indicator of the TC-impact on subsurface ENSO variability.

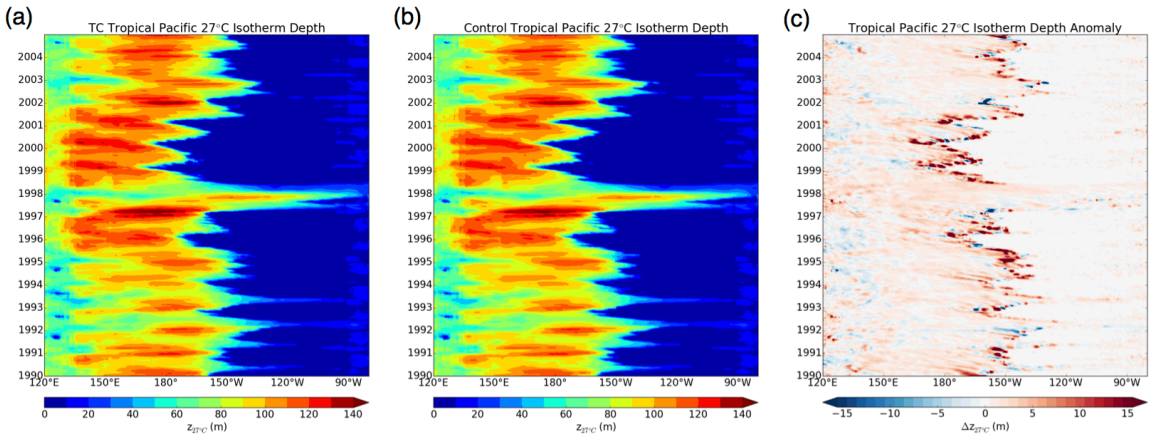


Figure 2.30. 3-month smoothed average depth of the $27°C$ isotherm in the tropics in the TC (a) and control (b) experiments. The difference between isotherm depths (c) is generally positive, indicating a mean deepening of the tropical thermocline.

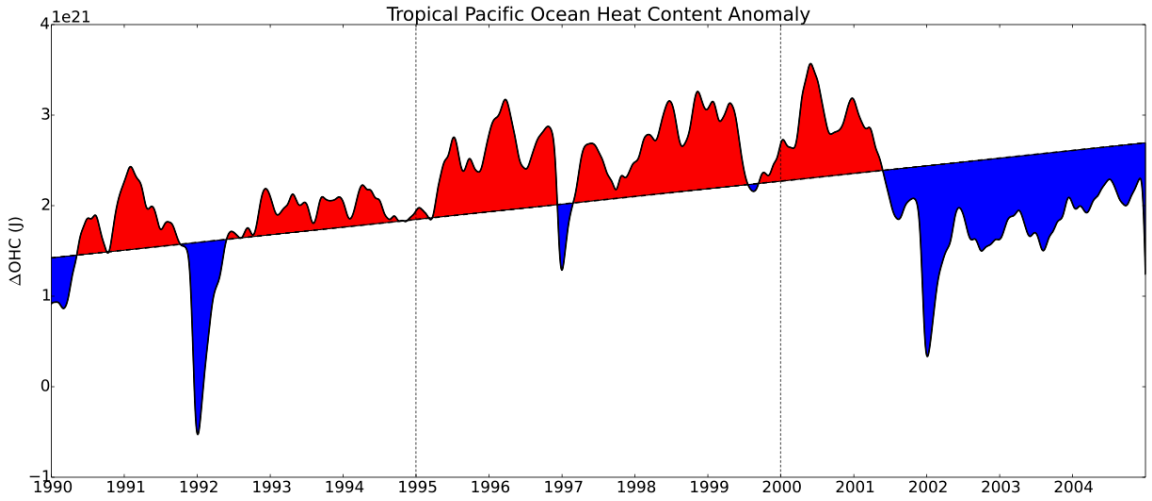


Figure 2.31. The 3-month smoothed ocean heat content anomaly in the tropical Pacific ($10°S-10°N$). The dashed line represents mean trend in $\Delta OHC_{Eq}$, with red shading indicating periods of above average increases in $\Delta OHC_{Eq}$ and blue below average.

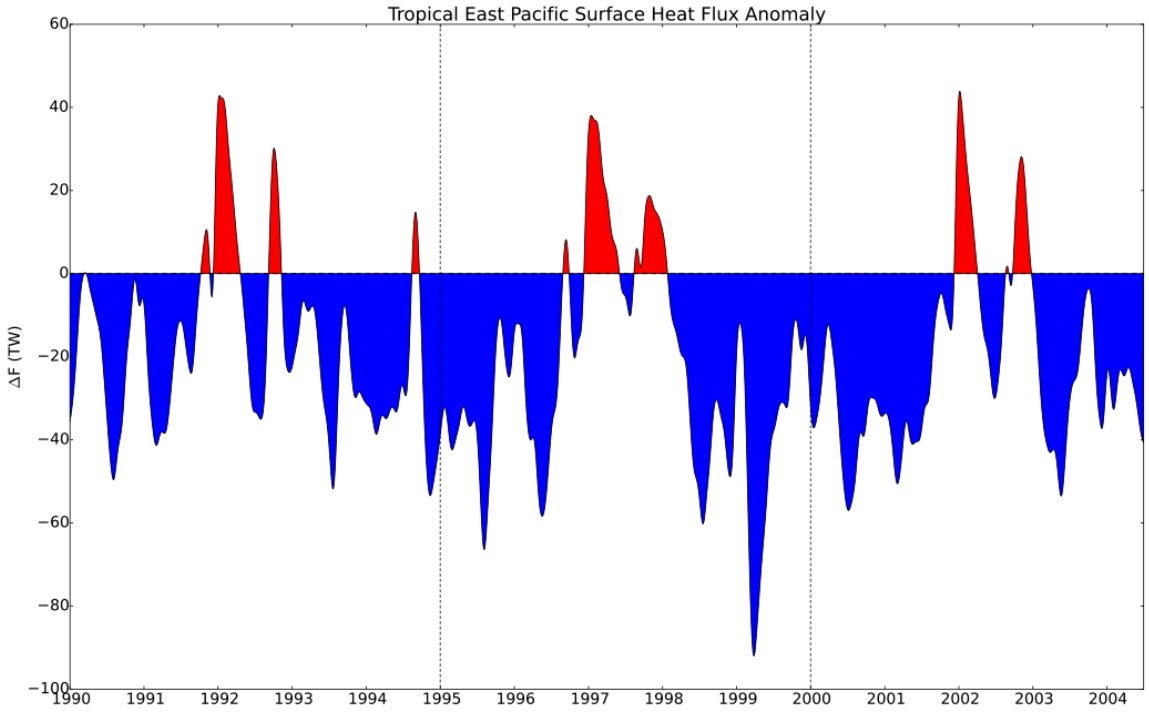


Figure 2.32. 3-month smoothed anomaly in the total incoming heat flux across the ocean surface in the tropical East Pacific. Positive values indicate anomalous heat uptake and negative ventilation of TC-induced heat anomalies to the atmosphere.

## Bibliography

Ashok, K., Behera, S. K., Rao, S. A., Weng, H., and Yamagata, T. (2007). El Niño Modoki and its Possible Teleconnection. *Journal of Geophysical Research*, 112(C11):C11007.

Barnston, A. G. and Livezey, R. E. (1987). Classification, Seasonality and Persistence of Low-Frequency Atmospheric Circulation Patterns. *Monthly Weather Review*, 115(6):1083–1126.

Bender, M. A., Ginis, I., Tuleya, R., Thomas, B., and Marchok, T. (2007). The Operational GFDL Coupled Hurricane-Ocean Prediction System and a Summary of Its Performance. *Monthly Weather Review*, 135(12):3965–3989.

Black, P. G., D'Asaro, E. A., and Sanford, T. B. (2007). AirSea Exchange in Hurricanes: Synthesis of Observations from the Coupled Boundary Layer AirSea Transfer Experiment. *Bulletin of the American Meteorological Society*, 88(8):357–374.

Boccaletti, G., Ferrari, R., and Fox-Kemper, B. (2007). Mixed Layer Instabilities and Restratification. *Journal of Physical Oceanography*, 37(9):2228–2250.

Brockmann, C., Fahrbach, E., Huyer, A., and Smith, R. L. (1980). The Poleward Undercurrent Along the Peru Coast: 5 to 15°S. *Deep-Sea Research*, 27(10):847–856.

Bueti, M. R., Ginis, I., Rothstein, L. M., and Griffies, S. M. (2014). Tropical Cyclone-Induced Thermocline Warming and its Regional and Global Impacts. *Journal of Climate*, 27(18):6978–6999.

Cummings, J. A. (2005). Operational Multivariate Ocean Data Assimilation. *Quarterly Journal of the Royal Meteorological Society*, 131(613):3583–3604.

Danabasoglu, G., Yeager, S. G., Bailey, D., Behrens, E., Bentsen, M., Bi, D., Biastoch, A., Böning, C. W., Bozec, A., Canuto, V. M., Cassou, C., Chassignet, E., Coward, A. C., Danilov, S., Diansky, N., Drange, H., Farneti, R., Fernandez, E., Fogli, P. G., Forget, G., Fujii, Y., Griffies, S. M., Gusev, A., Heimbach, P., Howard, A., Jung, T., Kelley, M., Large, W. G., Leboissetier, A., Lu, J., Madec, G., Marsland, S. J., Masina, S., Navarra, A., Nurser, A. G., Pirani, A., y Mélia, D. S., Samuels, B. L., Scheinert, M., Sidorenko, D., Treguier, A.-M., Tsujino, H., Uotila, P., Valcke, S., Voldoire, A., and Wang, Q. (2014). North Atlantic Simulations in Coordinated Ocean-Ice Reference Experiments Phase II (CORE-II). Part I: Mean States. *Ocean Modelling*, 73(0):76–107.

Dare, R. A. and McBride, J. L. (2011). Sea Surface Temperature Response to Tropical Cyclones. *Monthly Weather Review*, 139(12):3798–3808.

D'Asaro, E. A., Sanford, T. B., Niiler, P. P., and Terrill, E. J. (2007). Cold Wake of Hurricane Frances. *Geophysical Research Letters*, 34(15):L15609.

Delworth, T. L., Rosati, A., Anderson, W., Adcroft, A. J., Balaji, V., Benson, R., Dixon, K., Griffies, S. M., Lee, H.-C., Pacanowski, R. C., Vecchi, G. A., Wittenberg, A. T., Zeng, F., and Zhang, R. (2012). Simulated Climate and Climate Change in the GFDL CM2.5 High-Resolution Coupled Climate Model. *Journal of Climate*, 25(8):2755–2781.

Emanuel, K. A. (1999). The Power of a Hurricane: An Example of Reckless Driving on the Information Superhighway. *Weather*, 54(4).

Emanuel, K. A. (2001). Contribution of Tropical Cyclones to Meridional Heat Transport by the Oceans. *Journal of Geophysical Research*, 106(D14):14771–14781.

Fedorov, A. V., Brierley, C. M., and Emanuel, K. A. (2010). Tropical Cyclones and Permanent El Niño in the Early Pliocene Epoch. *Nature*, 463(7284):1066–1070.

Fox-Kemper, B., Danabasoglu, G., Ferrari, R., Griffies, S. M., Hallberg, R. W., Holland, M. M., Maltrud, M. E., Peacock, S., and Samuels, B. L. (2011). Parameterization of Mixed Layer Eddies. III: Implementation and Impact in Global Ocean Climate Simulations. *Ocean Modelling*, 39(1-2):61–78.

Gent, P. R., Danabasoglu, G., Donner, L. J., Holland, M. M., Hunke, E. C., Jayne, S. R., Lawrence, D. M., Neale, R. B., Rasch, P. J., Vertenstein, M., Worley, P. H., Yang, Z.-L., and Zhang, M. (2011). The Community Climate System Model Version 4. *Journal of Climate*, 24(19):4973–4991.

Ginis, I. (2002). Tropical Cyclone-Ocean Interactions. *Advances in Fluid Mechanics Series*, 33:83–114.

Gordon, A. L., Susanto, R. D., and Ffield, A. (1999). Throughflow within Makassar Strait. *Geophysical Research Letters*, 26(21):3325–3328.

Griffies, S. M. (2009). Elements of MOM4p1. *GFDL Ocean Group Technical Report*, 6:444.

Griffies, S. M., Biastoch, A., Böning, C., Bryan, F., Danabasoglu, G., Chassignet, E. P., England, M. H., Gerdes, R., Haak, H., Hallberg, R. W., Hazeleger, W., Jungclaus, J., Large, W. G., Madec, G., Pirani, A., Samuels, B. L., Scheinert, M., Sen Gupta, A., Severijns, C. A., Simmons, H. L., Treguier, A. M., Winton, M., Yeager, S., and Yin, J. (2009). Coordinated Ocean-Ice Reference Experiments (COREs). *Ocean Modelling*, 26(1-2):1–46.

Holland, G. J. (1980). An Analytic Model of the Wind and Pressure Profiles in Hurricanes. *Monthly Weather Review*, 108(8):1212–1218.

Izumo, T. (2005). The Equatorial Undercurrent, Meridional Overturning Circulation, and their Roles in Mass and Heat Exchanges during El Niño Events in the Tropical Pacific Ocean. *Ocean Dynamics*, 55(2):110–123.

Jansen, M. and Ferrari, R. (2009). Impact of the Latitudinal Distribution of Tropical Cyclones on Ocean Heat Transport. *Geophysical Research Letters*, 36(6):L06604.

Jansen, M. F., Ferrari, R., and Mooring, T. A. (2010). Seasonal Versus Permanent Thermocline Warming by Tropical Cyclones. *Geophysical Research Letters*, 37(3):L03602.

Jayne, S. R. and Marotzke, J. (2001). The Dynamics of Ocean Heat Transport Variability. *Review of Geophysics*, 39(3):385–411.

Jullien, S., Menkes, C. E., Marchesiello, P., Jourdain, N. C., Lengaigne, M., Koch-Larrouy, A., Lefèvre, J., Vincent, E. M., and Faure, V. (2012). Impact of Tropical Cyclones on the Heat Budget of the South Pacific Ocean. *Journal of Physical Oceanography*, 42(11):1882–1906.

Large, W. G., McWilliams, J. C., and Doney, S. C. (1994). Oceanic Vertical Mixing: A Review and a Model with a Nonlocal Boundary Layer Parameterization. *Reviews of Geophysics*, 32(4):363–403.

Large, W. G. and Yeager, S. G. (2004). Diurnal to Decadal Global Forcing for Ocean and Sea-Ice Models: The Data Sets and Flux Climatologies. *NCAR Technical Note*.

Large, W. G. and Yeager, S. G. (2009). The Global Climatology of an Interannually Varying Air-Sea Flux Data Set. *Climate Dynamics*, 33(2-3):341–364.

Levitus, S., Antonov, J. I., Boyer, T. P., Baranova, O. K., Garcia, H. E., Locarnini, R. A., Mishonov, A. V., Reagan, J. R., Seidov, D., Yarosh, E. S., and Zweng,

M. M. (2012a). World Ocean Heat Content and Thermosteric Sea Level Change (0-2000 m), 1955-2010. *Geophysical Research Letters*, 39(10):n/a–n/a.

Levitus, S., Antonov, J. I., Boyer, T. P., Baranova, O. K., Garcia, H. E., Locarnini, R. A., Mishonov, A. V., Reagan, J. R., Seidov, D., Yarosh, E. S., and Zweng, M. M. (2012b). World Ocean Heat Content and Thermosteric Sea Level Change (0-2000 m), 1955-2010. *Geophysical Research Letters*, 39(10):L10603.

Lukas, R. (1988). Interannual Fluctuations of the Mindanao Current Inferred from Sea Level. *Journal of Geophysical Research*, 93(C6):6744–6748.

Manucharyan, G. E., Brierley, C. M., and Fedorov, A. V. (2011). Climate Impacts of Intermittent Upper Ocean Mixing Induced by Tropical Cyclones. *Journal of Geophysical Research*, 116(C11):C11038.

McCreary, J. P. and Lu, P. (1994). Interaction Between the Subtropical and Equatorial Ocean Circulations: The Subtropical Cell. *Journal of Physical Oceanography*, 24:466–497.

Mei, W. and Pasquero, C. (2013). Spatial and Temporal Characterization of Sea Surface Temperature Response to Tropical Cyclones*. *Journal of Climate*, 26(11):3745–3765.

Mei, W., Primeau, F., McWilliams, J. C., and Pasquero, C. (2013). Sea Surface Height Evidence for Long-Term Warming Effects of Tropical Cyclones on the Ocean. *Proceedings of the National Academy of Sciences.*, 110(38):15207–15210.

Moon, I.-J., Ginis, I., Hara, T., and Thomas, B. (2007). A Physics-Based Parameterization of Air-Sea Momentum Flux at High Wind Speeds and Its Impact on Hurricane Intensity Predictions. *Monthly Weather Review*, 135(8):2869–2878.

Park, J. J., Kwon, Y.-O., and Price, J. F. (2011). Argo Array Observation of Ocean Heat Content Changes Induced by Tropical Cyclones in the North Pacific. *Journal of Geophysical Research*, 116(C12):C12025.

Pasquero, C. and Emanuel, K. A. (2008). Tropical Cyclones and Transient Upper-Ocean Warming. *Journal of Climate*, 21(1):149–162.

Powell, M. D., Vickery, P. J., and Reinhold, T. A. (2003). Reduced Drag Coefficient for High Wind Speeds in Tropical Cyclones. *Nature*, 422(6929):279–283.

Price, J. F. (1981). Upper Ocean Response to a Hurricane. *Journal of Physical Oceanography*, 11(2):153–175.

Price, J. F., Morzel, J., and Niiler, P. P. (2008). Warming of SST in the Cool Wake of a Moving Hurricane. *Journal of Geophysical Research*, 113(C7):C07010.

Qu, T. and Lukas, R. (2003). The Bifurcation of the North Equatorial Current in the Pacific*. *Journal of Physical Oceanography*, 33(1):5–18.

Reynolds, R. W., Smith, T. M., Liu, C., Chelton, D. B., Casey, K. S., and Schlax, M. G. (2007). Daily High-Resolution-Blended Analyses for Sea Surface Temperature. *Journal of Climate*, 20(22):5473–5496.

Rothstein, L. M., Zhang, R.-H., Busalacchi, A. J., and Chen, D. (1998). A Numerical Simulation of the Mean Water Pathways in the Subtropical and Tropical Pacific Ocean. *Journal of Physical Oceanography*, 28(2):322–343.

Ruijter, W., Biastoch, A., Drijfhout, S. S., Lutjeharms, J. R. E., Matano, R. P., Pichevin, T., van Leeuwen, P. J., and Weijer, W. (1999). Indian-Atlantic Interocean Exchange: Dynamics, Estimation and Impact. *Journal of Geophysical Research*, 104(C9):20855–20910.

Sanford, T. B., Price, J. F., Girton, J. B., and Webb, D. C. (2007). Highly Resolved Observations and Simulations of the Ocean Response to a Hurricane. *Geophysical Research Letters*, 34(13):L13604.

Schott, F. A. and McCreary, J. P. (2001). The Monsoon Circulation of the Indian Ocean. *Progress in Oceanography*, 51(1):1–123.

Schouten, M. W. (2002). Upstream Control of Agulhas Ring Shedding. *Journal of Geophysical Research*, 107(C8):3109–23–11.

Scoccimarro, E., Gualdi, S., Bellucci, A., Sanna, A., Giuseppe Fogli, P., Manzini, E., Vichi, M., Oddo, P., and Navarra, A. (2011). Effects of Tropical Cyclones on Ocean Heat Transport in a High-Resolution Coupled General Circulation Model. *Journal of Climate*, 24(16):4368–4384.

Shukla, J. (1975). Effect of Arabian Sea-Surface Temperature Anomaly on Indian Summer Monsoon-Numerical Experiment with GFDL Model. *Journal of the Atmospheric Sciences*, 32(3):503–511.

Sriver, R. L. and Huber, M. (2007). Observational Evidence for an Ocean Heat Pump Induced by Tropical Cyclones. *Nature*, 447(7144):577–580.

Sriver, R. L. and Huber, M. (2010). Modeled Sensitivity of Upper Thermocline Properties to Tropical Cyclone Winds and Possible Feedbacks on the Hadley circulation. *Geophysical Research Letters*, 37(8):L08704.

Sriver, R. L., Huber, M., and Chafik, L. (2013). Excitation of Equatorial Kelvin and Yanai Waves by Tropical Cyclones in an Ocean General Circulation Model. *Earth System Dynamics*, 4(1):1–10.

Sriver, R. L., Huber, M., and Nusbaumer, J. (2008). Investigating Tropical

Cyclone-Climate Feedbacks Using the TRMM Microwave Imager and the Quick Scatterometer. *Geochemistry, Geophysics, Geosystems*, 9(9):Q09V11.

Stommel, H. (1979). Determination of Water mass Properties of Water Pumped Down from the Ekman Layer to the Geostrophic Flow Below. *Proceedings of the National Academy of Sciences.*, 76(7):3051–3055.

Trahan, S. and Sparling, L. (2012). An Analysis of NCEP Tropical Cyclone Vitals and Potential Effects on Forecasting Models. *Weather Forecasting*, 27(3):744–756.

Trenberth, K. E. (1997). The Definition of El Niño. *Bulletin of the American Meteorological Society*, 78(12):2771–2777.

Trenberth, K. E. and Caron, J. M. (2001). Estimates of Meridional Atmosphere and Ocean Heat Transports. *Journal of Climate*, 14(16):3433–3443.

Vincent, E. M., Lengaigne, M., Madec, G., Vialard, J., Samson, G., Jourdain, N. C., Menkes, C. E., and Jullien, S. (2012a). Processes Setting the Characteristics of Sea Surface Cooling Induced by Tropical Cyclones. *Journal of Geophysical Research*, 117(C2):C02020.

Vincent, E. M., Lengaigne, M., Vialard, J., Madec, G., Jourdain, N. C., and Masson, S. (2012b). Assessing the Oceanic Control on the Amplitude of Sea Surface Cooling Induced by Tropical Cyclones. *Journal of Geophysical Research*, 117(C5):C05023.

Vincent, E. M., Madec, G., Lengaigne, M., Vialard, J., and Koch-Larrouy, A. (2013). Influence of Tropical Cyclones on Sea Surface Temperature Seasonal Cycle and Ocean Heat Transport. *Climate Dynamics*, 41(7-8):2019–2038.

Wang, C. Z. (2001). A Unified Oscillator Model for the El Niño-Southern Oscillation. *Journal of Climate*, 14(1):98–115.

Willoughby, H. E., Darling, R. W. R., and Rahn, M. E. (2006). Parametric Representation of the Primary Hurricane Vortex. Part II: A New Family of Sectionally Continuous Profiles. *Monthly Weather Review*, 134(4):1102–1120.

Wunsch, C. (2005). The Total Meridional Heat Flux and its Oceanic and Atmospheric Partition. *Journal of Climate*, 18(21):4374–4380.

Wyrtki, K. (1981). An Estimate of Equatorial Upwelling in the Pacific. *Journal of Physical Oceanography*, 11(9):1205–1214.

Yablonsky, R. M. and Ginis, I. (2009). Limitation of One-Dimensional Ocean Models for Coupled Hurricane-Ocean Model Forecasts. *Monthly Weather Review*, 137(12):4410–4419.

Yang, J., Liu, Q., Xie, S. P., and Liu, Z. (2007). Impact of the Indian Ocean SST basin mode on the Asian summer monsoon. *Geophysical Research Letters*, 34:L02708.

Yeager, S., Karspeck, A., Danabasoglu, G., Tribbia, J., and Teng, H. (2012). A Decadal Prediction Case Study: Late Twentieth-Century North Atlantic Ocean Heat Content. *Journal of Climate*, 25(15):5173–5189.

Zhang, S., Harrison, M. J., Rosati, A., and Wittenberg, A. (2007). System Design and Evaluation of Coupled Ensemble Data Assimilation for Global Oceanic Climate Studies. *Monthly Weather Review*, 135(10):3541–3564.

# APPENDIX

## Wind Formulation

TC winds are based on the NHC/JTWC TCVitals database, as seen in Tables 1.1 and 1.2 and described by Trahan and Sparling (2012). This database provides representation of the storms location, intensity, and structure produced every six hours as a real-time analysis of all available data. The specific parameters utilized are the longitude and latitude of the center of storm circulation, the maximum sustained wind speed (MWS), radius of maximum wind (RMW), central sea level pressure ($p_c$), environmental sea level pressure ($p_o$), radius of outermost closed isobar ($R_{cls}$), and the radii at which the sustained winds reach values of 18 $m\ s^{-1}$ and 26 $m\ s^{-1}$ in the northeast, southeast, southwest, and northwest quadrants of the storm ($R_{18}$ and $R_{26}$). Each of these parameters is linearly interpolated in time, along the storm track, to the current model time step, in order to provide a coherent storm structure at all times.

Based on the presence of the $R_{18}$ and $R_{26}$ parameters, an asymmetric empirical wind field is calculated that accounts for the differing wind radii in each quadrant of the storm (Bender et al. (2007)). For each location in space, the radial distance from the storm center, $r$, and angular departure from due north, $\alpha$, are determined. $R_{18}$ and $R_{26}$ are interpolated along lines of constant $r$ to the current $\alpha$. Based on which of these radii are present for the current time (having a value greater than zero in the best track database), a scaling radius and wind speed are derived for the current

angle $\alpha$

$$R_1(\alpha) = \begin{cases} \frac{1}{2}\left(R_{18}(\alpha) + R_{26}(\alpha)\right) & \text{if } R_{18} > 0 \ \& \ R_{26} > 0 \\ R_{18}(\alpha) & \text{if } R_{26} < 0 \\ R_{26}(\alpha) & \text{if } R_{18} < 0 \end{cases} \tag{A.1a}$$

$$V_1(\alpha) = \begin{cases} 22\ m/s & \text{if } R_{18} > 0 \ \& \ R_{26} > 0 \\ 18\ m/s & \text{if } R_{26} < 0 \\ 26\ m/s & \text{if } R_{18} < 0 \end{cases} \tag{A.1b}$$

which are used to calculate an angularly dependent e-folding radius, $b$, for the wind speed

$$b(\alpha) = \frac{\text{RMW} - R_1(\alpha)}{\ln\left(\frac{V_1(\alpha)}{\text{MWS}}\right)} \tag{A.2}$$

and finally arrive at a wind speed profile that is linear within the RMW, and decays exponentially without

$$U_{10}(r,\alpha) = \text{MWS} \cdot \begin{cases} \frac{r}{\text{RMW}} & \text{if } r < \text{RMW} \\ e^{(\text{RMW}-r)/b(\alpha)} & \text{if } r \geq \text{RWM} \end{cases} \tag{A.3}$$

This wind speed magnitude is decomposed into tangential ($U_{tan}$) and radial ($U_{rad}$) components as

$$U_{tan}(r,\alpha) = U_{10}(r,\alpha) \cdot \cos\left(\theta(r)\right) \tag{A.4a}$$

$$U_{rad}(r,\alpha) = -U_{10}(r,\alpha) \cdot \sin\left(\theta(r)\right) \tag{A.4b}$$

where $\theta(r)$ is an empirically derived angle represent the proportion of the wind directed in the radial direction (inflow) versus tangentially. These radial and tangential winds are then converted into zonal and meridional components as

$$u(r,\alpha) = U_{rad} \cdot \cos(\alpha) - U_{tan} \cdot \sin(\alpha) = -U_{10} \cdot \sin(\alpha + \theta(r)) \tag{A.5a}$$

$$v(r,\alpha) = U_{tan} \cdot \cos(\alpha) - U_{rad} \cdot \sin(\alpha) = U_{10} \cdot \cos(\alpha + \theta(r)) \tag{A.5b}$$

In the absence of the angularly dependent structure data, the axisymmetric wind profile of Holland (1980)) is used instead. RMW, MWS, and pressure gradient $\Delta p = (p_c - p_o)$ are used to calculate the scaling variables

$$A = \mathrm{RMW}^B \tag{A.6a}$$

$$B = \mathrm{MWS}^2 \cdot e \cdot \frac{\rho_a}{\Delta p} \tag{A.6b}$$

where $\rho_a$ is the density of dry air ($\sim$1.28 $kg\ m^{-3}$). These two parameters are then used to calculate a wind speed magnitude at each grid point

$$U_{10}(r) = \left[ A \cdot B \left( \frac{e^{-A/r^B}}{\rho_a \cdot r^B} \right) + \frac{r^2 \cdot f^2}{4} \right]^{1/2} - \frac{r \cdot f}{2} \tag{A.7}$$

where $r$ is the current distance from the center of circulation. As above, the wind speed magnitude is then decomposed into zonal and meridional components. These wind speed vectors are then augmented by one-half of the storm's translation speed, in order to capture some portion of the asymmetry caused by the superposition of the storms circulation and forward motion.

Synthetic wind speeds are generated for each storm in the best track database in sequence, on a 1/6° resolution equirectangular grid, using the appropriate formulation. In order to minimize the overlap of storm profiles and problems in the tail of the Holland (1980) wind profile as the Coriolis parameter $f$ tends to zero, the winds are constrained to uniformly vanish outside of an imposed radius equal to twice the $R_{cls}$. This radius is chosen because, physically, $R_{cls}$ should roughly represent the size of the closed, recirculation vortex, but somewhat underestimates the distance at which the synthetic TC winds are uniformly smaller than the CORE-II winds.

Each storm is projected onto the ocean model grid. A point-by-point comparison is then made between the synthetic TC and specified CORE-II wind speed magnitudes. For those points where the TC forcing is greater, the meridional and zonal wind speed components from the CORE forcing are replaced by those from the synthetic

storm. In this way, relatively smooth embedding of the empirically generated storms into an atmospheric dataset that previously lacked strong TC forcing is achieved.